Neural Network Approach for Predicting the Failure of Turbine Components

Nafisa Bano

Thesis submitted to the
Faculty of Graduate and Postdoctoral Studies
in partial fulfillment of the requirements
for a doctoral degree in Mechanical Engineering

Department of Mechanical Engineering
Faculty of Engineering
University of Ottawa

Abstract: Turbine components operate under severe loading conditions and at high and varying temperatures that result in thermal stresses in the presence of temperature gradients created by hot gases and cooling air. Moreover, static and cyclic loads as well as the motion of rotating components create mechanical stresses. The combined effect of complex thermo-mechanical stresses promote nucleation and propagation of cracks that give rise to fatigue and creep failure of the turbine components. Therefore, the relationship between thermo-mechanical stresses, chemical composition, heat treatment, resulting microstructure, operating temperature, material damage, and potential failure modes, i.e. fatigue and/or creep, needs to be well understood and studied. Artificial neural networks are promising candidate tools for such studies. They are fast, flexible, efficient, and accurate tools to model highly non-linear multi-dimensional relationships and reduce the need for experimental work and time-consuming regression analysis. Therefore, separate neural network models for γ' precipitate strengthened Ni based superalloys have been developed for predicting the γ' precipitate size, thermal expansion coefficient, fatigue life, and hysteresis energy. The accumulated fatigue damage is then estimated as the product of hysteresis energy and fatigue life. The models for γ' precipitate size, thermal expansion coefficient, and hysteresis energy converge very well and match experimental data accurately. The fatigue life proved to be the most challenging aspect to predict, and fracture mechanics proved to potentially be a necessary supplement to neural networks. The model for fatigue life converges well, but relatively large errors are observed partly due to the generally large statistical variations inherent to fatigue life. The deformation mechanism map for 1.23Cr-1.2Mo-0.26V rotor steel has been constructed using dislocation glide, grain boundary sliding, and power law creep rate equations. The constructed map is verified with experimental data points and neural network results. Although the existing set of experimental data points for neural network modeling is limited, there is an excellent match with boundaries constructed using rate equations which validates the deformation mechanism map.

DEDICATION

To my mother Fatima Begum, my son Aman, my twin daughters Khushi and Khushboo.

Acknowledgements

First of all, I want to express my sincere gratitude to the Almighty for giving me the strength, knowledge, and patience to complete this task, which I believe is the most significant accomplishment in my life.

I would like to thank my thesis supervisor Prof. Michel Nganbe whose exceptional knowledge in the field of materials science, excellent guidance, and encouragement helped me successfully complete this research. He showed utmost patience in reading and correcting research papers and thesis drafts. I would also like to thank late Dr. Atef Fahim for his guidance and support. I want to give my special thanks to Dr. A. K. Koul for his guidance, encouragement, suggestion, and discussion.

I acknowledge the financial support from the Department of Mechanical Engineering and the Faculty of Graduate and Postdoctoral Studies provided in the form of Admission Scholarship, Teaching, and Research Assistantships.

In addition, I would like to acknowledge my parents, my kids Aman, Khushi, and Khushboo, my father in-law and mother in-law, other family members, and friends for their continued support and encouragements.

Finally, I would like to thank my husband (Nazish Irfan) for his encouragement and moral support throughout my research work. Without his loving support and understanding, I would have never completed this work.

TABLE OF CONTENTS

LIST OF FIGURES

LIST OF TABLES

NOMENCLATURE

A	Material constant in Paris equation
A_{PLC}	Non-dimensional constant in power law creep equation
A_{GBS}	Non-dimensional constant in grain boundary sliding equation
b	Bias of a simple neuron
b	Burgers vector
b	y-intercept of linear regression analysis
c	Crack length
c_o	Initial crack size
c_f	Final or critical crack size
d	Grain size
dc/dN	Crack growth rate
D_F	Accumulated fatigue energy or damage
D_{FA}	Fatigue damage obtained from hysteresis area loop equation
D_{FNN}	Fatigue damage obtained from neural network
D_{gb}	Diffusion coefficient for grain boundary diffusion
D_{ogb}	Pre-exponential constant for grain boundary diffusion
D_{ov}	Pre-exponential constant for volume diffusion
D_v	Volume diffusivity
e	Vector of network errors
g_k	Current gradient of backpropagation training
G	Glossop Superalloys Ltd.
I	Identity matrix
J	Jacobian matrix
J^T	Transpose of the Jacobian matrix
k	Boltzmann constant
K	Stress intensity factor
K_{min}	Minimum stress intensity factor
K_{max}	Maximum stress intensity factor

K_{IC}	Fracture toughness
m	Material constant in Paris equation
m	Slope of linear regression analysis
mse	Mean square error
msereg	Mean square error for Bayesian Regularization
msw	Mean square weight
mu (μ)	A parameter in Levenberg-Marquardt training algorithm
mu-max	Maximum value of mu
mu-dec	Decreased value of mu
mu-inc	Increased value of mu
min-grad	Minimum gradient
max-fail	Maximum validation failure
mem-reduc	Memory reduction
M_{age}	Ageing quenching method
M_{sol}	Solutionizing quenching method
n	Stress exponent for power law creep or grain boundary sliding
n	Net neural network input
n'	Cyclic strain hardening exponent
N	Number of cycles during fatigue
N_F	Number of cycles to failure
N_I	Crack initiation life
N_{Pexp}	Experimental crack propagation life
N_{Pcal}	Calculated crack propagation life
N_{Fexp}	Total experimental fatigue life
N_{FM}	Fracture mechanics fatigue life
p	Input to neural network
p_n	Normalized inputs
q	Grain size index
Q_v	Activation energy for volume diffusion
Q_{gb}	Activation energy for grain boundary diffusion
r	Average radius of grain boundary particles

r_y	Plastic zone radius
R	Correlation coefficient of linear regression analysis
R	Gas constant
R	Strain ratio in fatigue
t_{age}	Ageing time
t_{sol}	Solutionizing time
T	Temperature
T	Neural network target
T_{age}	Ageing temperature
T_{app}	Application temperature
T_m	Melting temperature
T/T_m	Homologous temperature
T_n	Normalized targets
T_{sol}	Solutionizing temperature
Tansig	Tan sigmoid transfer function
Trainbr	Bayesian Regularization training algorithm
Trainlm	Levenberg-Marquardt training algorithm
V_f	Volume fraction of γ' precipitate phase
w	Weight of a simple neuron
W	Wiggins superalloys Ltd.
X_k	Vector of current weights and biases
Y	Geometry factor in Paris equation
Y	Neural network output
α	Factor for the degree of coherency of particles
α	Thermal expansion coefficient
α_k	Learning rate in backpropagation training
γ	Performance ratio for Bayesian Regularization
γ	Gamma solid solution phase
γ'	Gamma prime precipitate phase
$\dot{\gamma}$	Shear strain rate

$\dot{\gamma}_0$	Pre-exponential constant for dislocation glide
$\dot{\gamma}_{DG}$	Shear strain rate due to dislocation glide
$\dot{\gamma}_{GBS}$	Shear strain rate due to grain boundary sliding
$\dot{\gamma}_{PLC}$	Shear strain rate due to power law creep
μ	Shear modulus
μ_o	Shear modulus at zero K
λ	Grain boundary precipitate spacing
$\Delta\varepsilon_t$	Total strain range
$\Delta\varepsilon_p$	Plastic strain range
$\Delta\varepsilon_e$	Elastic strain range
$\Delta\sigma$	Stress range
ΔF	Activation energy for dislocation glide
ΔK_{th}	Threshold stress intensity factor range
ΔK	Stress intensity factor range
ΔW	Hysteresis energy
ΔW_A	Hysteresis energy using area loop equation
ΔW_{NN}	Hysteresis energy using neural network
σ	Nominal applied stress
σ_{UTS}	Ultimate strength
σ_y	Yield strength
σ_c	Critical stress
σ_{max}	Maximum stress
σ_{min}	Minimum stress
σ_a	Alternating stress or stress amplitude
σ_m	Mean stress
ε_0	Instantaneous strain
$\dot{\varepsilon}_{GBS}$	Tensile strain rate due to grain boundary sliding
$\dot{\varepsilon}_{PLC}$	Tensile strain rate due to power law creep

τ_0	Flow strength of the solid at zero K
τ_b	Back stress due to carbides
τ_{ic}	Back stress due to dislocation climb
τ_{ig}	Back stress due to dislocation glide
τ_s	Applied shear stress
τ/μ	Normalized shear stress
% E	Percentage error

LIST OF ACRONYMS

ACC	Accelerated air cooling
AE	Acoustic emission
ANM	Adaptive numerical modeling
ANN	Artificial neural network
BPNN	Backpropagation neural network
CTE	Coefficient of thermal expansion
DMM	Deformation mechanism map
EPFM	Elastic plastic fracture mechanics
FC	Furnace cooling
FCC	Face centered cubic
GBS	Grain boundary sliding
HCF	High cycle fatigue
LCF	Low cycle fatigue
LEFM	Linear elastic fracture mechanics
NDT	Non-destructive testing
NN	Neural network
OQ	Oil quenching
PLB	Power law breakdown
PLC	Power law creep
RA	Reduction in Area
TBC	Thermal barrier coating
TCP	Topologically close-packed
TEM	Transmission electron microscope
TET	Turbine entry temperature
WQ	Water quenching

Chapter 1

Introduction, motivation and objectives

1.1 Introduction

Turbine components and aerospace engines operate at high temperatures and under severe thermal and mechanical loading conditions. Different stages of operations of turbines such as start, stationary, and stop phases are characterized by different temperature levels. Consequently, the complete cycle can feature substantial temperature variations resulting in severe thermo-mechanical stresses due to unequal thermal expansion of interacting components. Therefore, materials used in aerospace engines and turbine components are required to possess optimal thermal, mechanical, and microstructural properties. High temperature superalloys and steels are the two main material classes used in critical hot zones of turbines. Both materials classes have found widespread applications because of their excellent thermal, mechanical and physical properties including corrosion resistance, high strength coupled with ductility, creep and fatigue resistance, optimal impact and wear resistance properties at high temperatures. These materials contain many alloying elements such as Cobalt (Co), Chromium (Cr), Tungsten (W), Tantalum (Ta), Molybdenum (Mo), Niobium (Nb), Aluminum (Al), Titanium (Ti), etc. Superalloys are sub-divided into three broad classes: Nickel (Ni) based superalloys, cobalt (Co) based superalloys, and iron (Fe or Fe-Ni) based superalloys. The microstructure of most Ni based superalloys consists of a face centered cubic (FCC) γ matrix with a high volume fraction of an ordered intermetallic γ'

$Ni_3[Al,Ti]$ precipitate phase. The γ' precipitates are homogeneously distributed in the γ matrix. The microstructure of Ni based superalloys also contains other carbide and boride phases; however, their impact on high temperature properties is considered to be small. Among all phases, γ' precipitates are the main strengtheners in Ni based superalloys and are therefore responsible for key high temperature mechanical and microstructural properties [1]. The chemical composition and heat treatment of many Ni based superalloys must be well controlled to provide optimal volume fractions of γ' precipitates.

Similar to superalloys, high temperature steels owe their high temperature strength to appropriate medium to large grain size combined with a second phase which together limit grain boundary sliding that is the most critical deformation process at high temperature. In the case of 1.23Cr-1.2Mo-0.26V steel, the second phase is a dispersion of carbide particles.

The present work is a compilation of research undertakings aimed at establishing relationships and correlations between chemical compositions, heat treatments, microstructures, mechanical properties, thermal properties, and service lives of Ni based superalloys and 1.23Cr-1.2Mo-0.26V steel used in turbine components. Following the short motivation description below, an extensive literature review is presented in chapter 2. The modeling methodology and materials is described in chapter 3; results and discussion are outlined in chapter 4; main conclusions with some suggestions for future work are summarized in chapter 5.

1.2 Motivation and objectives

Aerospace engines and turbine components are subjected to complex thermal and mechanical stresses. Thermo-mechanical stresses are due to temperature gradients and are a function of the thermal expansion coefficient of the material. If these thermal stresses are sufficiently high, i.e. exceed the local strength of the material, yielding or cracking can result. Mechanical stresses caused by severe cyclic loading and vibratory motion of rotating components are superimposed to thermal stresses. In other words, the combined effect of complex thermal and mechanical stresses can promote nucleation and propagation of cracks, which can result in the failure of aero-engines and turbine components. In fact, fatigue and creep are the two main modes of failure of turbine components such as blades and discs that operate under complex thermo-mechanical loading conditions for extended periods of time. In order to improve the performance and durability of aero-engines and turbine components, substantial efforts have been made in the past decades to optimise component design, manufacturing methods, and materials. To estimate the reliable service life of these components, numerous fatigue and creep equations have been derived based on laboratory experiments. But in practice, the environment experienced by these components is difficult to replicate exactly in the laboratory. Specifically, long-term factors such as oxidation, corrosion, and material degradation are often underestimated in a laboratory setting. The neural network modeling could be a more accurate tool to predict highly non-linear multi-dimensional relationships. It is a flexible modeling technique that works similar to the human brain and is capable of solving complex problems without any mathematical relationship between various operating parameters. This method also reduces the need for experimental work and time consumed in deriving the equations. Therefore, the neural network is investigated in this study as a modeling tool to predict the γ' precipitate size, thermal expansion coefficient as well as fatigue damage in γ' precipitate strengthened Ni based superalloys. In addition, a deformation mechanism map is constructed for 1.23Cr-1.2Mo-0.26V steel, also widely used in turbine components.

Specifically, the objectives of this thesis are to

1. Model and compare the γ' precipitate sizes of various Ni based superalloys using Levenberg-Marquadt and Bayesian Regularization backpropagation neural network training methods.
2. Model the thermal expansion coefficient of various γ' precipitate strengthened Ni based superalloys.
3. Determine and compare the fatigue lives of various γ' precipitate strengthened Ni based superalloys using fracture mechanics and neural network approaches.
4. Determine and compare the hysteresis energies and fatigue damages of various γ' precipitate strengthened Ni based superalloys used for turbine disc using hysteresis area and neural network approaches.
5. Construct the deformation mechanism map for 1.23Cr-1.2Mo-0.26V steel using dislocation glide, grain boundary sliding, and power law creep rate equations and verify the map with experimental data and neural network results.

Chapter 2

Literature review

A great deal of research has been conducted on various physical, thermal, and mechanical aspects of alloys used for aero-engines and turbine components. This literature review summarises information on alloys used in different turbine parts operating under high temperature and severe loading conditions.

2.1 Superalloys

The term superalloy came around World War II and the demand for this new class of alloys in aero-engines and turbine components increased rapidly because they retain their strength and oxidation resistance at high temperatures in contrast to most other material classes. The use of Co and Fe based superalloys is limited as compared to Ni based superalloys primarily due to higher costs and lower corrosion resistance respectively. The application conditions, properties, microstructures, strengthening mechanisms, heat treatment, etc. are explained in the following paragraphs.

2.1.1 Application conditions

Modern aero-engines are designed with great emphasis on continuously increasing the turbine entry temperature (TET) which varies greatly during a typical flight cycle. It is highest during take-off and climbing to cruising altitude (approximately 1480^{o}C). The variation of the TET during a typical flight cycle of a civil aircraft is shown in Figure 2.1 [1]. This variation in temperature results in high thermal stresses whereas high speed rotation of turbine engines results in mechanical stresses. The combined effects of thermal and mechanical stresses promote the nucleation of cracks that can lead to failure of turbine components. Apart from thermo-mechanical stresses, turbine components also face severe environments (corrosive and erosive) that accelerate the nucleation of cracks and ultimately lead to failure of turbine components.

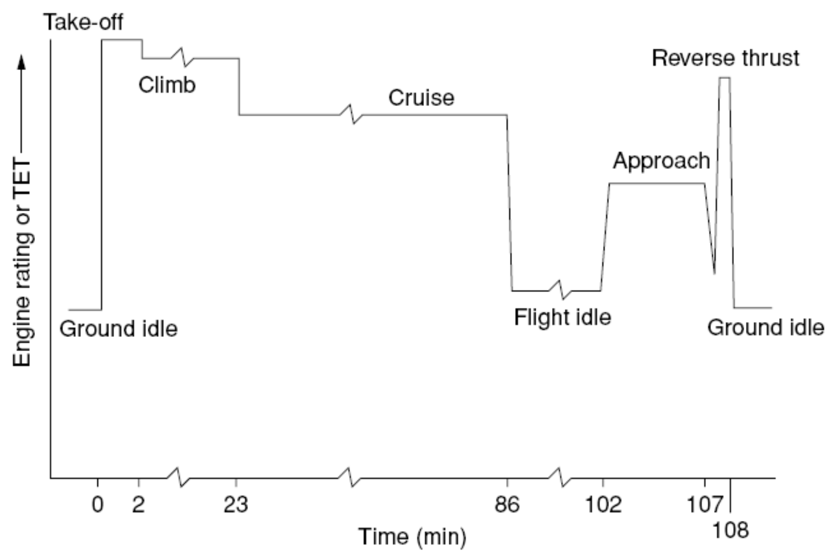

Figure 2.1: Variation of the TET during a typical flight cycle of a civil aircraft [1].

2.1.2 Properties of superalloys

Superalloys used under severe conditions must demonstrate good mechanical, physical, and thermal properties. High and low cycle fatigue (HCF and LCF) resistance and creep resistance are of key importance. These two important properties will be illustrated in detail in later sections. Good ductility, wear resistance, and good impact resistance need to be maintained. The properties of superalloys strongly depend on the microstructure. Therefore, an accurate control over phases created in the alloy as well as an optimization of morphology and distribution of γ' precipitates is necessary in order to ensure appropriate high temperature properties of Ni based superalloys.

The magnitude of thermal stresses resulting from temperature variations depends on the thermal expansion coefficient [2]. Therefore, the thermal expansion coefficient is one of the most important design factors for turbine blades and other components to reduce thermal stresses and minimize expansion since components are often operated under close tolerances. There is a strong correlation between the thermal expansion coefficient, operating temperature, chemical composition, elastic modulus and morphology (size and shape) of γ' precipitates. Previous research has attempted to measure or derive the thermal expansion coefficient of Ni based superalloys. Sung and Poirier compiled data for Ni based superalloys from various sources and derived an equation based on regression analysis for coefficients of thermal expansion (CTE) as a function of composition and temperature only. They also stated that Ni based superalloys containing both γ' particles and γ matrix have smaller CTEs than do single phase (γ) alloys [3]. Balikci et al. measured thermal expansion coefficient of a suitably heat treated and aged polycrystalline superalloy, IN738LC (a turbine blade material) with various γ' precipitate microstructures (fine, medium, course, and duplex) and annealing textures. They correlated the thermal expansion coefficient to the preferred orientation and elasticity modulus under different microstructural conditions. They found that coarse and medium size precipitates with low elasticity modulus values yield the highest thermal expansion coefficients while fine size precipitates have lower thermal expansion coefficients at all temperatures and the duplex size precipitate microstructure shows the lowest thermal expansion coefficient. The thermal expansion is an elastic dilatation; thermo-mechanical forces can result if there are any confinements that prevent free and complete expansion of components. Residual and interfacial stresses, abrupt compositional changes, and deviations from an homogeneous phase distribution also affect the thermal expansion behaviour of components. Hence, processing and fabrication methods and uniformity of the resultant microstructure are important in determining the overall thermal behaviour [4]. Li and Mills studied the effect of γ' content on the densities of Ni based superalloys and concluded that an increase in γ' phase content results in an increase in the density and a decrease in the thermal expansion coefficient. In the relevant turbine application temperature range between 800°C and 1000°C, the temperature dependence of the thermal expansion coefficient increases as the size of γ' particles increases [5]. Raju et al. estimated the thermal expansion coefficients as a function of temperature of Inconel-600® by using high temperature X-ray diffraction technique in the temperature range 25-923°C and found a fair degree of agreement with other existing dilatometer based bulk thermal expansion estimates [6]. Abel and Bozzolo introduced a simple algorithm for the determination of thermal expansion coefficients of pure elements and their alloys based on features of the binding energy curve using single elements, an intermetallic alloy and Ni based superalloys as examples. This approach is limited to low temperatures and provides only a rough estimate for higher temperatures [7]. Based on a previously proposed algorithm [7] exclusively built for the calculation of the coefficient of thermal expansion, they proposed an algorithm for the calculation of general thermal properties, i.e., coefficient of thermal expansion, equilibrium volume, energy of formation, and compressibility of multicomponent systems, and suggested that this algorithm might be useful when experimental data is either limited or unavailable [8].

Other desired properties of superalloys include low density to reduce weight; high fracture energy to prevent failure; and good oxidation and hot corrosion resistance to fight corrosive and erosive attacks [9].

2.1.3 Main phases in Ni based superalloys

The microstructure of most Ni based superalloys consists of at least two phases: ordered γ' and disordered γ. The fundamental properties of superalloys depend on these two common phases. Other phases such as carbides, borides, and topologically close-packed (TCP) phases are also found in superalloys, but their impact on properties is minimal. The phases of most Ni based superalloys are briefly described in the following paragraphs.

Gamma phase (γ): It is a continuous matrix, FCC Ni based austenitic phase, in which other phases reside. The stability of the γ phase with respect to other possible crystal structures is very important since any phase transformations, either during thermal cycling or during extended periods of operation, would affect high temperature properties. It contains a high percentage of solid solution formers such as Co, Cr, Mo, and W, thereby giving rise to solid solution strengthening. The increase in strength depends on the differences in atomic sizes between the base Ni and substitutional atoms. Cr, Mo, and W are strong solid solution strengtheners. In contrast, Co, Fe, Ti, and Al have minor solid solution strengthening effects that contribute more to either improve the corrosion resistance or increase strength by precipitation strengthening [1].

Gamma prime phase (γ'): The γ' precipitate, an intermetallic compound of nominal composition Ni_3Al, can be obtained by ageing the solution treated alloys. It is the most important phase because it plays a significant role in strengthening of Ni based superalloys by hindering the movement of dislocations. Its crystal structure consists of Al atoms at the unit cell corners and Ni atoms at the face centers (see Figure 2.2).

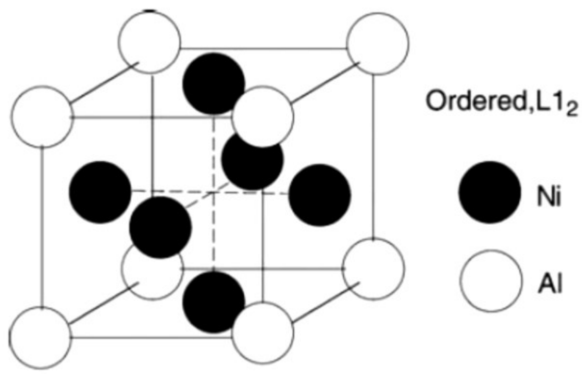

Figure 2.2: Arrangements of Ni and Al atoms in the ordered Ni_3Al phase [1].

Depending on heat treatments and chemical compositions, different sizes of γ' precipitates, i.e. fine, coarse, and duplex (both primary and secondary γ') can be formed. Figure 2.3 shows the microstructure of IN738LC, a Ni based superalloy, used in turbine blades [10]. Primary (medium or coarse) and secondary (fine) γ' precipitates are homogeneously distributed in the γ matrix [10].

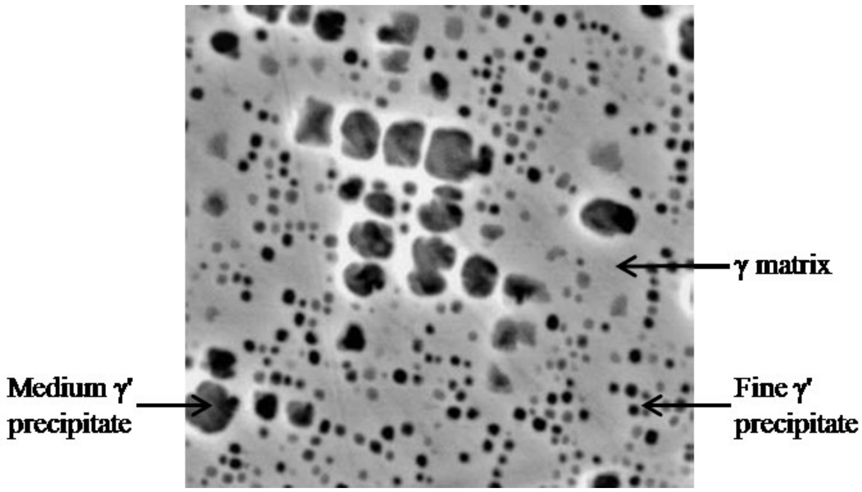

Figure 2.3: Microstructure of the Ni based superalloy IN738LC [10].

2.1.4 Strengthening mechanisms

Strengthening of superalloys is required in order to obtain the desirable high temperature properties. Solid solution strengthening, precipitation hardening, and carbide precipitation (grain boundary strengthening) are the three main strengthening mechanisms. All strengthening mechanisms rely on a simple principle, i.e. restricting or hindering dislocation motion, thus impeding plastic deformation, which makes materials harder and stronger as the strength is inversely related to dislocation mobility [2]. The creep resistance and yield strength anomalous behaviour in Ni based superalloys are some of the effects of the interactions between different strengthening mechanisms and dislocations.

2.1.4.1 Solid solution strengthening

Solid solution strengthening is the addition of impurity atoms or alloying elements that take substitutional or interstitial positions without any change in the crystal structure of the host material. Alloying elements either smaller or larger than the host atom impose lattice strains (tensile or compressive) on the surrounding atoms which restrict dislocation movement. Therefore, a greater applied stress is necessary in order to initiate and then continue plastic deformation resulting in the enhancement of strength and hardness. Higher concentrations of the impurity atoms provide stronger strengthening effects [1,2].

2.1.4.2 Precipitation strengthening

The strength achieved through precipitation hardening is related to the degree of coherency between the precipitate particles and the matrix, which, in turn, depends critically on the lattice misfit. The misfit between γ' and γ phases plays an important role in determining the morphology of γ' precipitates whereas the morphology of γ' precipitates plays an important role when considering dislocation-precipitate interactions. The lattice parameters of γ' and γ phases are very similar and the lattice misfit is small. These result in coherent γ/γ' interfaces that guarantee low interfacial energy which is essential for a stable microstructure and improves properties at elevated temperatures [1]. Precipitate cutting and Orowan looping are the two mechanisms that take place at γ' particles during plastic deformation of Ni based superalloys. When a mobile dislocation encounters a γ' precipitate, the dislocation either shears the precipitate or bypasses it by Orowan looping. When the precipitate size is small, cutting or shearing is the dominant strengthening mechanism whereas Orowan looping or bypassing dominates at large precipitates. Careful control of the γ' precipitates size results in the optimum hardness (strength) which is usually attained at the transition point between precipitate cutting and looping mechanisms. It is believed that both Orowan looping and particle cutting phenomena are at play at high temperatures to provide the observed strengthening effect [11,12].

2.1.4.3 Grain boundary strengthening

Various carbides and borides segregate at γ grain boundaries. The actual type of carbides and borides depends on the alloy composition and processing conditions employed. Carbides and borides improve high temperature creep properties of the superalloys via the inhibition of grain boundary sliding [1].

2.1.4.4 Yield strength anomalous behaviour

One example of interaction between γ' precipitates and dislocations is the anomalous yield behaviour which is a remarkable characteristics exhibited by γ/γ' Ni based superalloys (Figure 2.4) [1,13]. The anomalous behaviour is caused by dislocation arrangement into pairs called super-dislocations (Figure 2.5) and the different temperature dependent configurations of super-partial dislocations of such pairings as they cut through γ' particles [2,13-15]. The yield strength is a sensitive function of the γ' phase, which, in turn, depends on the fraction, size, and distribution of γ' particles, and hence on the heat treatment applied. The strength of metals and alloys normally decreases when temperature increases owing to the thermally assisted movement of dislocations. In contrast, in case of superalloys, the yield strength increases with temperature up to approximately 600^{o}C to 800^{o}C. Above this range, the yield strength decreases quickly as the temperature further increases toward about 1200°C [1,13]. This is ideal for turbine blades as their stationary operating temperature is approximately 800-1000°C [1].

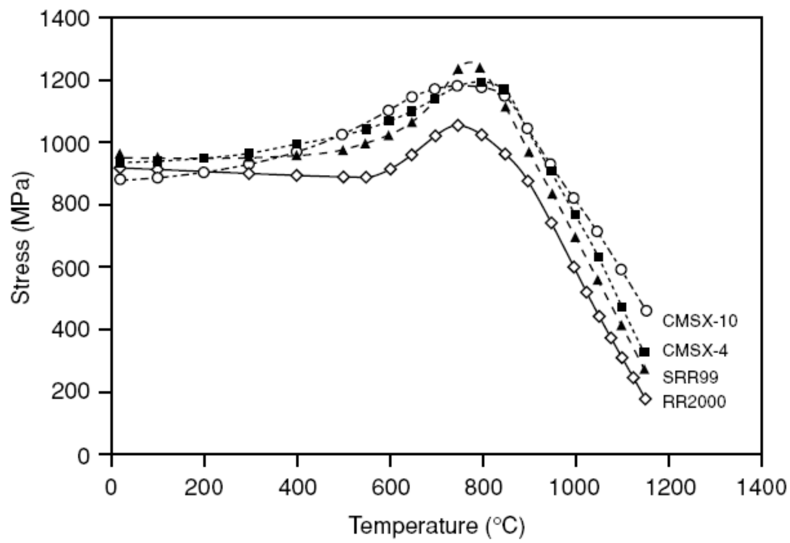

Figure 2.4: Yield stress vs. temperature of a number of superalloys. The anomalous behaviour is illustrated by the yield strength increase up to a peak at about 900°C [1].

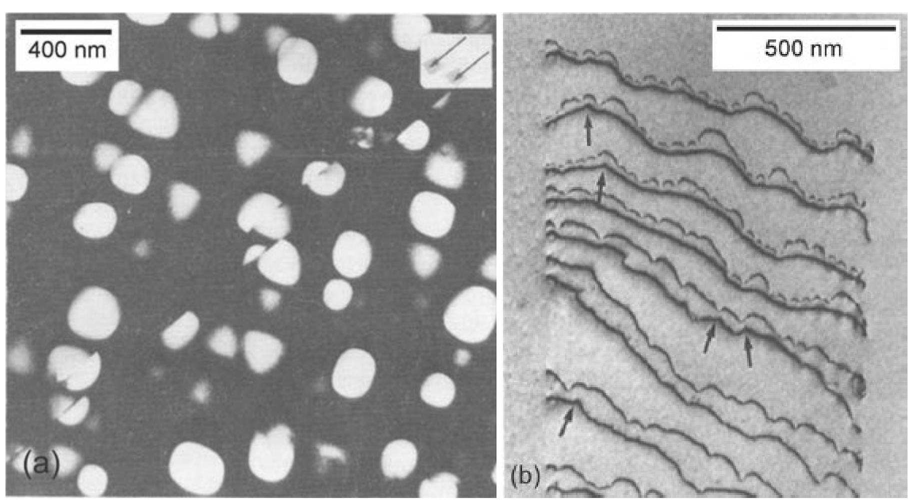

Figure 2.5: Transmission electron micrographs showing dislocations travel through the γ/γ' microstructure in pairs: (a) Dark-field micrograph of sheared particles in Nimonic 105; and (b) Pairs of edge dislocations in Nimonic PE16 after unloading [1,14,15].

2.1.5 Heat treatment

Commonly employed procedures to form γ' precipitates in superalloys are solution and precipitation heat treatments that can best be explained using corresponding phase diagrams along with temperature vs. time plots as can be seen in Figure 2.6 [2,16]. The first step is usually a solution heat treatment which consists in heating the alloy to the γ single phase region (temperature T_o for instance in Figure 2.6 for the alloy of composition C_o) where all solute atoms are dissolved to form a relatively soft and homogeneous single phase solid solution. The solutionizing temperature T_o depends on the properties desired. This procedure is followed by quenching to freeze the solutionized supersaturated state. In some cases, very fine precipitates may also form during quenching. Accelerated air cooling (ACC), oil quenching (OQ), and water quenching (WQ), common quenching methods, are employed during heat treatment. For precipitation heat treatment, the supersaturated solid solution is heated to the two-phase (γ'+γ) region to an intermediate temperature (temperature T_2 in Figure 2.6 for the alloy of composition C_o) where the diffusion rate is appreciable and γ' precipitates form within the γ matrix as dispersed particles. After an appropriate ageing time, the alloy is cooled to room temperature [2]. Often, double or multiple ageing treatment steps are employed depending on the alloy type and design objectives in order to control the size and distribution of γ' precipitates and improve strength and rupture life [2]. The first step at relatively high temperature can produce coarser particles while finer secondary precipitates can be produced within the γ channels either at lower ageing temperatures or during cooling.

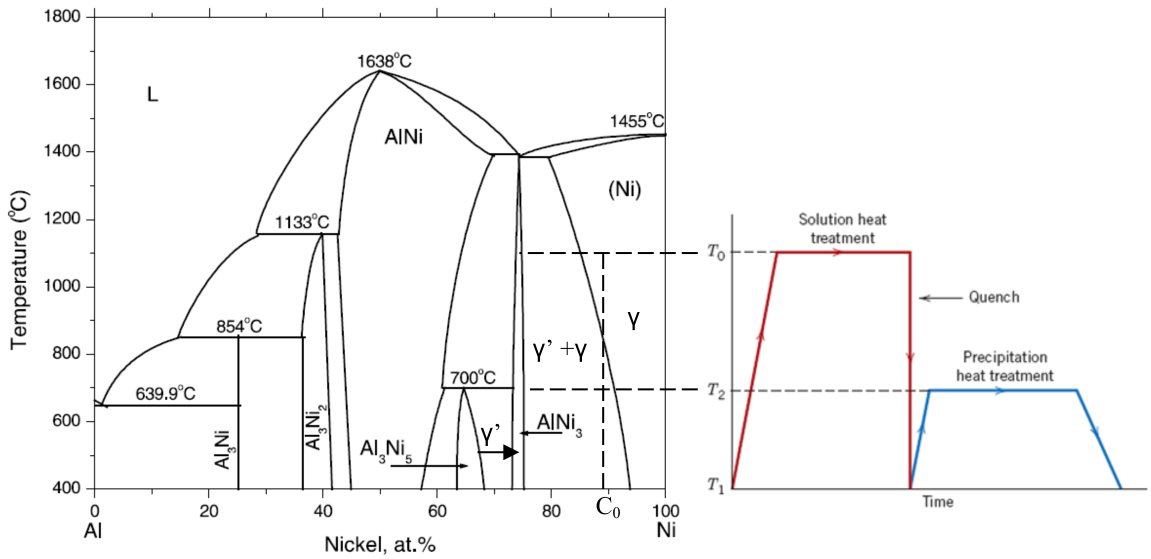

Figure 2.6: Binary Ni-Al phase diagram with solution and precipitation heat treatments [2,16].

2.2 Cr-Mo-V steel

Cr-Mo-V is a high temperature steel widely used for critical components in steam turbine rotors. The alloy primarily possesses a tempered martensitic microstructure with a prior austenite grain size of 100 µm containing various types of carbides/precipitates, namely Fe_3C as inter-granular precipitate and V_4C_3, Mo_2C (needle) as trans-granular dispersions. The high creep strength of Cr-Mo-V steel is caused by precipitation strengthening due to these uniformly dispersed carbides [17].

2.3 Failure modes

As already mentioned in previous sections, the combined effect of complex thermal and mechanical stresses promotes the nucleation and propagation of cracks that give rise to fatigue and creep failure of gas turbine blades and other components interacting with them. The creep of high temperature materials is described in section 2.3.2. Fatigue characteristics and damage mechanisms are explained in section 2.3.1 below.

2.3.1 Fatigue

Fatigue is the general phenomenon of material failure that occurs in structures subjected to dynamic and fluctuating stresses to a stress level considerably lower than the tensile or yield strength [18,19]. Each stress cycle causes some degradation or damage of the material or component. It is the single largest cause of failure in metals and is one of the major causes of failure of turbine components. Fatigue failure is catastrophic and insidious, occurring very suddenly and without any remarkable overall plastic deformation warning. Even ductile metals fail in a brittle manner during fatigue. The standard definition of fatigue as stated by ASTM, contained in ASTM E 1150 is "the process of progressive localized permanent structural change occurring in a material subjected to conditions that produce fluctuating stresses and strains at some point or points that may culminate in cracks or complete fracture after a sufficient number of fluctuations" [20].

2.3.1.1 Fatigue stages

Fatigue failure consists of three stages, namely, crack initiation, crack propagation, and final fracture. Each of these stages is an extremely complex process. Crack initiation can be defined as the generation, nucleation or formation of small cracks that can be detected by a reliable non-destructive testing (NDT) technique or by any other means. Cracks generally nucleate at oxide films, inclusions, pores, intermetallic phases, grain boundaries, slip-bands, machined surfaces, twin boundaries, second phases, notches, surface scratches, sharp fillets, keyways, threads, dents, and microscopic surface discontinuities. These nucleation sites serve as the points of stress concentrations or stress raisers. A crack initiated at a pore of a Ni based superalloy is shown in Figure 2.7 [21,22].

In the fatigue crack propagation stage, the crack advances incrementally with increasing number of stress cycles that create beach-marks and/or striations on the fracture surface [2].

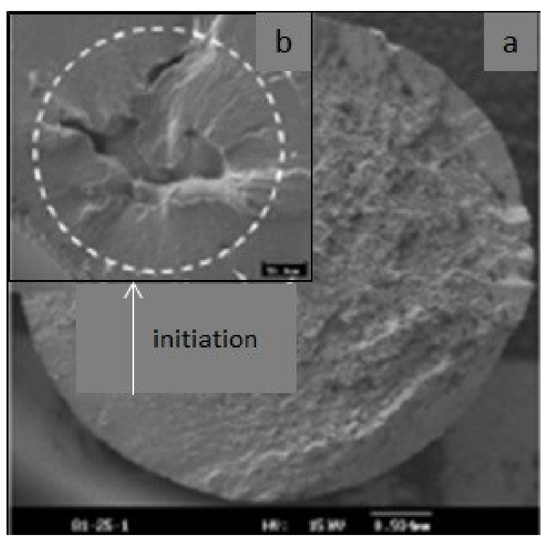

Figure 2.7: Fracture surface of a Ni based superalloy (a), crack initiation at a pore (see arrow) is magnified in Figure (b) [21,22].

2.3.1.2 High cycle and low cycle fatigue

High cycle fatigue (HCF) and low cycle fatigue (LCF) are the two regimes of fatigue loading. HCF primarily results from the motion of rotating components as well as resonances. In HCF, a linear elastic behaviour is observed and is often characterised by smaller stress amplitudes and larger numbers of cycles in excess of 10^8. However, more technological advancements resulted in extremely highly loaded components such as turbine blades and discs, the occurrence of plasticity led to another fatigue regime called LCF. LCF conditions are primarily caused by thermal stresses resulting from a restriction in thermal expansion of components and from engine start-ups and shut-downs when the load changes from zero to the maximum and back to zero. In most cases, the service lives of turbine components covers less than 10^5 LCF cycles which are characterised by relatively high stress amplitudes [2,23]. During LCF, a hysteresis loop develops between stress and strain which indicates the partitioning of the response into elastic and plastic strain contributions. The terms related to the stable hysteresis loop are explained in Figure 2.8: the width $\Delta\varepsilon$ represents the total strain range and the height $\Delta\sigma$, the stress range. The hysteresis loop equation is the most commonly used method for estimating the hysteresis energy that can be given by [24]:

$$\Delta W = \frac{\Delta\sigma\Delta\varepsilon_p}{1+n'} \tag{1}$$

where $\Delta\varepsilon_p$ is the plastic strain range and n' is the cyclic strain hardening exponent.

Fatigue fracture occurs after the material has accumulated a critical amount of energy over a given number of cycles called service life. The hysteresis energy can be used for total fatigue damage prediction.

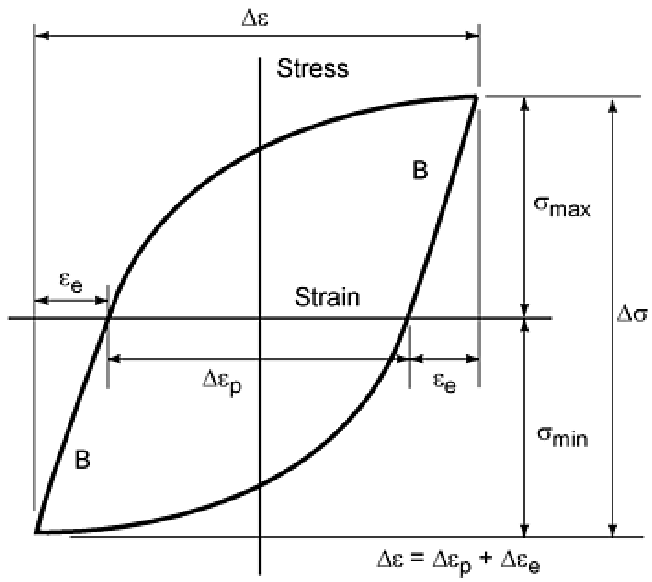

Figure 2.8: Stable hysteresis loop developed during low cycle fatigue [19].

2.3.1.3 Fracture mechanics

Fracture mechanics describes relationships between the material properties, stress levels, presence of crack-producing flaws, and crack propagation mechanisms. This leads to an important link between fracture mechanics and fatigue [25]. Small, microscopic flaws or defects (cracks) exist under normal conditions at the surface or within the interior of components, which create strong local stress concentrations. These stress fields can generate plastic zones (of radius r_y) where the work is done against plastic and frictional forces [25]. The local stress depends on the crack orientation and geometry. It is highest close to the tip of the crack and decreases with distance away from the crack tip. Local yielding occurs if the local stress reaches the yield strength, σ_y. Figure 2.9 shows an illustration of the plastic zone and the local stress distribution at the tip of a crack [25].

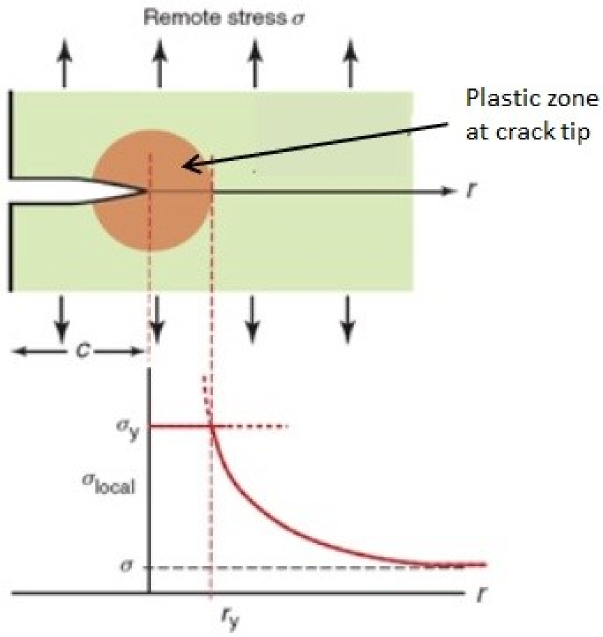

Figure 2.9: Plastic zone and stress distribution at a crack tip [25].

The stress intensity factor (K), defined by equation (2) for the linear fracture mechanics case, controls the stress and energy state near the crack tip, and consequently the fracture process.

$$K = Y\sigma\sqrt{\pi c} \tag{2}$$

The fatigue stress intensity factor range ΔK can then be defined using equation (3) as:

$$\Delta K = K_{\max} - K_{\min} = Y\Delta\sigma\sqrt{\pi c} \tag{3}$$

where Y is a function depending on the geometry and loading conditions; σ is the nominal applied stress; and c is the crack depth. Linear Elastic Fracture Mechanics (LEFM) and Elastic Plastic Fracture Mechanics (EPFM) are the two sub-branches of fracture mechanics used to describe the stress field around the crack tip. LEFM is applicable to fatigue crack growth when the deformation at the crack tip is mostly elastic and the size of the plastic zone near the crack tip is very small (generally smaller than the crack size or grain size). In addition, the material should be isotropic and homogeneous around the crack. If these conditions of LEFM are not fulfilled, then EPFM is used. But, due to complexity in EPFM, it is not as well developed as the LEFM concept. Therefore, LEFM principles are most frequently applied to solve fatigue crack growth problems. As the crack grows and increases in length during fatigue, the stress intensity factor range ΔK increases with time under constant cyclic stress as can be seen in Figure 2.10.

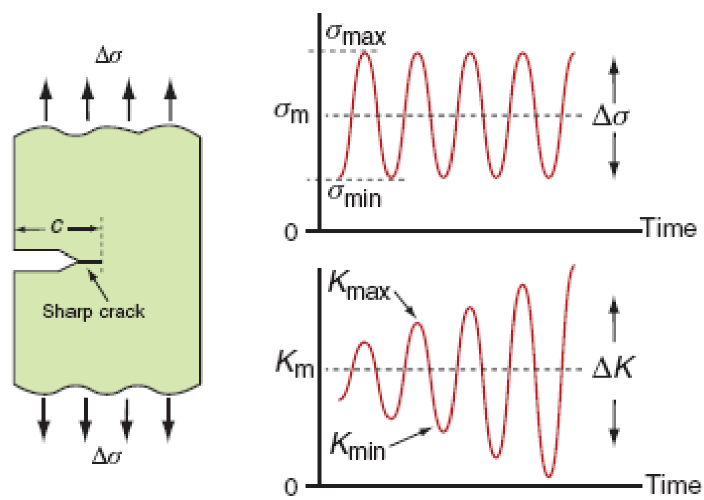

Figure 2.10: Cyclic loading of a cracked component [25].

The crack growth per cycle, dc/dN, increases with ΔK as illustrated in Figure 2.11 [25]. There are three main stages in the curve:

In the first stage, below the threshold stress intensity factor range (ΔK_{th}), non-propagating cracks exist, but there is no observable fatigue crack growth. The second stage is the most important and describes a linear relationship between log(dc/dN) and log(ΔK) through the Paris equation written as:

$$\frac{dc}{dN} = A(\Delta K)^m \tag{4}$$

where A and m are material constants.

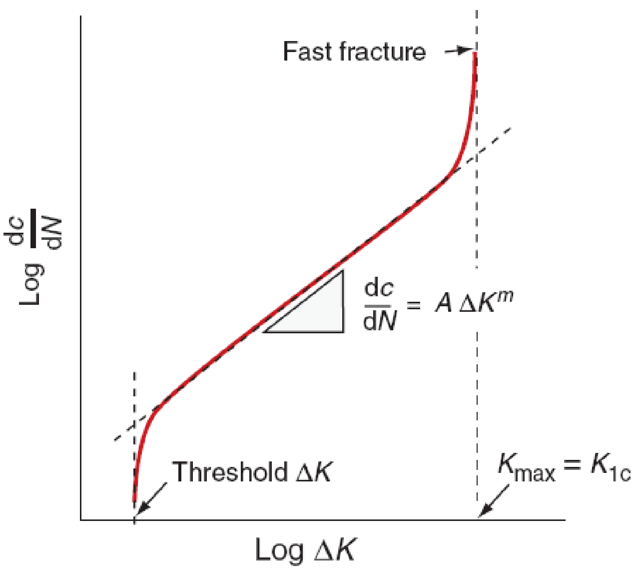

Figure 2.11: Crack growth rate dc/dN vs. ΔK in a log-log scale [25].

The fatigue crack propagation life of a component can be obtained by integrating equation (4) between the limits of the initial crack size, c_0, and the critical crack size for sudden fracture, c_f, as:

$$N = \int_{c_0}^{c_f} \frac{1}{A \cdot \Delta K^m} dc \tag{5}$$

yielding

$$N = \frac{1}{\frac{(m-2)}{2}\pi^{m/2} A Y^m (\Delta\sigma)^m c_0^{(m-2)/2}} \left[1 - \left(\frac{c_0}{c_f} \right)^{(m-2)/2} \right] \tag{6}$$

For the special case of m = 2, equation (6) can be simplified to:

$$N = \frac{1}{\pi A Y^2 (\Delta\sigma)^2} \ln\left(\frac{c_f}{c_0} \right) \tag{7}$$

In the third stage of Figure 2.11, an accelerated crack growth occurs leading to unstable fracture when the stress intensity factor reaches the fracture toughness (K_{IC}) of the material. The fracture toughness is a measure of a material's resistance to brittle fracture when a crack is present. It depends on many factors, the most influential of which are temperature, strain rate, and microstructure. Ductile materials have large values of K_{IC}, but brittle materials have low values of K_{IC} which make the material vulnerable to catastrophic failure [2].

Traditionally, component life estimation is based on a combination of the crack initiation life and the crack propagation life determined by the fracture mechanics approach. Equations (6) and (7) are generally used for the crack propagation life prediction in which the crack initiation life is added to obtain the total fatigue life.

2.3.1.4 Fatigue life prediction and fatigue damage

Several fatigue life prediction methods such as Basquin law, Coffin-Manson law, frequency modified damage function model, strain range partition, and so on have been developed to predict fatigue life. Lee et al. successfully used different methods for predicting the high temperature low cycle fatigue performance of five Ni based superalloys (Inconel 718 HIP, Inconel 718 HIP and heat treated, MAR-M-247 HIP, MAR-M-247 HIP and heat treated, and Rene 95 HIP) based on tensile and LCF tests. They also developed a novel equation to predict the LCF of HIP superalloys as well as of cast Rene 80 at elevated temperatures [26]. Several studies have also been done to relate the hysteresis energy to the total fatigue damage and fatigue life. It was suggested that the hysteresis energy associated with plastic deformation per unit volume in a cycle is a measure of the damage in the material and can be used as a parameter to predict the fatigue life [27]. Mathew et al. conducted experiments on a Ni based alloy, Nimonic PE16, to investigate the deformation behaviour under monotonic and cyclic loading conditions with and without holding time. They applied different life prediction models based on the concepts of hysteresis energy, strain range partitioning, and micro-mechanistic damage to analyse experimental fatigue life data. They concluded that the fatigue life is not only determined by the magnitude of plastic strain but also by the nature of the strain, which, in turn, controls the type of damage [28]. Under random loading conditions, Tchankov and Vesselinov developed a new incremental method, based on the Von Mises material behaviour, for the calculation of dissipated hysteresis energy to failure that can be used as a fatigue life parameter. They further concluded that failure occurs when a critical boundary value for dissipated energy is reached. The advantage of this method is that it does not use a cyclic counting procedure. This approach is not limited to high or low cycle fatigue and can easily be extended to a multiaxial state of stresses [29]. Recently, Mazari et al. proposed an analysis of fatigue crack propagation based on energetic approach and expressed a unique linear relation between the crack growth rate and the hysteretic energy per cycle [30]. Daubenspeck and Gordon used a combination of extrapolation and estimation techniques to develop a method to accurately characterize high stress amplitude LCF of IN738LC using experimental data at different temperatures in order to evaluate and examine the validity of extrapolation based on hysteresis energy trends [31].

Many damage accumulation models have also been formulated on the ground of experiments or theoretical analyses for different material classes. For Ultimet superalloy, Jiang et al. used the integrated approach of combining non-destructive evaluation, microstructural investigation, and fatigue testing to characterize the fatigue damage of utilized acoustic emission, used for identifying the positions of the crack initiation, and positron lifetime spectroscopy, a sensitive non-destructive technique to reveal the fatigue damage. They found that the results of acoustic emission system were generally in good agreement with those of the average positron lifetime by positron spectroscopy [32]. Kim et al. developed a robust experimental procedure with repeatable measurements of the acoustic non-linearity parameter to track the evolution of fatigue damage in a Ni based superalloy subjected to both high and low cycle fatigue. These non-linear ultrasonic results indicate that the fatigue damage associated with HCF is relatively localized, while the damage associated with LCF is more evenly distributed. One application of the measured acoustic non-linearity parameter vs. fatigue life data is to potentially serve as a master curve for life prediction based on non-linear ultrasonic measurements [33]. Ramkumar et al. correlated an increase in the non-linearity parameter resulting from harmonic generation from a failed fatigued sample of DA718, a Ni based superalloy, that exhibits planar slip, and consequently dislocation pile-ups using transmission electron microscope (TEM) observations of the dislocation structure in fatigued samples. They found that theoretical estimates of the increase in non-linearity parameter based on TEM measurements were close to experimental ultrasonic measurements [34]. Seweryn et al. proposed the model of damage accumulation for analysis of fatigue life of structural elements under non-proportional loading states and concluded that increment of damage accumulation depends on increments of dissipation of energy and stress condition. Their model enabled to define the number of cycles or the time of safe application of complex fatigue loads in many engineering applications [35].

2.3.2 Creep

Materials used for elevated temperature applications are generally subjected to time-dependent and permanent deformation called creep which limits the lifetime of the components [36]. The fact that creep is a function of temperature and time indicates that it is a thermally activated process. The type of the material, the microstructure, and the service environment affect creep behaviour. For metals, creep becomes important at temperatures above the recrystallization temperature when atoms become mobile allowing time-dependent rearrangement of the microstructure [18,20,36,37]. The knowledge of creep characteristics of a material allows the design engineer to ascertain its suitability for a specific application. Turbine components are machined to tight tolerance with respect to the engine housing and are subjected to elevated temperatures under low to medium stresses for a prolonged time. Therefore, creep is one of the major modes of damages of turbine components in which a plastic and irrecoverable strain accumulates overtime causing unacceptable elongation or even failure of components. Figure 2.12 is an example of failure of a turbine blade due to creep deformation [37].

Figure 2.12: Typical creep deformation in a jet-engine turbine blade [37].

2.3.2.1 Creep deformation

It is believed that more than one creep mechanism, discussed in section 2.3.2.2, can operate at the same time. Typical creep curves show the strain as a function of elapsed time for constant load or stress and temperature. In engineering situations, constant load tests are more important because the load is maintained constant in real applications. However, to better understand the mechanisms of creep, constant stress tests are employed [2]. Figure 2.13 (a) illustrates the idealized shape of a creep curve of a material under a constant load and (b) shows the corresponding variation of the creep rate [38]. The shape of the creep curve depends on the material's chemical composition, microstructure, and operating conditions. There is an instantaneous elastic deformation, as indicated in the Figure, resulting from the application of the load. The instantaneous strain is not considered creep and may constitute a substantial fraction of the total strain.

It should be subtracted from the total strain to give the creep strain [23]. This strain should also be considered in design studies and failure analysis.

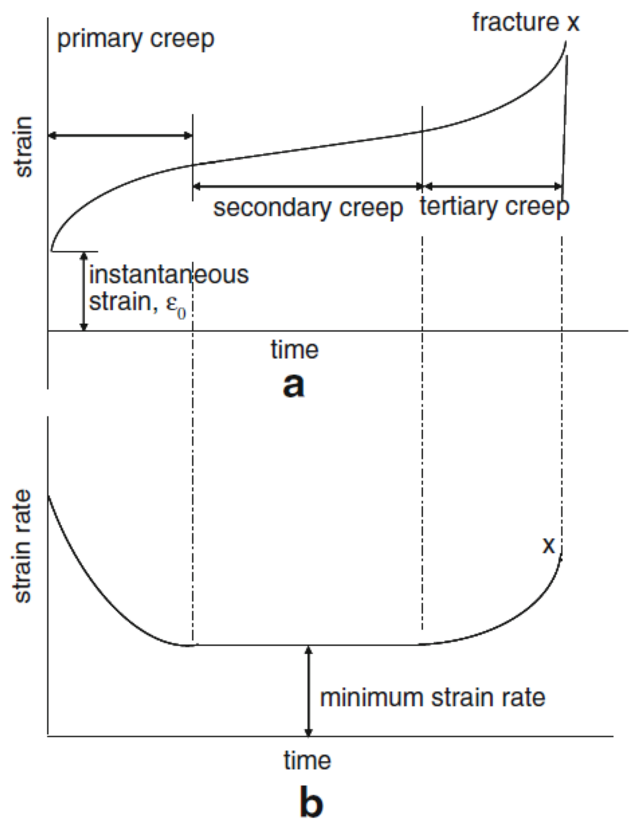

Figure 2.13: (a) A schematic creep curve showing three stages of creep and an instantaneous elongation on application of load; (b) schematic strain rate plot vs. time [38].

The resulting creep curve consists of three stages, namely, primary or transient creep, secondary or steady state creep, and tertiary creep [38]. The degree to which these three stages can be distinguished depends on the material, temperature, and applied stress. The slope of the curve is called creep rate [2,20,36,38]. Both constant load and constant stress exhibit similar creep behaviour except in constant stress the onset of tertiary creep is delayed.

The primary creep phase exhibits a continuously decreasing creep rate because creep resistance or strain hardening of the material increases and further deformation becomes more difficult as the material is strained [1,2]. In the secondary creep phase, the creep rate reaches a steady state; the deformation rate is minimal and almost constant. The steady state creep represents a balance between work hardening and recovery; it usually covers an overwhelming fraction of the total creep life. Therefore, the secondary or minimum creep rate is the most important engineering design parameter and is widely used in research and engineering studies [36,37].

In the tertiary creep phase, the creep rate increases due to microstructural and metallurgical changes such as grain boundary separation, formation of internal cracks, cavities, voids, necking, coarsening of precipitates, etc. All these factors cause a decrease in the effective cross-sectional area and an increase in strain rate. Oxidation also reduces the cross-sectional area and leads to increased creep rate. In designing components for service at elevated temperatures, the creep resistance is primarily considered using data of elapsed time and extension that precede tertiary creep. However, the safety factor can include the tertiary creep phase in which defects can be detected before catastrophic failure occurs [2,36,37].

2.3.2.2 Mechanisms of creep deformation

Creep deformation is based on mechanisms such as slip, sub-grain formation, diffusion, and grain boundary sliding that occur at high temperatures [23,37]. It is believed that new slip systems become operative at high temperatures that allow slip to be easier than at low temperatures. At high temperatures, sub-grain structures are formed due to excess dislocations and grains can slide past each other. Moreover, grain boundary migration can take place allowing grain boundaries to move normal to their surface under the influence of shear stresses that help to relieve strain concentration. Thus, both grain boundary sliding and grain boundary migration play a major role in high temperature creep [23,38].

Dislocation glide: The motion of dislocations in slip systems, defined by slip planes and slip directions, is called dislocation glide. The impediment of dislocation glide by obstacles such as precipitates, dispersoids, solute atoms, and other dislocations determines the creep rate in this mechanism [23,39,40].

Dislocation creep or power law creep (PLC): Dislocation creep consists of dislocation motion non-parallel to the Burgers vector to overcome barriers by thermally assisted mechanisms such as diffusion of vacancies or atoms. During dislocation creep, the steady state rate represents a balance between strain hardening and recovery by rearrangement and annihilation of dislocations [23,38,40]. It has been shown that dislocation climb normal to the Burgers vector plays a major role in dislocation creep. Atomic diffusion is the rate controlling mechanism because the dislocation climb requires diffusion of vacancies or atoms as illustrated in Figure 2.14 where many adjacent atom movements are required to produce climbing of an entire dislocation line [18]. The rate equation empirically describing balanced hardening and recovery processes can be given as [40]:

$$\dot{\varepsilon}_{PLC} = A_{PLC} \frac{D_v \mu b}{kT} \left(\frac{\sigma}{\mu} \right)^n \tag{8}$$

where ($\dot{\varepsilon}_{PLC}$) is the steady state strain rate, A_{PLC} is a non-dimensional constant; D_v is the volume diffusivity at the test temperature; μ is the elastic shear modulus; k is the Boltzmann constant; T is the temperature in Kelvin; b is the Burgers vector; σ is the applied stress and n is the stress exponent.

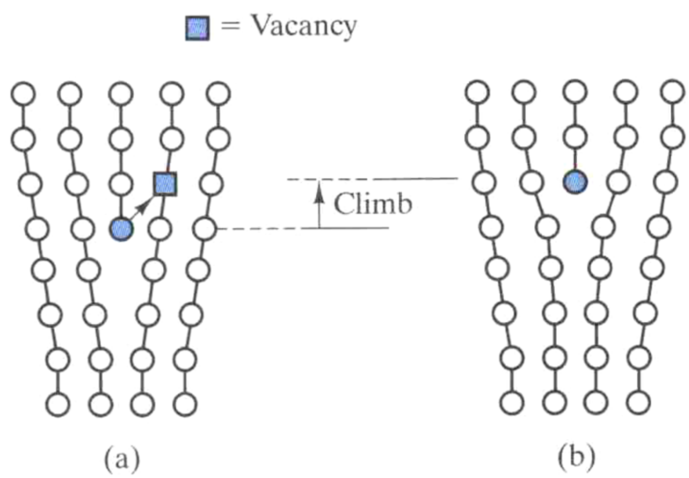

Figure 2.14: Mechanism of dislocation climb [18].

Diffusion creep: In diffusion creep (Nabarro-Herring creep and Coble creep), there is a stress assisted motion of vacancies causing the deformation of the material. The stress results in the flow of vacancies from the grain boundaries under normal tensile loading and the corresponding flow of atoms from the grain boundaries under normal compressive loading in the opposite direction. There is an evidence to suggest that the activation energy for diffusion creep and the activation energy for self-diffusion are identical [1,2,23].

Grain boundary sliding (GBS): Grain boundary sliding is a shear process in which the grains in polycrystalline metals move relative to each other parallel to grain boundaries.

The mechanism of grain boundary sliding can lead to the initiation of grain boundary fracture which occurs discontinuously with time. Figure 2.15 is a schematic illustration of cracking at triple points (intersection point of three grain boundaries) due to grain boundary sliding in which the arrows show the grain sliding direction [20,23,38].

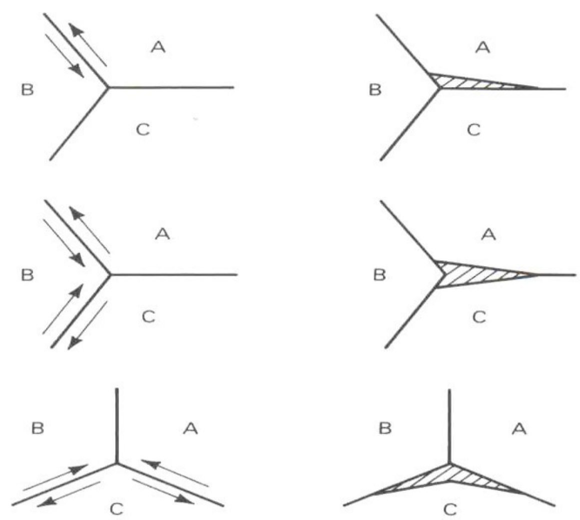

Figure 2.15: Schematic views of cracking due to grain boundary sliding [20,23,38].

The rate equation of GBS can be given as [41,42]:

$$\dot{\varepsilon}_{GBS} = A_{GBS}\frac{D_{gb}\mu b}{kT}\left(\frac{b}{d}\right)^q\left(\frac{\sigma}{\mu}\right)^n \tag{9}$$

where ($\dot{\varepsilon}_{GBS}$) is strain rate due to GBS; A_{GBS} is a non-dimensional constant; D_{gb} is the diffusion coefficient for grain boundary; q is the grain size index; d is the grain size; other parameters are the same as in equation (8).

2.3.2.3 Deformation mechanism map

J. Weertman and J. R. Weertman first constructed a creep diagram that displayed creep mechanisms (dominant flow processes) as discrete fields separated by transition boundaries where the two adjacent mechanisms contribute equally to overall deformation [43]. This concept was further developed by Ashby and co-workers to construct deformation and fracture mechanism maps for a material with a specific grain size as a function of homologous temperature (T/T_m) and normalized stress (τ/μ) where a particular thermally activated flow or fracture mechanism dominates the process of deformation and fracture within a given field [43,44]. The contours of constant strain rate were also superimposed on the various fields of the maps to relate applied stress, strain rate, and temperature to provide information about the range of dominance of each of these thermally activated processes and the rates of flow they produce [40]. Typical constitutive rate equations developed for simple metals and alloys were used to describe the contribution of different mechanisms in polycrystalline materials such as silver, nickel, iron, etc. involving dislocation glide, dislocation creep or power law creep (dislocation glide plus climb), and diffusion creep mechanisms, i.e. Nabarro-Herring creep and Coble creep [45]. Bell and Langdon carried out a detailed experimental study on the importance of GBS during creep in a magnesium alloy over a range of temperatures and stresses [46]. They also compared different methods of assessing the strain contribution due to GBS towards overall creep deformation and concluded that GBS had an important role to play in the deformation of metals that were subjected to creep at high temperatures. Langdon further developed a rate equation for GBS taking into account the movement of dislocations within, or adjacent to, the boundary plane, through a combination of dislocation glide and climb steps. He concluded that GBS was one of the dominant creep mechanisms that operates independently of diffusion creep leading to enhanced creep rates at low stresses [41]. Langdon and Mohamed used GBS rate equation to construct an alternative deformation mechanism map at fixed temperature but varying as a function of grain size and applied stress [47-50]. Bhargava et al. generated creep and tensile data for AlSI 304 stainless steel and generally found agreement of the plotted data with predictions in dislocation glide, power law creep, and diffusion creep regimes [44]. Luthy et al., on the other hand, showed that large portions of deformation regimes were dominated by GBS even in Ni and Al [51]. Janghorban and Esmaeili compared the deformation mechanism maps for Ti and Ti-6Al alloy and concluded that in the case of Ti-6Al alloy, power law creep dominates over a wider range of stresses and temperatures than for pure titanium, and the strengthening effect of aluminum shifted the iso-strain rate contours to higher stresses and temperatures [52]. Deformation mechanism maps for turbine blade superalloys such as IN738LC and GTD-111 have also been constructed and, in both cases, the authors assumed that diffusion creep was prevalent at lower stresses [53,54]. Koul and Castillo generated long term creep and rupture life data on cast IN738LC over a wide range of temperatures based on activation energy and detailed microstructural analyses. They concluded that GBS dominated the creep deformation in long term creep tests [55]. Using these data along with other data generated at a constant temperature where power law breakdown (PLB) was clearly discernible, they further modified the conventional deformation mechanism map by considering GBS as a separate deformation mechanism as shown in Figure 2.16 [56,57]. They further hypothesized that, at lower stresses and higher temperatures, the transition between GBS and diffusion creep may exist if an interface reaction controlled diffusion creep mechanism is considered dominant at very low stresses and high temperatures. The interface reaction controlled diffusion creep was considered because grain boundaries in complex engineering alloys are not perfect sources or sinks for vacancies due to the presence of grain boundary carbides and other segregating elements [58].

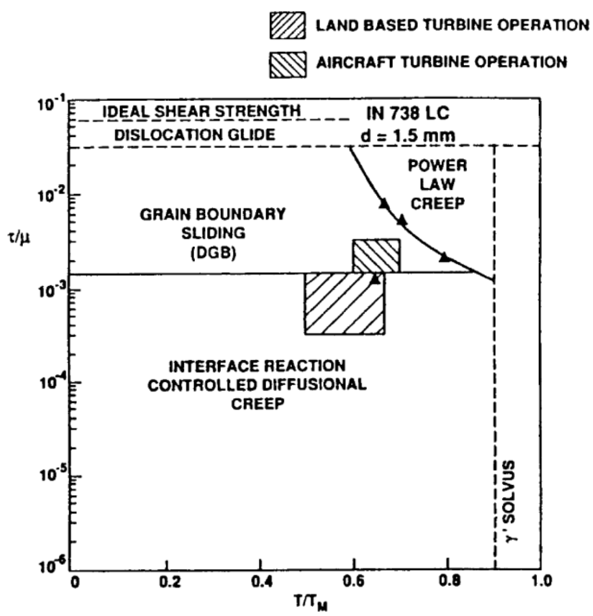

Figure 2.16: Deformation mechanism map for IN738LC blades indicating typical operational stress and temperature regimes for industrial and aero-engine blades [56,57].

Langdon further developed a rate equation for GBS applicable to a wide range of grain sizes, where the rate of sliding was considered to be controlled by the rate of accommodation through intra-granular slip. The model showed good agreement with experimental results under creep as well as superplastic deformation conditions [42]. Wu and Koul modified the Langdon's GBS model to develop a constitutive rate equation for GBS in the presence of grain boundary precipitates by incorporating physically defined back stresses opposing dislocation glide and climb [59]. They further concluded that the grain size dependence of the creep rate was grain boundary carbide distribution dependent in complex engineering alloys. They further refined their theoretical model to consider GBS at serrated grain boundaries, using the dynamics of grain boundary dislocation pile-ups, by averaging the sliding rate over the characteristic dimensions of grain boundary serrations [60]. Ayensu and Langdon established a clear inter-relationship between the extent and the rate of GBS and the development of creep cavitation. They concluded that the total cavitated area increased at faster sliding rates, but the number and density of cavities decreased at highest sliding rates because the cavities interlinked to form extended cracks along the boundaries. They confirmed that the overall level of cavitation is related to the occurrence of GBS [61]. Xu et al. developed an inter-granular GBS controlled creep crack growth model to describe the effects of microstructural features such as grain size, grain boundary precipitates, and serrated grain boundaries on the creep crack growth in complex engineering alloys [62]. They further showed experimentally that the grain size dependence of creep crack growth was grain boundary carbide distribution dependent in complex engineering alloys [63]. Wardsworth et al. have examined creep data of complex engineering alloys that include reactor-grade magnesium alloys, Ni based superalloys, and aluminum based alloys and postulated that creep deformation, in these alloys, was controlled by GBS accommodated by dislocation glide and climb process as opposed to Nebarro-Herring mechanism of diffusional creep at lower stresses [64]. It is thus evident that GBS as opposed to diffusion creep plays a major role in controlling the time dependent high temperature deformation in complex engineering alloys during creep, creep cavitation, crack nucleation, and growth processes. Wu et al. presented a schematic of a deformation mechanism map for complex engineering alloys where time dependent deformation at elevated temperatures is controlled either by dislocation glide and climb within the grain interiors called power law creep or along the grain boundaries called GBS, with the PLB marking the transition between two mechanisms (Figure 2.17) [65].

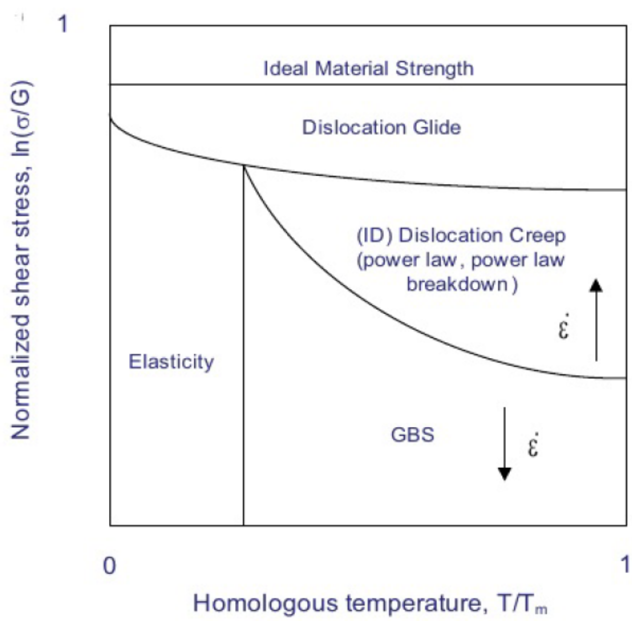

Figure 2.17: Schematic creep mechanisms [36,65].

Kawasaki et al. conducted experiments on Pb-62Sn eutectic alloy to plot the deformation mechanism map and showed that GBS was a dominant creep mechanism along with Nebarro-Herring and Coble creep [43]. Recently, Banerjee et al. modified the deformation mechanism map for the Pb-Sn eutectic solder alloy considering GBS as a dominant creep mechanism. Based on microstructural evidence, they further sub-divided the GBS dominant region into two parts based on the dominance of different GBS accommodation processes, i.e., GBS accommodated by wedge type cracking below $0.5T_m$ and GBS accommodated by cavitation creep above this temperature, Figure 2.18 [66]. Most recently, M. Asadi et al. used a similar approach considering that the PLB phenomenon was related to the dominance of GBS as opposed to diffusion creep and plotted a creep deformation mechanism map for the Alloy 718 [67]. They also summarized the rate equations for different creep mechanisms used for the construction of deformation mechanism maps for different engineering alloys [67].

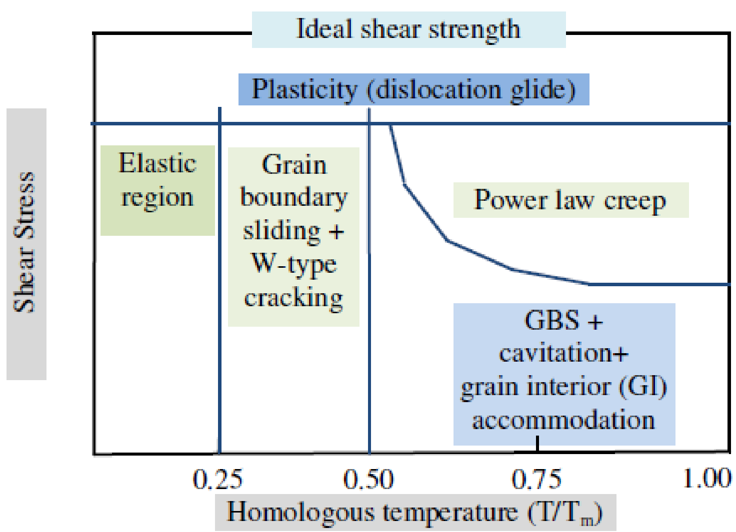

Figure 2.18: Modified deformation mechanism map by accommodating grain boundary sliding [66].

2.4 Artificial neural network

A number of adaptive numerical modeling (ANM) techniques such as artificial neural networks, support vector machines and Gaussian processes have been applied to a wide range of regression and classification problems in materials science [68]. In recent years, an artificial neural network (ANN) has been very successfully applied in many disciplines including pattern recognition, identification, classification, signal processing, process control, corrosion life prediction, and a host of other material science applications [69]. However, such modeling techniques also have some challenges in computational materials science. Raabe addressed some important challenges of computational materials science by giving examples of modeling and simulations of microstructure, computational bio-materials science, artificial neural network, etc. in his article. He also suggested that there should be a balance between the realm of simulations and experimental validation [70].

An artificial neural network, first presented in 1943 by the neurophysiologist Warren McCulloch and the logician Walter Pits, is a mathematical technique that models complex linear and non-linear relationships and simulates any correlations that are difficult to describe using physics based models. Today, the ANN can be trained to solve problems that are difficult for conventional computer programs or human intelligence. They are good at fitting functions and recognizing patterns. A fairly simple neural network can fit any practical function. The results computed by the neural network have reasonable accuracy and are much faster than other methods. The backpropagation neural network (BPNN) methods are the most commonly used ANN methods. Several different backpropagation training algorithms such as Gradient Descent, Gradient Descent with

Momentum, Scaled Conjugate Gradient or Resilient backpropagation, Levenberg-Marquadt and Bayesian Regularization, etc. have been applied either in batch mode or incremental mode of training on different pattern recognition and function approximation problems. Hagan and Mehnaz applied several backpropagation training algorithms on function approximation problems and concluded that the Levenberg-Marquadt method was more efficient than that of other techniques [71]. Demuth et al. have employed several BPNN algorithms and summarized that for function approximation problems, the Levenberg-Marquadt or Bayesian regularization performed better for small and medium size networks whereas for pattern recognition problems, the Resilient BPNN had the fastest algorithm. It has also been recommended that for large networks, Scaled Conjugate Gradient or Resilient backpropagation performed better. Gradient Descent and Gradient Descent with Momentum are generally too slow for many practical applications and are normally used only when incremental training is desired [69]. The basics of backpropagation algorithms are described in section 3.1.5.

The Levenberg-Marquadt and Bayesian Regularization are the most common backpropagation algorithms that have been successfully applied in recent decades to correlate chemical composition, heat treatment, and physical and mechanical properties with materials response to application conditions in the field of computational materials science. New alloys have also been designed for aero-engines and turbine components using an ANN. Another application of the BPNN so far has been the development of constitutive relationship for materials. A summary of previous research on backpropagation training algorithms, specifically, Levenberg-Marquadt and Bayesian Regularization methods is given in following paragraphs.

Huang and Blackwell successfully trained and tested a neural network model with mechanical property variables relating to temperature and strain rates to develop a constitutive relationship for the widely used Ni based superalloy Inconel 718. They gave the constitutive relationship and discussed its practical applications [72]. Bhadeshia summarized mechanical properties (strength, creep, and fatigue), heat treatment, phase transformation, welding, etc. in his review paper and explained how neural network models can be used to obtain optimum results in superalloys, polymers, ceramics, and composite materials [73].

Using the backpropagation neural network, microstructural and processing relationships in materials have been established in the past. Yoshitake et al. have constructed a neural network model to estimate the temperature dependent lattice constants of the γ and γ' phases of Ni based superalloys where the lattice parameters of two phases were expressed as a non-linear function of 18 variables including chemical composition and temperature based on data sets compiled from new experiments and published literature. The results showed that the method was extremely useful in understanding both the effect of solutes on the lattice mismatch, and on how this mismatch changes with temperature; the outcome was the development of new single-crystal alloys [74]. Sharpe considered four next-generations Ni based disc superalloys prepared by powder metallurgy and subjected to various controlled heat treatments. He established relationships between alloy processing and microstructure. Elevated temperature testing including tensile, hardness, creep deformation, creep crack growth, and fatigue crack growth tests were also conducted to establish relationships between microstructure and mechanical properties. He demonstrated the applicability of the ANN modeling to the development and behavior of Ni based disc superalloys [75]. Based on dislocation structures, a model has been developed to predict the flow stress of a precipitation hardening aluminum alloy. Three essential features of dislocation microstructures: substructure cell size, cell wall thickness, and density of geometrically necessary dislocations were used as input variables and the model was able to accurately predict the flow stress of aluminum alloy 6022 as a function of its dislocation density and structure [76].

The mechanical property determination is one of the main areas where an ANN has been recognized as a potentially useful modeling tool. The yield and ultimate tensile strength for a range of commercial, wrought, and polycrystalline Ni based superalloys has been modeled as a function of alloy chemistry and temperature. The trained models were subjected to a variety of metallurgical tests and the resultant models were found to be consistent with current metallurgical theory and experience [77,78]. Similarly, Warde and Knowles trained a series of networks to model the yield strength of polycrystalline superalloys as a function of temperature and composition. The previously developed neural network models were used in an alloy design process to highlight a subset of potential compositions from a wide range of alloys [79,80]. Haque and Sudhakar developed a BPNN model to predict the behavior of fracture toughness and tensile strength of micro-alloy steel as a function of microstructure with the objective to validate and extend the application of micro-alloy steels for a series of steels comprising dual-phase microstructures. They found that ANN training results were in good agreement with experimental results [81]. In addition, an ANN has also been utilized for the mechanical property determination in manufacturing processes. For example, Esfahani et al. modeled the effects of chemical composition and process parameters (total 23 variables) on the tensile strength of hot strip mill products and compared the results with experimental data [82]. Singh et al. trained an ANN model to predict the yield and tensile strengths of steel plates as a function of composition and rolling parameters and tested the model to confirm that the predictions were reasonable in the context of metallurgical principles and other data published in literature [83]. In the work of Bariani et al., a neural network was utilized to represent the rheological (flow stress) behaviour of a the Ni based superalloy, Nimonic 80A, under various values of strain rate and temperature conditions approximating thermo-mechanical cycles of industrial hot forging operations [84]. Martino et al. introduced neural network models to predict mechanical properties of Ni based alloys using 30 different input parameters including chemical composition (up to 20 elements), manufacturing process, crystallographic structure, heat treatment (with three temperature and time steps), and test conditions [85].

Hardness and some other physical properties along with mechanical properties were also successfully predicted using ANNs [86-88]. Hassan et al. recently applied a feedforward BPNN to predict the density, porosity, and hardness of aluminium-copper/silicon carbide composites using the weight percentage of copper and the volume fraction of reinforcement particles as input parameters [87]. Also, Syarif et al. developed a feedforward BPNN model for predicting the hardness, ultimate tensile strength, yield strength, and elongation of Ti-6Al-4V alloy as a function of heat treatment processes [88].

An ANN has been proven to be an effective tool in predicting creep properties and developing new alloys. Yoo et al. employed a neural network technique for modeling of the creep strength of polycrystalline Ni based superalloys used for turbine disc and blade applications as a function of alloy composition, creep stress, and creep temperature [89]. Furthermore, they investigated an ANN for an alloy development, i.e., the compositional modeling of the creep rupture life of single-crystal superalloys. The model contained test conditions such as creep stress and temperature as well as alloy compositions as inputs. As predicted by their model, newly designed alloys exhibited excellent phase stability and creep rupture lives that were better than or equivalent to those of CMSX-4 (second generation single-crystal Ni based superalloy) [90].

Numerous papers have been published on the use of ANN models for predicting fatigue life, fatigue/creep crack growth rate, and fatigue damage. Fuji. et al. used an ANN to model the fatigue crack growth rate of a large variety of Ni based superalloys as a function of some 51 variables, including stress intensity range ΔK, log ΔK, chemical composition, temperature, grain size, heat treatment, frequency, load waveform, atmosphere, R-ratio, distinction between short and long crack growth, sample thickness, and yield strength using data from published literature [91]. Schooling and Reed's research evaluated the use of an ANN to investigate and model trends in fatigue crack growth behaviour on stage II of the Paris regime, where the growth rate depends mainly on the stress intensity range, Young's modulus and yield strength of Ni based superalloys [92]. They also modeled the fatigue thresholds in Ni based superalloys and found that the models were in agreement with metallurgical knowledge and threshold values that were predicted with a reasonable degree of accuracy [93]. Lee et al. used constant stress fatigue data to evaluate possible ANN architectures for the prediction of fatigue lives and to develop network training methods for carbon-fibre-reinforced plastics and glassreinforced plastic laminate. They found that the ANN can also be used to model constant stress fatigue behaviour of composite materials [94]. Venkatesh and Rack performed comparative study of elevated temperature creep-fatigue life prediction by conducting high temperature low cycle fatigue tests on Ni based alloy Inconel 690 and developed a BPNN model with five extrinsic parameters, namely, strain range, tensile strain rate, compressive strain rate, tensile and compressive hold, and an intrinsic parameter (final grain size) and concluded that the ANN has the potential for achieving superior creep-fatigue life cycle predictions as compared to the modified Coffin-Manson, linear life fraction, and hysteresis energy methods [95]. Haque and Sudhakar build an ANN model to analyse fatigue crack growth rates as a function of stress intensity factor ranges for dual phase steel with different martensite content range. The model exhibited excellent agreement with experimental results [96]. Pleune et al. used Matlab NN software to train fatigue data to characterize the fatigue lives of carbon and low alloy steels as a function of environment, steel type, temperature, sulfur content, dissolved oxygen level in water, and tensile strain rate. The results were accurate and precise and agreed well with experimental data [97]. Srinivasan et al. generated data for solutionized stainless steel and applied an ANN model to study the LCF and creep-fatigue interaction behavior with five parameters, namely, temperature, strain rate, total strain amplitude, hold time, and PCW (percentage cold work) level. They showed that an ANN can predict creep-fatigue life much better than certain analytical approaches such as strain range partitioning, frequency modified approach, and energy based approach [98]. Genel employed an ANN model to predict the strain-fatigue life properties, i.e. fatigue strength coefficient and fatigue ductility coefficient values, which primarily characterize the curves of the strain amplitude vs. life reversals, of 73 steels using tensile material data that were extracted from literature. They constructed four separate ANN models for individual fatigue properties. The strain-fatigue life properties were predicted with high accuracy and seemed more reasonable compared to approximate methods that were formerly used based on tensile material data [99]. Kim et al. trained an ANN to recognize the stress intensity factor in the interval from micro-crack to fracture of structural steel specimens by using the acoustic emission (AE) measurements on compact tension specimens. Predictions obtained from the ANN were in good agreement with experimental data for the stress intensity factor. The ANN based on the AE measurement can be used to predict the stress intensity factor of different specimens for various cyclic loading conditions and can easily be incorporated to aid in the numerical analysis of the stress intensity factor during fatigue crack propagation [100]. Marquardt and Zenner trained an ANN to evaluate the components damage directly based on the S-N curve and load spectrum and approximated the lifetime that leads to a more reliable prediction than the fatigue life calculated by linear damage accumulation according to Palmgren and Miner. An ANN corresponds to a direct substitution of the Palmgren-Miner rule. It also demonstrates the ability to predict the lifetime for material groups and type of loadings for which the network was not trained [101]. A BPNN was employed for the fatigue life prediction under multiaxial random loading and for finding critical locations of an automotive sub-frame within reasonable time. The performance of an ANN model was evaluated by comparing its outputs with results of the conventional calculation method for multiaxial fatigue life and was found acceptable in most fatigue design considerations. It has been shown that an ANN provides good prediction results in searching critical component locations [102]. The neural computing method was also suitable for describing the fatigue data trends and statistical scatter of fatigue life under constant loading conditions for an arbitrary set of influential factors once the optimal neural network was designed and trained [103]. Bezazi et al. discussed the use of an ANN to estimate the fatigue lifetime of a sandwich composite material structure subjected to cyclic three-point bending loads. Excellent agreement was obtained between the model predicted outputs and experimental data [104]. An ANN was also trained to predict the fatigue crack growth rates of Ti-6Al-4V alloy using elevated temperature data at a given stress intensity under different temperatures [105].

An ANN has been proven to be a useful tool in simulation and condition monitoring of power plants. Fast et al. constructed the multi-layered feedforward network and accurately predicted operational and performance parameters of gas turbines for varying local ambient conditions [106].

Corrosion behaviour has also been predicted using ANNs. Cottis et al. built an ANN model to predict the pitting corrosion behaviour of a stainless steel as a function of solution composition and temperature [107].

Chapter 3

Modeling methodology and materials

3.1 Basics to neural network

The basic principles of simple neuron model, neural network architecture, transfer functions, backpropagation training methods, etc. are described in following sections.

3.1.1 Simple neuron model

An ANN has non-linear basic processing units called neurons. The neuron model and architecture of a neural network describe how a network transforms its inputs into outputs. The neural network architecture consists of multiple layers of neurons which have a summing up junction and a transfer function. A simple neuron model is shown in Figure 3.1. The neuron takes input p which is transmitted through a connection that multiplies its strength by the weight w to form the product wp. A bias b is also applied that is much like a weight except that it has a constant value of 1 and can be omitted if desired. The transfer function then takes the net input n which is the sum of the weighted inputs (wp + b) and produces the output Y [69,99]. The central idea of an ANN is to adjust weights and biases or the network itself adjusts these parameters to achieve accurate results [69].

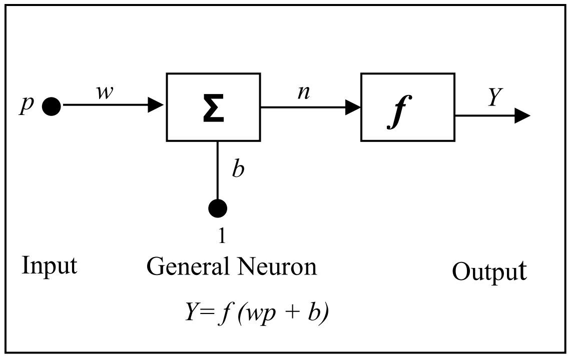

Figure 3.1: Simple neuron model [69].

3.1.2 Transfer functions

The transfer function takes the weighed input and produces the output Y. Sometimes the users can also specify their own transfer functions based on their requirement. The commonly used transfer functions are:

Linear transfer function: Neurons of this type are used as linear approximators. The linear transfer function is generally used in the output layer. A simple linear transfer function is shown in Figure 3.2 [69,105].

Sigmoid transfer function: The sigmoid transfer function is commonly used to develop non-linear relationships. The tan sigmoid transfer function, shown in Figure 3.3, takes the input, which can have any value between plus and minus infinity, and squeezes the output into the range -1 to 1. This transfer function is commonly used in backpropagation networks because it is differentiable and runs very fast [69,105].

The output of the neuron using the tan sigmoid transfer function is given by:

$$Y = \frac{2}{(1+\exp^{(-2*n)})^{-1}} \tag{10}$$

where Y is the output and n is the net input.

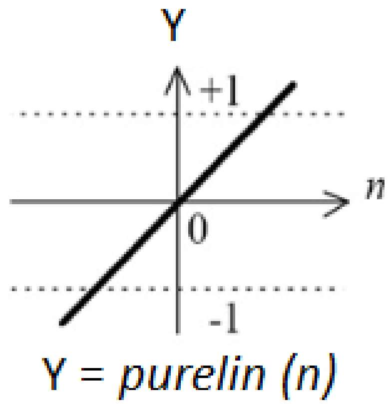

Figure 3.2: Linear transfer function [69,105].

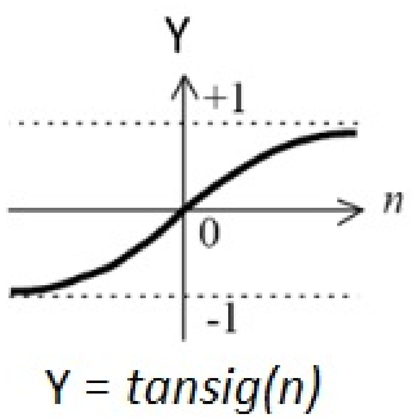

Figure 3.3: Tan sigmoid transfer function [69,105].

3.1.3 Neural network architecture

The most commonly used neural network architecture is given in Figure 3.4. It consists of one input layer, one output layer, and one hidden layer. The added hidden layer contains intermediary parameters that are automatically generated by the model; the hidden layer is necessary in case of complex non-linear relationships between the inputs and the outputs. One or multiple neurons connect the input to the hidden layer. Similarly, one or multiple neurons connect the hidden layer and the output layer. On the left hand side of Figure 3.4, p_1, p_2, ----p_n are the inputs that are sent to the hidden layer and on the right hand side Y is the output of the network [69,89,101].

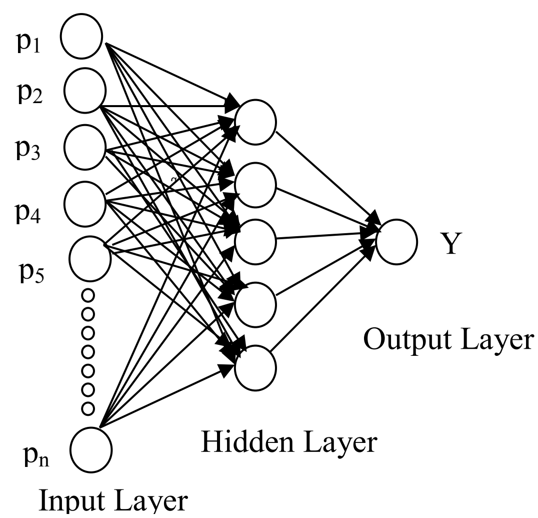

Figure 3.4: Neural network architecture used for modeling.

3.1.4 Backpropagation

The backpropagation generally has three or more layers: one input layer, one or more hidden layers, and one output layer. Each layer has a number of neurons that are connected with other neurons in neighbouring layers by weights. The backpropagation training set has a representative set of input/target pairs. It consists in moving the training patterns forward through the network layers. The output is computed by the network for each input in the training subset. The error between the computed output and the actual measurement value (target) is then propagated backward, and weights and biases are updated. These steps are repeated for all input/target pairs until the network performs optimally, i.e. the errors between the network outputs and the targets are minimal. The backpropagation method is illustrated in Figure 3.5 [69,105].

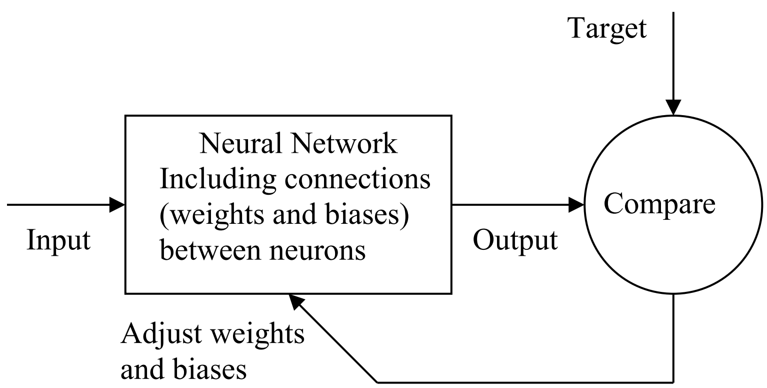

Figure 3.5: Backpropagation training [69,105].

3.1.5 Backpropagation training algorithms

Backpropagation updates the weights and biases in the direction in which the performance error function decreases most rapidly. An iteration of the backpropagation is given by:

$$X_{k+1} = X_k - a_k g_k \tag{11}$$

where X_k is a vector of current weights and biases, g_k is the current gradient, and α_k is the learning rate. As mentioned in section 2.4, there are several different backpropagation training algorithms, i.e. basic Gradient Descent, Gradient Descent with Momentum, Levenberg-Marquardt algorithm, etc. They all are based on other standard optimization techniques, such as conjugate gradient and Newton's methods. Their computation and storage requirements are different. The use of these algorithms depends on the type of problem to be solved. The conventional performance error function that is minimized by the backpropagation algorithm is defined as [69,82]:

$$mse = \frac{1}{N}\sum_{i=1}^{N}(e_i)^2 = \frac{1}{N}\sum_{i=1}^{N}(T_i - Y_i)^2 \qquad (12)$$

where mse is the mean squared error; T is the target and Y is the output. The default backpropagation training algorithm in Matlab neural network toolbox is the Levenberg-Marquardt algorithm (Trainlm). It is the most commonly used training method. It is a numerical optimization technique, a variation of the Newton's method, consisting in iteratively updating weights and biases to minimize the mean squared error, which is the performance error function of this algorithm. It uses the Jacobian matrix J that contains first derivatives of network errors with respect to weights and biases to compute the gradient. In Levenberg-Marquardt algorithm, the gradient can be computed as:

$$g_k = J^T e \qquad (13)$$

where g_k is the gradient; J is the Jacobian matrix; T is the transpose of the matrix and e is a vector of network errors. A new parameter, μ (mu), is introduced in this algorithm which is decreased or increased to reduce the performance error function during training of the network. According to equation (11), an iteration of the Levenberg-Marquardt algorithm can be written as:

$$X_{K+1} = X_k - [J^T J + \mu I]^{-1} J^T e \tag{14}$$

where I is the identity matrix.

The maximum value of mu is given by mu-max. The training status is displayed in every show. Training stops when some pre-defined conditions are met, i.e. the number of iterations exceeds the pre-defined maximum iterations or epochs, or the performance error function reaches the goal. Min-grad refers to the minimum gradient of the performance error function whereas max-fail is the maximum validation failure. The common training parameters for all algorithms in Matlab neural network toolbox are epochs, show, goal, min-grad, and max-fail [108]. The training parameters for the Levenberg-Marquadt algorithm are epochs, show, goal, mu, mu-dec, mu-inc, mu-max, min-grad, etc. The Levenberg-Marquadt backpropagation algorithm is the fastest training algorithm available, but, it also requires a lot of computer memory when the training set is large. Therefore, the parameter mem-reduc is used for the reduction of computing memory requirement [69].

3.1.6 Feedforward backpropagation network

Multilayer feedforward network is the most common architecture used by the backpropagation algorithm. Generally, four parameters are required to create a network object in Matlab neural network toolbox [108]. These parameters are the minimum and maximum values of inputs, the number of neurons of each layer, the transfer functions to be used in each layer, and the training function. These four input parameters are briefly described in the following paragraphs.

Inputs: The selection of inputs is very important for optimal network development. Their maximum and minimum values form the basic values of feedforward network in Matlab neural network toolbox during training of the network [69,108].

Number of neurons: The number of neurons forms the second parameter of the feedforward neural network. As already mentioned earlier, the neural network architecture consists of multiple layers of neurons. The number of neurons in the input layer is determined by the number of input variables. The number of neurons in the hidden layer is determined by trial and error with various weights and biases, whereas the number of targets is considered to be the number of neurons in the output layer. Generally, under-fitting occurs if the hidden neurons are too few and too many neurons cause over-fitting and strong oscillations [69,108].

Transfer functions: Various transfer functions are available in the Matlab neural network toolbox such as tan sigmoid, log sigmoid, and linear transfer function. Tan sigmoid and linear transfer functions are commonly used in the hidden and output layers respectively (see section 3.1.2).

Training functions: Once the first three input parameters of the feedforward network are set and the network is initialized by weights and biases, the network is ready for training. During training, the performance error function, defined by the training algorithm or by the user, is minimized by iteratively adjusting weights and biases of the network [69,108]. Various training algorithms used in feedforward neural network are explained in 3.1.5.

3.1.7 Improving generalization

Generally, over-fitting can occur during the neural network training. This means that the error in the training subset can be small, though the error for any new set of data can still be large because the network has just memorized the training example, but does not have the ability to generalize to new situations. Various solutions may be used to improve the network generalization. One method is to use a network that is just large enough to provide an adequate fit. The larger the network, the more complex functions the network can create and higher the risk of over-fitting. But, it is difficult to know beforehand how large a network should be for a specific application. If the number of parameters in the network is much smaller than the total number of data points in the training set, then there is little or no chance of over-fitting. If data are limited, two generalization techniques, early stopping and regularization can prevent over-fitting [69].

3.1.7.1 Early stopping

An early stopping is the default method in Matlab neural network toolbox for improving generalization. In this method, the data is divided into three subsets: a training subset, a validation subset, and a test subset. The training subset is used for computing the network errors and updating the network weights and biases. During the initial phase of training, the error on the validation subset and training subset normally decreases. But, the error on the validation subset typically begins to rise, when over-fitting occurs. When the validation error continues to increase for a specified number of iterations, the training stops, and weights and biases at the minimum of the validation error are returned. The testing subset is not utilized during training and used for comparing different models, which allow assessing the generalization error and confirming the appropriateness of the data division into three subsets [69].

3.1.7.2 Regularization

The regularization approach is the most commonly used method for preventing over-fitting, wherein the performance error function is optimized. The Bayesian Regularization (Trainbr) is a type of the regularization method in which the Trainbr training function is used to automatically set the optimal performance error function to achieve the best possible generalization. The Bayesian Regularization uses the sum of squared error as the performance error function. The sum of squared error is automatically optimized to achieve the best regularization by minimizing and modifying a linear combination of squared errors and weights. In addition to a term of mean square error, the Bayesian Regularization includes a term of mean square weight. Therefore, the performance error function for the Bayesian Regularization (msereg) method can be given by [69,82]:

$$msereg = \gamma mse + (1-\gamma)msw \tag{15}$$

where msw (mean square weight) is defined as:

$$msw = \frac{1}{n}\sum_{j=1}^{n} w_j^2 \tag{16}$$

w_j is the weight, and γ is the performance ratio, which is adjusted automatically by the Bayesian Regularization algorithm. This performance error function (msereg) leads to smaller network weights and biases, which make the network response smoother and less likely to over-fit.

The common training parameters in Trainbr are almost the same as for Trainlm, i.e. epochs, goal, show, time, min-grad, max-fail, mem-reduc, mu, mu-dec, mu-inc, and mu-max. In training with Trainbr, the algorithm runs until the effective number of parameters reaches convergence. Generally, the training stops with the message "Maximum mu reached" which indicates that the algorithm has converged. In some cases, the algorithm is also considered to have converged if the sum of squared error and sum of squared weights remain constant over several interactions. In most cases, the Bayesian Regularization provides better generalization performance than other methods particularly when the data set size is very limited and the statistical scatter is small. However, it takes more time to converge than the other methods [69].

3.1.8 Pre-processing and post-processing

The neural network training is more efficient when both input and target variables are pre-processed or normalized (scaled) so that they always fall within a specified range. When the network is been created, some of the pre-processing functions are automatically performed [69].

3.1.8.1 Pre-processing

There are two main normalizing functions, namely, Min and Max; and Mean and Standard deviation which are explained below.

Min and Max: The Min and Max function in Matlab neural network toolbox is used to pre-process the inputs (p) and targets (T) into normalized inputs (p_n) and targets (T_n) that fall within the interval [-1, 1].

Mean and Standard deviation: This normalizes inputs (p) and targets (T) into normalized inputs (p_n) and targets (T_n) with a mean value of zero (0) and a standard deviation of one (1).

3.1.8.2 Post-processing

The performance of a trained network can be initially assessed based on the errors on training, validation, and test subsets. However, the ultimate accuracy of the network is usually evaluated using a linear regression analysis between the network outputs and the corresponding targets for the entire data set including training, validation, and test subsets. The linear regression analysis returns three parameters: the slope m of the regression line, its y-intercept b, and the correlation coefficient R between the outputs and targets. The first two parameters m and b relate targets to network outputs and the third parameter R is a measure of how well the variation in outputs is explained by the targets. For a perfect fit, m (slope) should be 1, b (y-intercept) should be 0, and R (correlation coefficient) should be 1 [69].

All models are performed using Microsoft Windows 7 Home edition with AMD Atholon (tm) II X2 220 Processor and 3GB RAM as the operating system and run into Matlab (R2007b) neural network toolbox.

3.2 Materials data

A total of 22 γ’ precipitated Ni based superalloys and 1 Cr-Mo-V steel material, all used in turbine blades and disc, are selected for this study. Chemical compositions are provided in Table 3.1 [11,109-112].

Table 3.1: Chemical compositions (wt %) of materials used for modeling [11,109-112].

Material	Ni	Cr	Co	Mo	W	Ta	Nb	Al	Ti	Zr	B	C	Si	V	Fe	Reference
Nimonic PE 16, W	43	16.7	0.19	3.27	0	0	0	1.1	1.28	0	0	0.065	0.24	0	34.155	110
Nimonic PE 16, G	43.2	16.2	0.05	3.5	0	0	0	1.25	1.28	0	0	0.054	0.06	0	35.61	110
Nimonic 80A	76.04	19.4	0.1	0	0	0	0	1.53	2.47	0	0	0.07	0.2	0	0.19	110
Nimonic 90 (1)	59.27	19.5	16	0.3	0	0	0	1.8	2	0	0	0.13	1	0	0	110
Nimonic 105	53.88	15	20	5	0	0	0	5	1	0	0	0.12	0	0	0	110
IN100 (1)	50.28	10	15.5	0	0	0	0	4.75	5.1	0	0	0	0	0	0	110
IN738LC	61.48	16	8.5	1.75	2.6	1.75	0.85	3.45	3.45	0.06	0.0095	0.11	0	0	0	11,109, 111
Nimonic 90 (2)	55.5	19.5	18	0	0	0	0	1.4	2.4	0	0	0.06	0	0	0	11,109,111
X-750	73	15.5	0	0	0	0	1	0.7	2.5	0	0	0.04	0	0	0	11,109,111
Astroloy (1)	56.5	15	15	5.25	0	0	0	4.4	3.5	0.06	0.03	0.06	0	0	0	11,109, 111
IN100 (2)	60	10	15	3	0	0	0	5.5	4.7	0.06	0.02	0.15	0	0	0	11,109,111
Mar-M-246	60	9	10	2.5	10	1.5	0	5.5	1.5	0.05	0.02	0.15	0	0	0	11,109,111
Udimet 500	48	19	19	4	0	0	0	3	3	0	0.01	0.08	0	0	0	11,109, 111
Waspaloy (1)	57	19.5	13.5	4.3	0	0	0	1.4	3	0.09	0.01	0.07	0	0	0	11,109,111
IN713LC	75	12	0	4.5	0	0	0	6	0.6	0.1	0	0.05	0	0	0	11,109,111
Nimonic 115	55	15	15	4	0	0	0	5	4	0.04	0	0.2	0	0	0	11,109,111
IN100 (3)	56.91	12	18.4	3.1	0	0	0	5	4.5	0	0	0.09	0	0	0	112
Waspaloy (2)	57.96	19.3	13.6	4.2	0	0	0	1.3	3.6	0	0	0.04	0	0	0	112
Rene 95	69.22	12.8	8.1	3.6	0	0	0	3.6	2.6	0	0	0.08	0	0	0	112
MERL 76	56.98	12	18.4	3.3	0	0	0	5.1	4.2	0	0	0.023	0	0	0	112
Astroloy (2)	55.38	14.7	17.2	5	0	0	0	4.1	3.6	0	0	0.024	0	0	0	112
HIP Astroloy	54.84	15.1	17	5.2	0	0	0	4	3.5	0	0	0.023	0	0	0	112
Cr-Mo-V Steel	0.35	1.23	0	1.2	0	0	0	0.005	0	0	0	0.3	0.25	0.26	95.45	17

G and W represent to Glossop Superalloys Ltd and Wiggins Ltd respectively, which refer to the name of supplier companies.

For any modeling using neural networks, the selection of neural network methods, input variables, and the number of data points is important. Different materials are used for γ' precipitate size, thermal expansion coefficient, fatigue life, hysteresis energy, accumulated fatigue damage, and deformation mechanism maps because no material could be found for which appropriate literature data are available to cover all material properties modeled in this study. Specific materials and rationales for their selection are provided in the following paragraphs for each property considered.

1) γ' precipitate size

The materials selected for γ' precipitate size are six γ' precipitated Ni based superalloys that are used for turbine discs and blades including Nimonic PE 16 (W), Nimonic PE 16 (G), Nimonic 80A, Nimonic 90, Nimonic 105, and IN100 for which required literature input data is available. The chemical composition of these materials is given in Table 3.1 [110]. 13 input variables including solutionizing temperature, solutionizing time, ageing temperature, ageing time, and chemical composition (Ni, Cr, Al, Ti, Co, C, Mo, Si, Fe) are chosen. In order to form efficient relationships between input and output variables, large amounts of data are required for each input/target pair.

In addition, the effects of ageing methods on the γ' precipitate size is modeled on commonly used Ni based superalloy (IN738LC) in turbine blades with sufficient literature data for appropriate neural network simulations.

2) Thermal expansion coefficient

Ten γ' precipitated Ni based superalloys used in turbine discs and blades are selected for which sufficient literature data are found for modeling of the thermal expansion coefficient. They include IN738LC, Nimonic 90, X-750, Astroloy, IN100, Mar-M-246, Udimet 500, Waspaloy, IN713LC, and Nimonic 115. Their chemical compositions are given in Table 3.1 [11,109,111]. 22 input variables including temperature, chemical composition (Ni, Cr, Co, Mo, W, Ta, Nb, Al, Ti, B, Zr, C contents), solution heat treatment (solution temperature, solution time, chilled water quenching, air cooling), and ageing heat treatment (ageing temperature, ageing time, water cooling, air cooling) are chosen.

3) Fatigue life

Six γ' precipitated turbine disc Ni based superalloys, namely, IN100, Waspaloy, Rene 95, Merl 76, Astroloy, and HIP Astroloy, available appropriate literature data for fatigue life, are used for simulation using neural networks. Their chemical compositions can be seen in Table 3.1 [112]. 15 input variables such as fatigue parameters (plastic strain range, strain ratio, and stress range), mechanical properties (ultimate strength, yield strength, and reduction in area), chemical composition (Ni, Cr, Co, Mo, Al, Ti, and C), and microstructural properties (grain size and volume fraction of γ' precipitates) are chosen.

4) Hysteresis energy

The materials selected for modeling of the hysteresis energy are same used for the fatigue life modeling, namely IN100, Waspaloy, Rene 95, Merl 76, Astroloy, and HIP Astroloy, for the reasons described above. The chemical composition of these materials is given in Table 3.1 [112].

5) Accumulated fatigue damage

The simulation of the accumulated fatigue damage is a hybrid of models for the fatigue life and hysteresis energy. Therefore, same materials described in 3) and 4) are used.

6) Deformation mechanism map

Cr-Mo-V steel has sufficient literature data for the simulation of deformation mechanism map construction. It is a carbide precipitation strengthened and largely used in turbine disc, and therefore, it is judged appropriate, together with γ' precipitated Ni based superalloys, for the objective of this thesis which is to investigate turbine discs and blade materials. Carbide precipitates in Cr-Mo-V steel are located both in grain interior and at grain boundaries that are primarily responsible for the material's strength at high temperature similar to γ' precipitates in Ni based superalloys. The chemical composition of Cr-Mo-V steel is given in Table 3.1 [17].

3.3 Other methods

Apart from the neural network modeling, other modeling methods are also used in this work as presented in the following sections.

3.3.1 Fracture mechanics approach for fatigue life prediction

Fracture mechanics principles are first used to determine the critical crack lengths of Ni based superalloys for the different load levels and then used to estimate corresponding fatigue lives.

3.3.1.1 Critical crack size determination

Using fracture mechanics, the critical crack length (c_f) can be estimated using the following equation [2] (see section 2.3.1.3):

$$K_{IC} = Y\sigma_c\sqrt{\pi c_f} \qquad \text{or} \qquad c_f = \frac{1}{\pi}\left(\frac{K_{IC}}{\sigma_c Y}\right)^2 \tag{17}$$

where K_{IC} is the fracture toughness; Y is a function depending on the geometry and loading conditions; σ_c is the critical stress or the maximum stress (σ_{max}) that can be defined as the sum of stress amplitude (σ_a) and mean stress (σ_m) given by equation (18):

$$\sigma_c = \sigma_a + \sigma_m \tag{18}$$

whereas the alternating stress or stress amplitude (σ_a) can be determined by using the following equation:

$$\sigma_a = \frac{\Delta\sigma}{2} = \frac{\sigma_{\max} - \sigma_{\min}}{2} \tag{19}$$

where $\Delta\sigma$ is the stress range; σ_{max} and σ_{min} are the maximum and minimum stresses respectively.

3.3.1.2 Crack propagation life determination

The crack propagation life can be predicted by solving the Paris equation (6) as given by [1] (see section 2.3.1.3):

$$N = \frac{1}{\frac{(m-2)}{2}\pi^{m/2} A Y^m (\Delta\sigma)^m c_0^{(m-2)/2}}\left[1-\left(\frac{c_0}{c_f}\right)^{(m-2)/2}\right] \tag{6}$$

3.3.2 Area method for calculation of the hysteresis energy

The hysteresis loop area equation (1), the most commonly used method for estimating the hysteresis energy, can be given as [24]:

$$\Delta W = \frac{\Delta\sigma\Delta\varepsilon_p}{1+n'} \tag{1}$$

where ΔW is the hysteresis energy; $\Delta\sigma$ is the stress range; $\Delta\varepsilon_p$ is the plastic strain and n' is the cyclic strain hardening exponent.

3.3.3 Fatigue damage prediction

Knowing both the hysteresis energy (ΔW) and the number of cycles to failure (N_F) allows assessing the approximate accumulated fatigue energy or damage (D_F) of components according to equation (20) [113]:

$$D_F = \Delta W . N_F \tag{20}$$

3.3.4 Rate equations for the deformation mechanism map

For constructing the deformation mechanism map of 1.23Cr-1.2Mo-0.26V steel, the following rate equations for obstacle controlled dislocation glide [40,114], modified rate equations for grain boundary sliding [56,59], and power law creep [56] are used respectively:

$$\dot{\gamma}_{DG} = \dot{\gamma}_0 \exp\left[-\frac{\Delta F}{kT}\left(1-\frac{\tau_s}{\tau_0}\right)\right] \tag{21}$$

$$\dot{\gamma}_{GBS} = A_{GBS}\frac{D_{gb}\mu b}{kT}\left(\frac{b}{d}\right)^q\left(\frac{\lambda+r}{b}\right)^{q-1}\frac{(\tau_s-\tau_{ig})(\tau_s-\tau_{ic})}{\mu^2} \tag{22}$$

$$\dot{\varepsilon}_{PLC} = A_{PLC}\frac{D_v\mu b}{kT}\left(\frac{\sigma-\sigma_b}{\mu}\right)^n \tag{23}$$

Where $\dot{\gamma}_{DG}$ is the strain rate due to dislocation glide; $\dot{\gamma}_0$ is a pre-exponential constant; ΔF is the activation energy for dislocation glide required to overcome the obstacles without any aid from external stresses; τ_s is the applied shear stress; τ_o is the flow strength of the solid at zero K; τ_{ig} and τ_{ic} are the back stresses due to dislocation glide and climb respectively; λ is the grain boundary precipitate spacing; r is the average radius of grain boundary particles; τ_b is the back stress due to carbides; other parameters are the same as in equations (8) and (9).

Chapter 4

Results and discussion

Turbine components and aerospace engines operate at high temperatures and under severe thermo-mechanical loading conditions which can result in the failure of engines. Operating temperature, microstructure, and properties (mechanical, thermal, etc.) are fundamental parameters in the design and assessment of aerospace components. The development of relationships between these parameters and failure modes is very important in order to predict the lives of turbine components. Therefore, separate neural network models have been developed for predicting γ' precipitate size, thermal expansion coefficient, fatigue life, and hysteresis energy which are used to determine the accumulated fatigue damage of turbine blade and disc materials. Moreover, creep deformation mechanism map for 1.23Cr-1.2Mo-0.26V steel is also constructed using dislocation glide, grain boundary sliding, and power law creep rate equations and verified with experimental data and neural network results. Together with fatigue and environmental damage such as wear and corrosion, creep can be used to predict the accumulated fatigue damage of turbine blade and disc materials.

As mentioned in section 3.1.5, in all neural network models, either feedforward Levenberg-Marquadt or Bayesian Regularization backpropagation in batch mode of training is selected in the Matlab neural network toolbox to iteratively update the weights and biases to minimize the error. Both the input and target data are normalized so that the inputs and targets have zero mean and unity standard deviation before training to get efficient results. As explained earlier, to avoid over-fitting, inputs and targets are randomly divided into three subsets, i.e. training, validation, and testing subsets. The training status is displayed in every show. To avoid premature convergence, the training parameters are set so that the convergence is sufficiently smooth and slow. Training stops when some predefined conditions are met, i.e. mu becomes larger than mu-max, the number of iterations reaches the predefined maximum number of epochs, the performance error function reaches the goal, etc. [69]. The obtained neural network training and results are described in the following sections.

4.1 Gamma prime (γ') precipitate size

Chemical composition and heat treatment influence the size and shape of γ' precipitates, which, in turn, play an important role in high temperature properties of superalloys. A neural network has been employed to determine alloy processing and microstructure relationship for superalloys [75] and to estimate the temperature dependent lattice constants of γ and γ' phases of Ni based superalloys as a function of chemical composition and temperature [74]. However, neural network models to predict γ' precipitate size of Ni based superalloys are still lacking. Therefore, a neural network model is developed in this work to correlate chemical composition and heat treatment with the γ' precipitates size of Ni based superalloys as described below.

4.1.1 Training methods for modeling of the γ' precipitate size

It is very difficult to know which neural network training algorithm is best suitable for a given problem as each training algorithm depends on many factors such as the complexity of the problem, the number of data points in the training set, the number of weights and biases in the network, the error goal, and the type of function to be approximated. Therefore, the Levenberg-Marquadt (Trainlm) and Bayesian Regularization (Trainbr) methods, explained in sections 3.1.5 and 3.1.7.2, are investigated in order to determine the most appropriate of these two training methods for the γ' precipitate size modeling of Ni based superalloys. The required data used for this study are taken from published literature [110]. Materials considered are Nimonic PE 16, Nimonic 80A, Nimonic 90, Nimonic 105, and IN100. The inputs variables are solutionizing temperature, solutionizing time, ageing temperature, ageing time, and chemical composition including Ni, Cr, Al, Ti, Co, C, Mo, Si, and Fe contents (see Tables 3.1, 4.1 and A1) [110]. The γ' precipitate size for each corresponding input set is taken as the target. For 13 input variables, a total of 200 data points is used for modeling the γ' precipitate size. In order to avoid over-fitting, the total data set is randomly divided into three subsets; a training subset (50% of the total data set), a validation subset (25% of the total data set), and a test subset (25% of the total data set).

The performance error function for the Levenberg-Marquadt training algorithm (Trainlm) is the mean squared error whereas for the Bayesian Regularization training algorithm (Trainbr), the performance error function is the sum of squared error. In order to obtain optimal performance, for both algorithms, mu is set to 1, which is a relatively large value, and mu-dec and mu-inc are set to 0.4 and 1.5, respectively.

The final network architecture consists of three layer feedforward backpropagation neural network in both training methods. For both methods, the network is trained until the minimum squared error (mean squared error or sum of squared error) is achieved.

Table 4.1: Inputs, targets and their ranges for modeling of the γ' precipitate size [110]

Nr.	Input parameters	Ranges
1	Nickel content (wt %)	43-76.04
2	Chromium content (wt %)	10-19.5
3	Aluminum content (wt %)	1.1-5
4	Titanium content (wt %)	1-5.1
5	Cobalt content (wt %)	0.05-20
6	Carbon content (wt %)	0-0.13
7	Molybdenum content (wt %)	0-5
8	Silicon content (wt %)	0-1
9	Iron content (wt %)	0-35.61
10	Solutionizing temperature (^{o}C)	1000-1200
11	Solutionizing time (hr)	2-20
12	Ageing temperature (^{o}C)	670-1000
13	Ageing time (hr)	0.16-3360
1	Target , T (γ' size, nm)	2.5-873

In order to determine the optimum structure for both Trainlm and Trainbr methods, the rate of error convergence is evaluated by changing the number of hidden neurons from 7 to 51. For each number of hidden neurons, the training is run for approximately 1000 epochs and took approximately 1 minute for the Trainlm method and 2 to 3 minutes for the Trainbr method. After trial and error, the optimal architecture for the Trainlm method is 13-13-1 obtained in only 36 epochs, whereas the optimal architecture for the Trainbr method is 13-17-1 after 158 epochs. The entire process took approximately one hour for the Trainlm method and 2-3 hours for the Trainbr method.

Figure 4.1 shows the mean squared error vs. the number of epochs for training, validation and testing subsets for the Trainlm method. Initially, the mean squared error for all training, validation and testing subsets decreases and then becomes constant and the training stops at 36 epochs. It can be seen from Figure 4.1 that the testing curve also follows the same pattern, which indicates that the network architectures converge and stabilize well. All three curves follow the same pattern indicating that no over-fitting occurred and the network is properly trained.

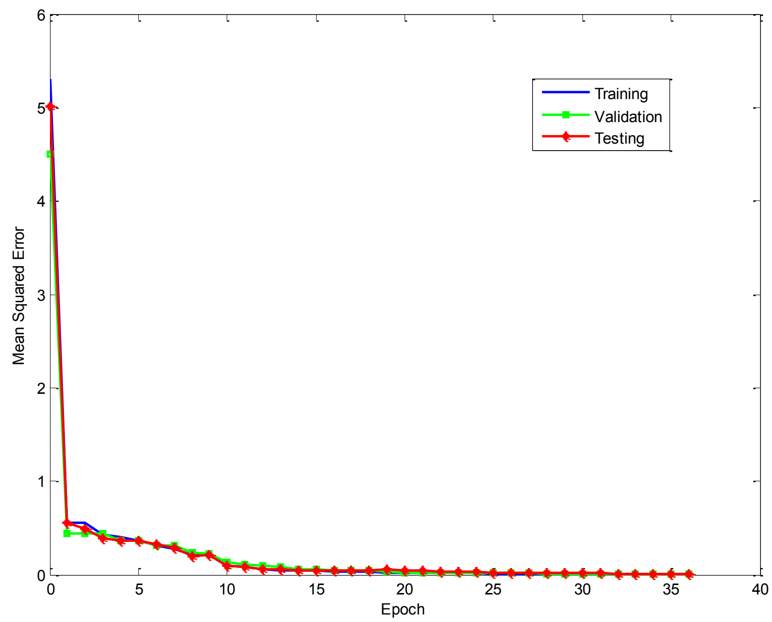

Figure 4.1: Mean squared error vs. epoch for the Trainlm method.

Similarly, Figure 4.2 shows the response of the network throughout its development using the Trainbr method. The uppermost plot in Figure 4.2 shows that the sum of squared error for the training subset drops rapidly as the network is trained. The final values of the sum of squared errors at 158 epochs are indicated in Figure 4.2. Moreover, when validation and testing subsets are used, the sum of squared errors vs. the number of training epochs follows a similar trend as that of the training subset. This indicates that no over-fitting occurred and the network is properly trained. The middle plot of Figure 4.2 shows that the squared weight at 158 epochs is 181.811. The bottom plot in Figure 4.2 shows that the effective number of parameters has reached a steady state of 49.6989 beyond 158 epochs, another indication that the network size is appropriate and the network is well trained.

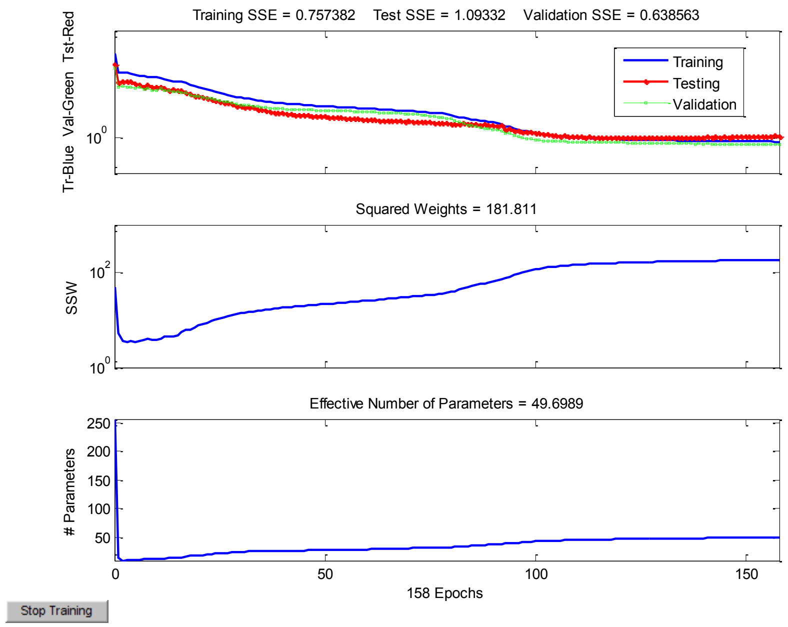

Figure 4.2: Network response during training for the Trainbr method.

The linear regression analysis is also performed for the γ' precipitates size modeling that yields a slope m = 0.99; a y-axis intercept b = 1.5 and a correlation coefficient R = 0.99542 for the Trainlm method and m = 0.98; b = 2.9 and R = 0.9939 for the Trainbr method. For both models, these parameters are very close to being ideal (m = 1; b = 0; R = 1) and indicate a good fit. The best linear regression fits are shown in Figures 4.3 and 4.4 by solid lines for both Trainlm and Trainbr methods respectively.

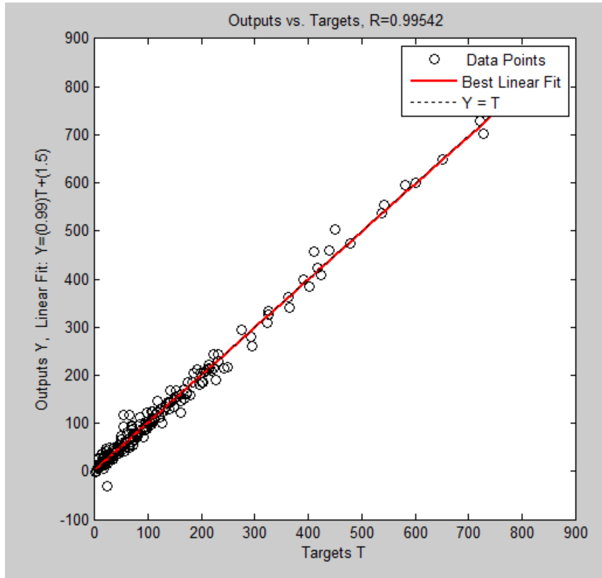

Figure 4.3: Linear regression analysis of the neural network obtained by Trainlm.

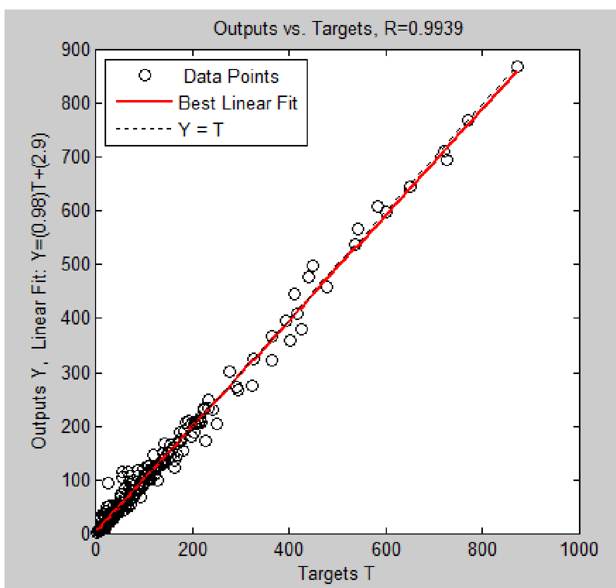

Figure 4.4: Linear regression analysis of the neural network obtained by Trainbr.

The theoretical one-to-one correspondence lines between the network outputs and targets are shown as dashed lines. Both the solid line and the dashed line practically overlap which indicate the high accuracy of the model and also show that the neural network is successful in learning the relationship between the input and the output variables. Targets and modeling results of the testing data subset obtained from the Trainlm and Trainbr methods as well as their corresponding % errors are summarized in Table 4.2.

Table 4.2: Gamma prime (γ') precipitate size obtained from Trainlm and Trainbr training methods from the testing data subset and corresponding errors

Nr.	Target, T	Trainlm output, Y_1,	T-Y_1	Trainlm % Error, E_1	Trainbr output, Y_2,	T-Y_2	Trainbr % Error, E_2
1	4.3	0.05	4.25	98.79	2.96	1.34	31.18
2	10.5	14.92	-4.42	42.14	12.37	-1.87	17.84
3	23.5	15.09	8.41	35.80	93.37	-69.87	297.33
4	12.25	10.85	1.40	11.40	9.02	3.23	26.40
5	20.3	22.25	-1.95	9.60	20.90	-0.60	2.97
6	32.2	35.85	-3.65	11.33	37.55	-5.35	16.62
7	54.1	46.98	7.12	13.16	51.85	2.25	4.16
8	48	43.69	4.31	8.99	43.54	4.46	9.29
9	138	144.23	-6.23	4.51	135.16	2.84	2.06
10	10	10.56	-0.56	5.56	11.82	-1.82	18.15
11	23	14.08	8.92	38.77	14.90	8.10	35.24
12	48.7	47.55	1.15	2.35	46.65	2.05	4.21
13	98.7	87.32	11.38	11.53	90.80	7.90	8.00
14	108	108.59	-0.59	0.55	111.84	-3.84	3.55
15	142.6	144.63	-2.03	1.42	137.45	5.15	3.61
16	192.7	211.45	-18.75	9.73	208.39	-15.69	8.14
17	35	31.30	3.70	10.58	28.30	6.70	19.15
18	110	103.12	6.88	6.25	101.30	8.70	7.91
19	155	155.10	-0.10	0.07	153.98	1.02	0.66
20	202	184.06	17.94	8.88	187.61	14.39	7.12
21	294	261.59	32.41	11.02	267.77	26.23	8.92
22	30.6	32.09	-1.49	4.88	34.07	-3.47	11.33
23	63	67.25	-4.25	6.75	66.54	-3.54	5.62
24	118	123.44	-5.44	4.61	120.59	-2.59	2.19
25	223	214.24	8.76	3.93	230.84	-7.84	3.52
26	19	13.63	5.37	28.27	14.12	4.88	25.71
27	17	19.08	-2.08	12.26	17.85	-0.85	5.03
28	42	42.18	-0.18	0.42	39.88	2.12	5.06

29	61	81.91	-20.91	34.28	81.59	-20.59	33.76
30	161	122.49	38.51	23.92	123.40	37.60	23.35
31	219	209.48	9.52	4.35	206.06	12.94	5.91
32	8.8	28.50	-19.70	223.85	31.34	-22.54	256.19
33	57	41.73	15.27	26.79	42.57	14.43	25.31
34	275	295.33	-20.33	7.39	300.10	-25.10	9.13
35	13.6	35.92	-22.32	164.13	35.87	-22.27	163.77
36	47.8	47.00	0.80	1.67	45.32	2.48	5.20
37	149	134.54	14.46	9.70	135.38	13.62	9.14
38	55	116.47	-61.47	111.77	113.62	-58.62	106.59
39	227	190.32	36.68	16.16	171.29	55.71	24.54
40	450	503.80	-53.80	11.96	499.38	-49.38	10.97
41	20	13.46	6.54	32.72	12.79	7.21	36.04
42	50	65.46	-15.46	30.91	66.40	-16.40	32.81
43	139	144.66	-5.66	4.08	147.43	-8.43	6.06
44	38	48.68	-10.68	28.11	50.94	-12.94	34.05
45	81	75.65	5.35	6.60	75.14	5.86	7.23
46	232	242.94	-10.94	4.72	249.25	-17.25	7.43
47	439	460.63	-21.63	4.93	476.64	-37.64	8.58
48	86	97.69	-11.69	13.59	107.37	-21.37	24.85
49	249	216.31	32.69	13.13	202.95	46.05	18.49
50	582	595.17	-13.17	2.26	610.21	-28.21	4.85
51	873	856.72	16.28	1.87	870.80	2.20	0.25

% Error, E = abs ((T-Y/T) x100)

It is clear from Table 4.2 that although based on quite different performance error functions, both methods seem to give similar results with the Trainlm training method yielded slightly better results than the Trainbr method. However, the main advantage of the Trainbr method is that it has an effective number of parameters (weights and biases) which remains approximately the same irrespective of the total number of parameters in the network until a sufficient number of iterations is achieved. By contrast, training by the Trainlm method is relatively simple and fast. Table 4.3 provides a summary of the network architecture, development, and results obtained from modeling by both methods.

Table 4.3: Training parameters used and results obtained from modeling of the γ' precipitate size

Network	Parameters	Trainlm	Trainbr
Network architecture	Input layer neurons	13	13
	Hidden layer neurons	13	17
	Output layer neurons	1	1
	Input-hidden layer transfer function	Tansig	Tansig
	Hidden-output layer transfer function	Linear	Linear
Network development	Training function	Trainlm	Trainbr
	Mu	1	1
	Mu-Dec	0.4	0.4
	Mu-Inc	1.5	1.5
	Min-Grad	1.00×10^{-10}	1.00×10^{-10}
	Epochs	36	158
	Goal	0	0
Network results (Linear regression)	Slope m	0.99	0.98
	y-Intercept b	1.5	2.9
	Correlation coefficient R	0.99542	0.9939

For both Trainlm and Trainbr models, the network architectures converge and stabilize well because of the batch mode of training and the small number of data points that allows both Trainlm and Trainbr methods to perform well and predict the outputs efficiently [69,71]. Moreover, both Trainlm and Trainbr methods seem to give similar results with only a slight advantage for Trainlm method as can be seen from all the results presented. Therefore, the preference of the Trainlm method over the Trainbr method in this work is primarily made based on computational time needed to optimize the model since the entire process took approximately one hour for the Trainlm method and 2-3 hours for the Trainbr method as mentioned previously. The same reasoning applies to the preference of the Trainlm method over the Trainbr method for all subsequent models since respective available data sets were even smaller than that of the γ’ precipitate size modeling, making the basis for training method selection identical.

4.1.2 γ’ precipitates size as a function of ageing methods

In order to highlight the importance of various ageing methods, the neural network modeling is applied on the turbine blade material (IN738LC) to predict the γ’ precipitate size. A new model containing 10 variables including solutionizing temperature, solutionizing duration, quenching methods, ageing temperature, ageing duration, and cooling methods, is created for IN738LC material. Radiation furnace and induction heating are considered for ageing investigation. Induction heating is characterized by electromagnetic forces that intensify the nucleation and growth of γ’ precipitates and is known to accelerate the ageing process. The data used for this study, taken from literature, are given in Table 4.4 [10,20,115-117].

Table 4.4: Inputs, targets, and their ranges for modeling the effect of ageing methods on the γ’ precipitate size [10,20,115-117].

Nr.	Input parameters	Ranges
1	Ageing temperature (°C)	650-1200
2	Ageing duration (min)	10-1440
3	Furnace cooling (FC)	0 or 1
4	Water quenching (WQ)	0 or 1
5	Induction ageing	0 or 1
6	Salt bath ageing	0 or 1
7	Solutionizing temperature (^{o}C)	1125-1250
8	Solutionizing duration (min)	120-240
9	Accelerated air cooling (ACC)	0 or 1
10	Oil quenching (OQ)	0 or 1
1	Target, T (γ' size, nm)	115-686

Note that for the different heat treatments, 0 means not used and 1 means used.

Figure 4.5 shows modeling results (curves) and measurement data points for the γ' precipitate size following induction ageing as a function of ageing time (duration) for two different ageing temperatures, 750^{o}C and 850^{o}C [118]. A very good match and correlation can be seen. Moreover, it can also be seen from Figure 4.5 that for a given ageing duration, the size of γ' precipitates is larger for 850^{o}C than that of 750^{o}C. This illustrates the large impact of temperature on diffusion rate, phase transformation, and consequently, γ' precipitate size. The increase in temperature from 750^{o}C to 850^{o}C accelerates the diffusion process and ultimately results in a substantial increase in the γ' precipitate size.

Modeling results for γ' precipitates sizes following ageing using either induction or radiation furnace heating are plotted together with the measurement data points in Figure 4.6 [118]. In this Figure, the ageing time for induction ageing is 15 minutes while the ageing time for furnace ageing is 24 hours. The faster increase in γ' precipitate size for induction ageing as compared to normal ageing can be clearly seen. The electromagnetic force during induction heating raises the effective driving force for the nucleation and growth of γ' precipitates remarkably [115].

The γ' precipitate structure can be directly related to high temperature properties of turbine materials. Therefore, modeling of the γ' precipitates size can be very useful for estimating the service life in addition to predicting the microstructure of turbine components.

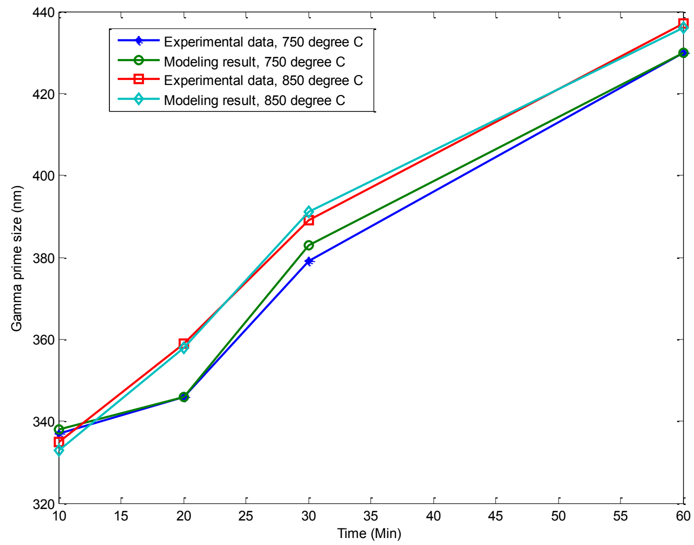

Figure 4.5: γ’ precipitate size vs. ageing time at 750^{o}C and 850^{o}C. Neural network results (curves) and measurement data points are plotted.

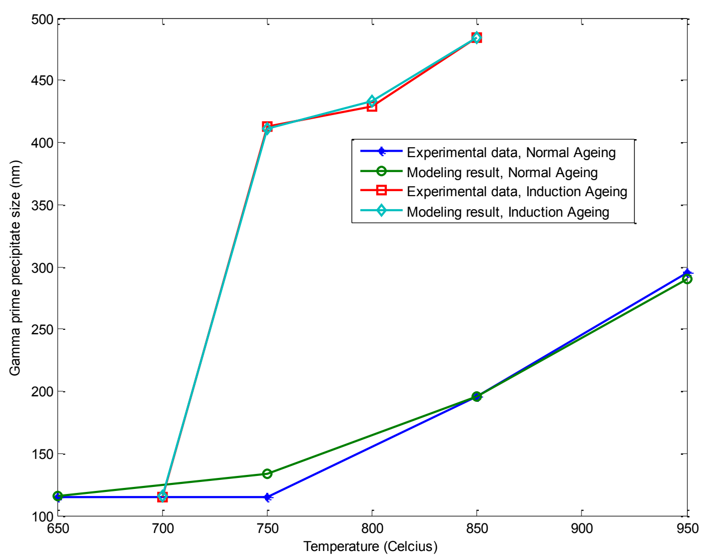

Figure 4.6: γ’ precipitate size vs. ageing temperature for normal (ageing duration: 24 hrs) and induction ageing (ageing duration: 15 minutes). Modeling results and measurement data points are plotted [118].

4.2 Thermal expansion coefficient

As explained in section 2.1.2, the thermal expansion is one of the most important design factors for turbine blades and other hot turbine components because the magnitude of thermal stresses can potentially initiate plastic deformation and cracks. Previous research has attempted to measure the thermal expansion coefficient of Ni based superalloys using either standard dilatometer test method or X-ray diffraction technique [4,6]. An equation to determine the thermal expansion coefficient of Ni based superalloys has also been derived based on either regression analysis or a simple algorithm using features of the binding energy curve [3,7,8]. These approaches are limited to low temperatures and provides only a rough estimate for higher temperatures. Therefore, new computational approaches need to be developed that are fast, easy, and allow measuring the thermal expansion coefficient at any temperature. The neural network has been previously employed in the mechanical and physical properties determination [77-88]. No attempt has been made to model the thermal expansion coefficient of γ' precipitate strengthened Ni based superalloys using neural networks. Therefore, it is crucial to study the relationship between the operating temperature, chemical composition, heat treatment, and thermal expansion coefficient of turbine components interacting with each other. For this purpose, a neural network model is developed to predict the thermal expansion coefficient of γ' precipitate strengthened Ni based superalloys. The chemical compositions of the materials used in the modeling are summarized in Table 3.1 [11, 109,111]. They are materials often used in discs and blades which are amongst the most critical components of turbine engines.

To model the thermal expansion coefficient, temperature, chemical composition including Ni, Cr, Co, Mo, W, Ta, Nb, Al, Ti, B, Zr, C contents and heat treatment including solution and ageing parameters are taken from literature as the input variables. Thermal expansion coefficient values from literature for each corresponding inputs are used as targets. Inputs, targets and their ranges are given in Table 4.5 [4,11,109,111].

Table 4.5: Inputs, targets, and their ranges [4,11,109,111] for modeling of the thermal expansion coefficient

Nr.	Input Parameters	Ranges
1	Temperature (^oC)	204.50-982.23
2	Solution temperature (^oC)	1079.45-1200
3	Solution time (hr)	1.5-4.0
4	Chilled water quenching (CWQ)	0 or 1
5	Air cooling (AC_s)	0 or 1
6	Primary ageing temperature (^oC)	0-1140
7	Primary ageing time (hr)	0-24
8	Water quenching (WQ)	0 or 1
9	Air cooling (AC_a)	0 or 1
10	Furnace cooling (FC)	0 or 1
11	Nickel content (wt %)	48-73
12	Chromium content (wt %)	9.0-19.5
13	Cobalt content (wt %)	0-18
14	Molybdenum content (wt %)	0-5.25
15	Tungsten content (wt %)	0-10
16	Tantalum content (wt %)	0-1.75
17	Niobium content (wt %)	0-1
18	Aluminum content (wt %)	0.7-6.0
19	Titanium content (wt %)	0.6-4.7
20	Boron content (wt %)	0-0.03
21	Zirconium content (wt %)	0-0.1
22	Carbon content (wt %)	0.04-0.15
1	Target, T (α , $10^{-6}/^oC$)	12.57-17.46

AC_s and AC_a refer to air cooling during solutionizing and ageing heat treatment respectively.

A total of 50 data points is used for modeling of the thermal expansion coefficient. In order to avoid over-fitting, the total data set is randomly divided into three subsets; a training subset (50% of the total data set), a validation subset (25% of the total data set), and a test subset (25% of the total data set). Other detailed information of materials, including test temperature, heat treatment, and measured target values of the thermal expansion coefficient covered in this study, are given in Appendix A, Table A2.

The Levenberg-Marquadt training method is used for modeling of the thermal expansion coefficient. After training, the final network architecture consists of a three layered feedforward backpropagation neural network with one input layer, one hidden layer, and one output layer. After a number of trials, the most suitable architecture obtained is 22-25-1; this means 22 neurons in the input layer, 25 neurons in the hidden layer, and 1 neuron in the output layer.

Figure 4.7 shows curves for the convergence characteristics including training, validation and testing data subsets. The performance is 1.43335×10^{-6} which is very small. Figure 4.8 shows the mean squared error vs. epoch curves for training, validation, and testing data subsets, respectively. Initially, the mean squared errors for both training and validation subsets decrease and then become constant and the training stops at 8 epochs or iterations. It can be seen from Figure 4.8 that the testing curve also follows the same pattern, which indicates that no over-fitting occurred and the network is properly trained. The values obtained from the modeling of the thermal expansion coefficient (output of the network), the corresponding target values from literature and their corresponding % errors for testing data subset are summarized in Table 4.6. It can be seen that there is a good correlation between the output (Y) and the target (T) values and the percentage errors are small.

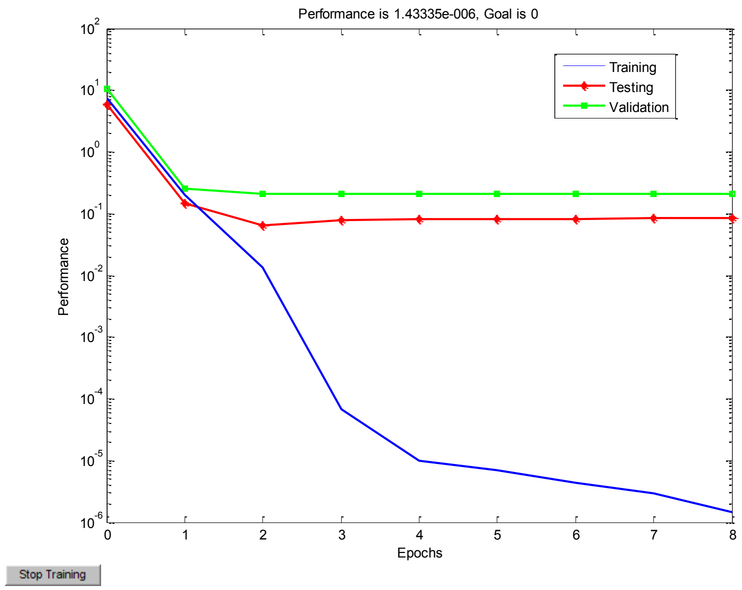

Figure 4.7: Convergence characteristics of the network for the thermal expansion coefficient modeling.

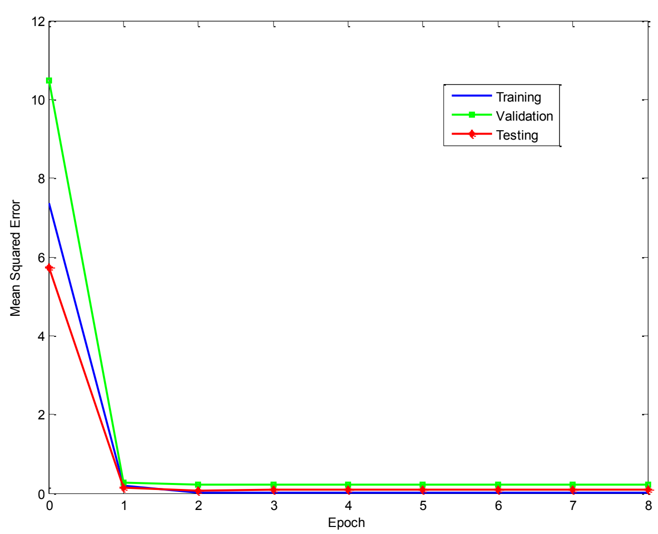

Figure 4.8: Mean squared error vs. epoch for the thermal expansion coefficient modeling.

Table 4.6: Inputs, targets, and corresponding % errors obtained from testing data subset for the thermal expansion coefficient modeling

Nr.	Target, T	Output, Y	T-Y	% Error, E
1	13.220	13.162	0.058	0.439
2	13.260	13.329	-0.069	0.519
3	13.400	13.415	-0.015	0.112
4	12.840	12.837	0.003	0.023
5	18.300	18.058	0.242	1.322
6	14.400	14.234	0.166	1.153
7	13.500	11.617	1.883	13.948
8	13.900	14.559	-0.659	4.741
9	14.000	13.753	0.247	1.764
10	14.000	14.287	-0.287	2.050
11	16.000	15.927	0.073	0.456
12	16.760	17.025	-0.265	1.581
13	15.700	15.705	-0.005	0.032

% Error, E = abs ((T-Y/T) x100)

The linear regression analysis is also performed and the parameters obtained from the presented model are m = 1.03; b = -0.393 and R = 0.966. Those parameters are very close to ideal values (m = 1; b = 0; R = 1) and indicate a good fit. The best linear regression fit for the investigated data set is shown in Figure 4.9 by the solid line. The theoretical one-to-one correspondence line between the network outputs and the targets is shown as a dashed line. Both lines practically overlap, which indicates the high accuracy of the model. The training parameters used and results obtained from the modeling are summarized in Table 4.7.

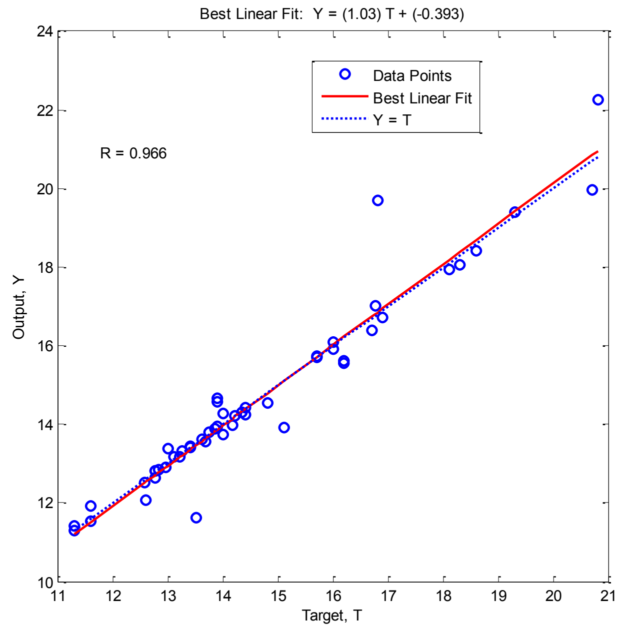

Figure 4.9: Linear regression analysis for the thermal expansion coefficient modeling.

Table 4.7: Training parameters used and results obtained from the thermal expansion coefficient modeling

Network	Parameters	Value
	Input layer neurons	22
	Hidden layer neurons	25
Network architecture	Output layer neurons	1
	Input-hidden layer transfer function	Tansig
	Hidden-output layer transfer function	Linear
	Training function	Trainlm
	Mu	1
	Mu-Dec	0.4
	Mu-Inc	1.4
Network development	Min-Grad	1.00×10^{-10}
	Epochs	8
	Goal	0
Network results	Slope m	1.03
(Linear regression)	y-Intercept b	-0.393
	Correlation coefficient R	0.966

The proposed network is able to model the thermal expansion coefficient of different Ni based superalloys. There is a good match between measurement data and modeling results. The model develops and converges very well because the number of data points available for modeling is small, which allowed the Levenberg-Marquadt algorithm to perform well and to predict the outputs efficiently [69]. This excellent modeling result opens new avenues and demonstrates the potential of the neural network to become a key design tool for assessing the behaviour of critical high temperature components. Due to existing direct correlations between the thermal expansion coefficient, thermal stresses, microstructure, and heat treatment of γ' precipitated Ni based superalloys, the modeled thermal expansion coefficients can potentially be used to predict thermal stresses between the base materials and coatings as well as between neighbouring turbine components for given operating temperature profiles. The modeled stresses can then further be used as input to assess component deformation, damage, and failure. In fact, coating, substrate components, and their neighbouring components often differ in chemical composition, microstructure, thermal expansion, Young's modulus, yield strength, creep behaviour, fatigue life, and other physical and mechanical properties [119]. This mismatch of properties may cause stresses at interfaces between the substrate and the coating as well as between the substrate and its neighbouring components, and the resulting residual strains and stresses can overlap with the workload of the component which can promote coating cracking and spallation as well as plastic deformation, accelerated corrosion, cracking, and ultimately failure of the main substrate component [119-122]. Following this philosophy, G. Parthasarathy et al. applied the neural network to predict the temperature at several critical locations of a Honeywell turbo-machinery component using rotational speed, related gas temperature, and gas flow near the component as inputs. They suggested that the same neural network approach can also be used for the computation of thermal stress at a critical component location [123]. Also, U. Hermosilla et al. developed a constitutive model to estimate the Young's modulus, creep behaviour, and the coefficient of thermal expansion and then incorporated their simulation into a material model within a finite element analysis of the stress development within the coated system [124]. Furthermore, E.P. Busso et al. proposed a novel mechanism-based life approach to predict the life of thermal barrier coating (TBC) systems based on a combination of TBC's morphological characteristics, accumulated TBC damage, and numerically predicted local TBC stresses responsible for the initiation of such damage [125]. Also, following physics based life prediction methodology, P. Busso et al. investigated local stresses responsible for crack formation and growth within a thermal barrier coating of turbine components and predicted the lifetime of the coating system using the modeled stresses. The approach was based on thermal stresses, material properties of the individual components, morphological properties of the material microstructure, and its damage behaviour prior to coating failure, etc. [126].

4.3 Fatigue life

The combination of complex thermal and mechanical service conditions in aggressive environments facilitates crack initiation, followed by crack propagation, and final fracture. The fatigue life is the sum of crack initiation life and crack propagation life. Several fatigue life prediction methods have been developed to predict fatigue life [26-31]. Various neural network models to predict fatigue crack growth rate, fatigue life, and fatigue properties of Ni based superalloys are available in the literature [91-104]. However, very little has been done so far to combine both fracture mechanics and neural network approaches for a comprehensive prediction of the fatigue lives of turbine disc materials. Therefore, in this section, fracture mechanics and neural network approaches have been explored to predict the fatigue lives of turbine disc alloys. These two approaches are explained as follows.

4.3.1 Fracture mechanics approach for fatigue life prediction

Ni based superalloys used for aerospace engines and other turbine components are subjected to severe fatigue and creep loading conditions that promote unstable propagation of cracks. Once cracks reach a critical size, catastrophic fracture occurs. Due to the lack of literature data for critical crack lengths, the critical crack lengths of Ni based superalloys for different load levels are first determined using fracture mechanics principles and then used to estimate the corresponding fatigue lives.

4.3.1.1 Critical crack size determination

The materials investigated are IN100, Waspaloy, Rene 95, Merl 76, Astroloy, and HIP Astroloy which are used for making turbine discs. Individual material's compositions, grain sizes, and γ' volume fraction levels vary from alloy to alloy.

In order to predict the component life using fracture mechanics, both initial and critical crack lengths are required. The critical crack length (c_f) can be estimated using equation (17) (see section 3.3.1.1). For most Ni based superalloys, the fracture toughness, K_{IC}, is about 100 MPa.m$^{1/2}$ [1] and for a semicircular edge crack, Y = 0.67 [1] is assumed. The experimental literature data used are given in Table 4.8 which includes the stress range ($\Delta\sigma$), mean stress (σ_m), strain ratio, and total strain. The maximum and the alternating stress or stress amplitude (σ_a) are determined by using equation (18) and equation (19) respectively. The calculated critical crack length (c_f), alternating stress σ_a, and maximum stress σ_c are also given in Table 4.8.

4.3.1.2 Crack propagation life determination

The Paris equation (6) is used for the crack propagation life prediction (see sections 2.3.1.3 and 3.3.1.2). The value of A for turbine disc alloys is taken as 4.00×10^{-12} [1]; the crack initiation size c_0 is assumed to be 2.50×10^{-4} meter [112]; m is known to be between 3 to 4 for superalloys [1]; therefore, a value of 3.71 is used and proved to yield minimum errors. Substituting these values in equation (6), the estimated life is given in Table 4.9 for the corresponding data sets in Table 4.8. Once the crack propagation life is predicted using fracture mechanics concepts, the crack initiation life is added to the crack propagation life to get the total fatigue life of turbine disc alloys. The crack initiation life, propagation life, and total calculated fatigue life are given in Table 4.9.

As can be seen from Table 4.9, errors between the experimental life and the predicted life are small. This confirms that the Paris equation can be successfully used for life prediction of turbine disc alloys.

Table 4.8: Experimental fatigue data [112] and corresponding σ_a, σ_c and c_f values

Nr.	Strain ratio, R	Total strain, $\Delta\varepsilon_t$ (mm/mm)	Mean stress, σ_m (MPa)	Stress range, $\Delta\sigma$ (MPa)	Alternating stress, σ_a (MPa)	Maximum stress, σ_c (MPa)	Critical crack length, c_f (mm)
1	-1	0.0147	-2	2377	1188.5	1186.5	6.09
2	-1	0.0101	-36	1791	895.5	859.5	11.6
3	0	0.009	-80	1600	800	720	16.6
4	0	0.0144	-74	2321	1160.5	1086.5	7.27
5	0	0.0124	161	2011	1005.5	1166.5	6.31
6	0	0.0099	286	1660	830	1116	6.89
7	0	0.0087	339	1496	748	1087	7.26
8	0	0.0147	-6	1742	871	865	11.5
9	0	0.0123	40	1696	848	888	10.9
10	0	0.0099	86	1594	797	883	11
11	0	0.0079	229	1393	696.5	925.5	10
12	0	0.0066	284	1157	578.5	862.5	11.5
13	0	0.0092	170	1476	738	908	10.4
14	-1	0.015	-37	2299	1149.5	1112.5	6.93
15	-1	0.0126	-60	2106	1053	993	8.7
16	-1	0.0116	-23	1951	975.5	952.5	9.46
17	-1	0.0108	-33	1904	952	919	10.2
18	-1	0.01	5	1730	865	870	11.3
19	-1	0.0199	-31	2707	1353.5	1322.5	4.91
20	0	0.0124	146	2046	1023	1169	6.28
21	0	0.01	347	1709	854.5	1201.5	5.94
21	0	0.009	367	1526	763	1130	6.72
23	-1	0.0184	-45	2634	1317	1272	5.3
24	-1	0.0151	-30	2342	1171	1141	6.59
25	-1	0.0119	-60	1995	997.5	937.5	9.76
26	-1	0.0109	-15	1798	899	884	11
27	-1	0.0091	25	1542	771	796	13.5
28	0	0.0117	194	1948	974	1168	6.29
29	-1	0.015	-41	2222	1111	1070	7.49
30	-1	0.0125	-37	2050	1025	988	8.79
31	-1	0.01	-57	1818	909	852	11.8
32	-1	0.01	-23	1787	893.5	870.5	11.3
33	-1	0.0085	-62	1539	769.5	707.5	17.1
34	-1	0.0085	-28	1575	787.5	759.5	14.9
35	-1	0.0072	0	1356	678	678	18.7
36	-1	0.0142	-56	1920	960	904	10.5
37	-1	0.01	-12	1674	837	825	12.6
38	-1	0.01	-19	1660	830	811	13
39	-1	0.0081	-12	1478	739	727	16.2
40	-1	0.0081	0	1466	733	733	16

Table 4.9: Crack initiation life (N_I), experimental crack propagation life (N_{Pexp}), calculated crack propagation life (N_{Pcal}), total experimental life (N_{Fexp}), total fracture mechanics fatigue life (N_{FM}), and % errors [112]

Nr.	N_I	N_{Pexp}	N_{Pcal}	N_{Fexp}	$N_{FM} = N_I + N_{Pcal}$	% Error, E
1	358	54	51.8	412	409.8	0.53
2	4968	480	152	5448	5120	6.02
3	52961	402	234	53363	53195	0.31
4	450	19	57.2	469	507.2	8.14
5	905	45	96.5	950	1001.5	5.42
6	2989	145	198	3134	3187	1.69
7	6041	301	292	6342	6333	0.14
8	753	75	169	828	922	11.35
9	1021	107	186	1128	1207	7.00
10	2733	292	234	3025	2967	1.92
11	14175	1750	385	15926	14560	8.58
12	60533	1930	771	62462	61304	1.85
13	4012	387	311	4399	4323	1.73
14	540	55	59.1	595	599.1	0.69
15	1387	103	82.7	1490	1469.7	1.36
16	4617	224	110	4841	4727	2.35
17	19042	1460	121	20502	19163	6.53
18	29302	2430	173	31729	29475	7.10
19	154	33	31.5	187	185.5	0.80
20	1059	20	90.5	1079	1149.5	6.53
21	3539	462	176	4001	3715	7.15
22	45885	594	270	46479	46155	0.70
23	240	31	35.1	271	275.1	1.51
24	701	17	55	718	756	5.29
25	1827	164	102	1991	1929	3.11
26	6764	323	150	7087	6914	2.44
27	120817	3510	267	124323	121084	2.61
28	1567	147	109	1714	1676	2.22
29	365	35	67.3	400	432.3	8.08
30	839	24	91.4	863	930.4	7.81
31	2214	553	144	2767	2358	14.78
32	1490	381	154	1871	1644	12.13
33	8979	371	271	9350	9250	1.07
34	6787	1050	247	7840	7034	10.28
35	226342	478	434	226820	226776	0.02
36	850	111	117	961	967	0.62
37	3800	225	196	4025	3996	0.72
38	2900	221	203	3121	3103	0.58
39	5110	3390	314	8498	5424	36.17
40	8176	725	323	8901	8499	4.52

% Error, E = abs ((N_{Fexp} - N_{FM} / N_{Fexp}) x100)

4.3.2 Neural network approach for fatigue life prediction

Here, the neural network is explored as an alternative to fracture mechanics for the fatigue life prediction. The common variables such as fatigue parameters (plastic strain range, strain ratio, and stress range), mechanical properties (ultimate strength, yield strength, and reduction in area), chemical compositions (Ni, Cr, Co, Mo, Al, Ti and C), and microstructural properties (grain size and volume fraction of γ' precipitates) are used as inputs. The selected inputs and targets and their ranges are given in Table 4.10. A total of 40 data points is used for modeling of the fatigue life. In order to avoid over-fitting, the total data set is randomly divided into three subsets; a training subset (50% of the total data set), a validation subset (25% of the total data set), and a testing subset (25% of the total data set).

Table 4.10: Inputs, targets, and their ranges [112] for modeling of the fatigue life

Nr.	Input Parameters	Ranges
1	Total strain, $\Delta\varepsilon_t$ (mm/mm)	0.0066-0.0199
2	Strain ratio, R	-1 or 0
3	Stress range, $\Delta\sigma$ (MPa)	1157-2707
4	Grain size, d (μm)	6-150
5	Volume fraction of γ', V_f (%)	20-62
6	Ultimate strength, σ_{UTS} (MPa)	1234-1440
7	Yield strength, σ_y (MPa)	881-1122
8	Reduction in Area, RA (%)	14.2-37.0
9	Nickel content (wt %)	54.84-69.22
10	Chromium content (wt %)	12.0-19.3
11	Cobalt content (wt %)	8.1-18.4
12	Molybdenum content (wt %)	3.1-5.2
13	Aluminum content (wt %)	1.3-5.1
14	Titanium content (wt %)	2.6-4.5
15	Carbon content (wt %)	0.023-0.09
1	Target, N_{Fexp} (cycle)	187-226820

The Levenberg-Marquadt training method is used for predicting the fatigue life. After a number of trials, the most suitable architecture obtained is 15-15-1; this means 15 neurons in the input layer, 15 neurons in the hidden layer and one neuron in the output layer. The performance is 3.51189 that is far from the goal value of zero. Figure 4.10 shows the mean squared error vs. the number of epochs for training, validation, and testing subsets. Initially, the mean squared errors for training, validation, and testing subsets decrease and then become constant and the training stops at 14 epochs. It can also be seen from Figure 4.10 that the testing curve follows a pattern that is somewhat different from training and validation subsets, which indicate that the network architecture is relatively less satisfactory with respect to stability.

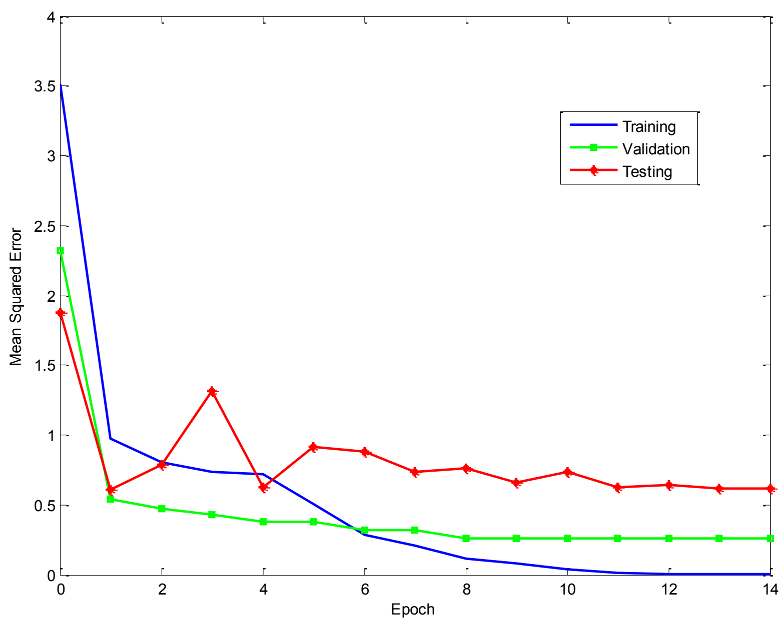

Figure 4.10: Mean squared error vs. epoch for modeling of the fatigue life.

The output obtained from modeling of the fatigue life, the target values and their corresponding % errors for the testing subset are summarized in Table 4.11. It can be seen that there is a big difference between the outputs (Y) and the targets (T) and the percentage errors are large due to the lack of correlation between corresponding inputs and targets.

Table 4.11: Inputs, targets, and corresponding % errors obtained from testing data subsets for modeling of the fatigue life

Nr.	Target, T	Output, Y	T-Y	% Error, E
1	5448	49417.74	-43969.74	807.08
2	3134	27375.23	-24241.23	773.49
3	3025	-35929.50	38954.51	1242.75
4	595	-1912.30	2507.30	421.39
5	31729	14851.73	16877.27	53.19
6	46479	12579.27	33899.73	72.94
7	7087	49095.06	-42008.06	592.75
8	863	9982.36	-9119.36	1056.70
9	7840	82987.68	-75147.68	958.52
10	3121	9487.04	-6366.04	203.97

% Error, E = abs ((T-Y/T) x100)

The parameters obtained from the linear regression analysis are m = 0.8; b = 1.1×10^4 and R = 0.84802. The solid line in Figure 4.11 represents the best linear fit. The theoretical one-to-one correspondence line between the network outputs and the targets is shown as a dashed line. Overall, it can be seen that although accurate in predicting systemic trends, the neural network seems unable to replicate the strong statistical variations and quasi-unpredictability common in the fatigue life. Still, the model's convergence is satisfactory and the linear regression line matches data points relatively well as can be seen in Figure 4.11. The training parameters used and results obtained from modeling are summarized in Table 4.12.

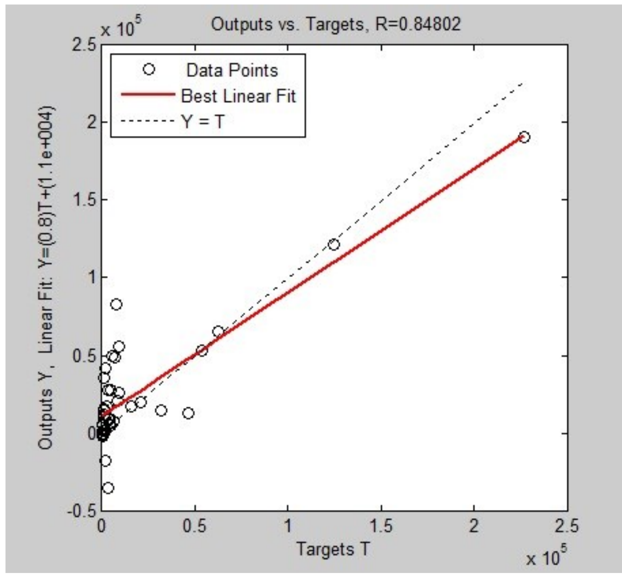

Figure 4.11: Linear regression analysis for modeling of the fatigue life.

Table 4.12: Training parameters used and results obtained from modeling of the fatigue life

Network	Parameters	Value
Network architecture	Input layer neurons	15
	Hidden layer neurons	15
	Output layer neurons	1
	Input-hidden layer transfer function	Tansig
	Hidden-output layer transfer function	Linear
Network development	Training function	Trainlm
	Mu	0.99
	Mu-Dec	0.3
	Mu-Inc	1.5
	Min-Grad	1.00×10^{-10}
	Epochs	14
	Goal	0
Network results (Linear regression)	Slope m	0.8
	y-Intercept b	1.1×10^{4}
	Correlation coefficient R	0.84802

4.4 Hysteresis energy

During a fatigue cycle, a hysteresis loop develops between the stress and strain and the material absorbs a certain amount of energy (ΔW) called hysteresis energy. Fatigue fracture occurs after the material has accumulated a critical amount of energy over a given number of cycles called its service life. The hysteresis energy can be used for total fatigue damage prediction. Several experimental studies and models have also been used to determine the hysteresis energy of materials [26-29]. However, the neural network is yet to be investigated in this field. Therefore, this section focuses on predicting the hysteresis energies of Ni based superalloys. Two different methods are used; the hysteresis area loop equation and the neural network approach. Both methods for hysteresis energy prediction are explained in following sections.

4.4.1 Hysteresis energy determination using the area equation

The hysteresis loop area equation (1) is used for estimating the hysteresis energy. The same materials used for fracture mechanics crack propagation life assessment as presented in section 4.3.1 and Table 3.1 are also considered here. Table 4.13 gives the literature experimental values for investigated turbine disc alloys at 650^{o}C as well as corresponding hysteresis energies values determined from equation (1). The average value of n' for a duplex γ' precipitates Ni based superalloy is given in literature as 0.11 [127] which is also used here. The values of the hysteresis energies are considered as targets for the neural network model development.

Table 4.13: Experimental data at 650^{o}C [112] and their corresponding hysteresis energies

Nr.	Plastic strain range, $\Delta\varepsilon_p$ (mm/mm)	Stress range, $\Delta\sigma$ (MPa)	Strain hardening coefficient, n'	Hysteresis energy using area equ, ΔW_A (kJ/m^3)	Hysteresis energy using neural network, ΔW_{NN} (kJ/m^3)
1	0.0013	2377	0.11	2783.874	2785
2	0.0001	1791	0.11	161.351	333
3	0.0001	1600	0.11	144.144	148
4	0.001	2321	0.11	2090.991	2088
5	0.0003	2011	0.11	543.514	555
6	0.0001	1660	0.11	149.550	174
7	0.0001	1496	0.11	134.775	132
8	0.0047	1742	0.11	7376.036	8847
9	0.0026	1696	0.11	3972.613	3948
10	0.001	1594	0.11	1436.036	1227
11	0.002	1393	0.11	2509.910	2571
12	0.0001	1157	0.11	104.234	153
13	0.0004	1476	0.11	531.892	511
14	0.0019	2299	0.11	3935.225	4289
15	0.0007	2106	0.11	1328.108	1335
16	0.0004	1951	0.11	703.063	711
17	0.0002	1904	0.11	343.063	318
18	0.0002	1730	0.11	311.712	368
19	0.0042	2707	0.11	10242.703	10202
20	0.0007	2046	0.11	1290.270	2102
21	0.0001	1709	0.11	153.964	172
22	0.0001	1526	0.11	137.477	-22
23	0.0026	2634	0.11	6169.730	6183
24	0.0006	2342	0.11	1265.946	1222
25	0.0001	1995	0.11	179.730	176
26	0.0001	1798	0.11	161.982	165
27	0.0001	1679	0.11	151.261	163
28	0.0002	1948	0.11	350.991	-135
29	0.0026	2222	0.11	5204.685	5212
30	0.0011	2050	0.11	2031.532	1894
31	0.0002	1818	0.11	327.568	374
32	0.0002	1787	0.11	321.982	363
33	0.0001	1539	0.11	138.649	141
34	0.0001	1575	0.11	141.892	152
35	0.0001	1356	0.11	122.162	84
36	0.0032	1920	0.11	5535.135	5823
37	0.0004	1674	0.11	603.243	595
38	0.0004	1660	0.11	598.198	590
39	0.0001	1478	0.11	133.153	174
40	0.0001	1466	0.11	132.072	171

4.4.2 Hysteresis energy determination using neural networks

An artificial neural network is explored as an alternative to the hysteresis loop area equation. As the selection of inputs is very important for optimal network development, fatigue variables (plastic strain range, strain ratio, and stress range), mechanical properties (ultimate strength, yield strength, and reduction in area), chemical composition (Ni, Cr, Co, Mo, Al, Ti, and C), and microstructural properties (grain size and volume fraction of γ' precipitates) are also taken as inputs for consistency with modeling of the fatigue life in section 4.3.2. The modeled hysteresis energy values are then used for accumulated damage determination in the following sections. The selected inputs and targets are given in Table 4.14. A total of 40 data points is used for modeling of the hysteresis energy. In order to avoid over-fitting, the total data set is randomly divided into three subsets; a training subset (50% of the total data set), a validation subset (25% of the total data set), and a testing subset (25% of the total data set).

The feedforward Levenberg-Marquadt backpropagation algorithm is used for modeling of the hysteresis energy to iteratively update the weights and biases to minimize the mean squared error. After a number of trials, the most suitable architecture obtained is 15-19-1; this means 15 neurons in the input layer, 19 neurons in the hidden layer, and one neuron in the output layer. The performance is 2.2126×10^{-13} which is very small. Figure 4.12 shows the mean squared error vs. the number of epochs for training, validation, and testing subsets. Initially, the mean squared errors for training, validation, and testing subsets decrease and then become constant and the training stops at 9 epochs. It can be seen from this result that the testing curve also follows the same pattern, which indicates that the network architecture is satisfactory with respect to stability. All three curves follow the same pattern indicating that no over-fitting occurred and the network is properly trained.

Table 4.14: Inputs, targets, and their ranges [112] for modeling of the hysteresis energy

Nr.	Input Parameters	Ranges
1	Plastic strain range, $\Delta\varepsilon_p$ (mm/mm)	0.0001-0.0042
2	Strain ratio, R	-1 or 0
3	Stress range, $\Delta\sigma$ (MPa)	1157-2707
4	Grain size, D (μm)	6-150
5	Volume fraction, V_f (%)	20-62
6	Ultimate strength, σ_{UTS} (MPa)	1234-1440
7	Yield strength, σ_y (MPa)	881-1122
8	Reduction in area, RA (%)	14.2-37.0
9	Nickel content (wt %)	54.84-69.22
10	Chromium content (wt %)	12.0-19.3
11	Cobalt content (wt %)	8.1-18.4
12	Molybdenum content (wt %)	3.1-5.2
13	Aluminum content (wt %)	1.3-5.1
14	Titanium content (wt %)	2.6-4.5
15	Carbon content (wt %)	0.023-0.09
1	Target, ΔW (kJ/m^3)	104.23-7376.04

The output obtained from the modeling of the hysteresis energy, the target values and their corresponding % errors for the testing subset are summarized in Table 4.15. It can be seen that there is a good correlation between the output (Y) and the target (T) values and the percentage error is small. As can be seen from Table 4.15, however, some of the errors are relatively large due to the lack of correlations between corresponding inputs and targets.

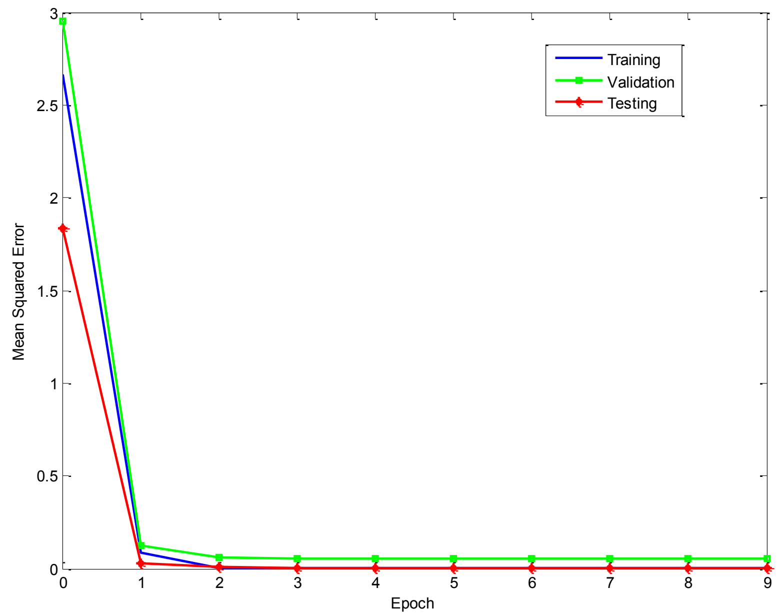

Figure 4.12: Mean squared error vs. epoch for modeling of the hysteresis energy.

Table 4.15: Inputs, targets, and corresponding % errors obtained from testing data subsets for modeling of the hysteresis energy

Nr.	Target, T	Output, Y	(T-Y)	% Error, E
1	161.25	333.42	-172.07	106.64
2	149.55	173.66	-24.11	16.12
3	1436.04	1226.93	209.11	14.56
4	3935.29	4289.24	-353.95	8.99
5	311.71	367.90	-56.19	18.03
6	137.48	22.18	115.30	83.87
7	161.78	165.48	-3.70	2.29
8	2031.53	1893.86	137.67	6.78
9	141.89	152.20	-10.31	7.27
10	598.20	590.45	7.75	1.30

% Error, E = abs ((T-Y/T) x100)

The parameters obtained from the linear regression analysis are m = 1; b = -16 and R = 0.99416. Those parameters are close to being ideal (m = 1; b = 0; R = 1) and indicate a good fit. The solid line in Figure 4.13 represents the best linear fit. The theoretical one-to-one correspondence line between the network outputs and the targets is shown as a dashed line. Both solid line and dashed line practically overlap, which indicate the high accuracy of the model and also shows that the neural network is successful in learning the relationship between the input and output variables. The training parameters used and results obtained from modeling are summarized in Table 4.16.

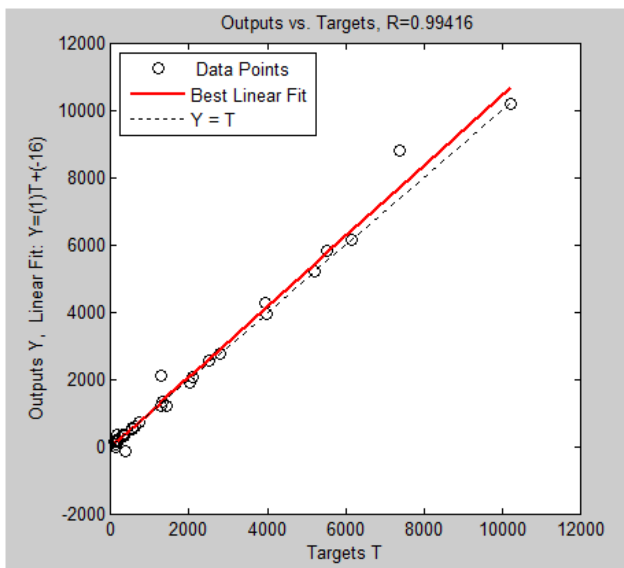

Figure 4.13: Linear regression analysis for modeling of the hysteresis energy.

Neural network results indicate that the network architecture is satisfactory with respect to stability and a satisfactory agreement is observed between calculated and modeled values.

Table 4.16: Training parameters used and results obtained from modeling of the hysteresis energy

Network	Parameter	Value
Network architecture	Input layer neurons	15
	Hidden layer neurons	19
	Output layer neurons	1
	Input-hidden layer transfer function	Tansig
	Hidden-output layer transfer function	Linear
Network development	Training function	Trainlm
	Mu	0.99
	Mu-Dec	0.3
	Mu-Inc	1.5
	Min-Grad	1.00×10^{-10}
	Epochs	9
	Goal	0
Network results (Linear regression)	Slope m	1
	y-Intercept b	-16
	Correlation coefficient R	0.99416

4.5 Fatigue damage prediction

As described in the previous section, materials absorb a certain amount of energy called hysteresis energy (ΔW) in each fatigue cycle. Knowing both the hysteresis energy and the number of cycles to failure (N_F) can allow assessing the approximate accumulated fatigue energy or damage (D_F) of components according to equation (20) [113]. The two hysteresis energies, i.e. energy obtained from the hysteresis area loop equation (ΔW_A) and energy obtained from the neural network modeling (ΔW_{NN}) are multiplied by the number of cycles to failure. The fatigue lives obtained from the neural network modeling are not used in fatigue damage calculation as the neural network results for fatigue life are not as good as other models. Rather, the crack propagation life calculated using fracture mechanics is added to the experimental crack initiation life in order to obtain the total number of cycles to failure used in this model. Table 4.17 shows the estimated fatigue damage absorbed by the materials during fatigue to failure according to equation (20).

Table 4.17: Fatigue damage calculation using both hysteresis energies ΔW_A and ΔW_{NN}

Nr.	Hysteresis energy using area equ ΔW_A [kJ/m^3]	Hysteresis enegy using NN, ΔW_{NN} [kJ/m^3]	Fatigue life using Fracture Mechanics, N_{FM} [kJ/m^3]	Fatigue Damage $D_{FA} = \Delta W_A \times N_{FM}$ [kJ/m^3]	Fatigue Damage $D_{FNN} = \Delta W_{NN} \times N_{FM}$ [kJ/m^3]	% Error, E
1	2783.874	2785	409.8	1140832	1141293	0.04
2	161.351	333	5120	826117.1	1704960	106.38
3	144.144	148	53195	7667740	7872860	2.68
4	2090.991	2088	507.2	1060551	1059034	0.14
5	543.514	555	1001.5	544329.3	555832.5	2.11
6	149.55	174	3187	476615.9	554538	16.35
7	134.775	132	6333	853530.1	835956	2.06
8	7376.036	8847	922	6800705	8156934	19.94
9	3972.613	3948	1207	4794944	4765236	0.62
10	1436.036	1227	2967	4260719	3640509	14.56
11	2509.91	2571	14560	36544290	37433760	2.43
12	104.234	153	61304	6389961	9379512	46.79
13	531.892	511	4323	2299369	2209053	3.93
14	3935.225	4289	599.1	2357593	2569540	8.99
15	1328.108	1335	1469.7	1951920	1962050	0.52
16	703.063	711	4727	3323379	3360897	1.13
17	343.063	318	19163	6574116	6093834	7.31
18	311.712	368	29475	9187711	10846800	18.06
19	10242.703	10202	185.5	1900021	1892471	0.40
20	1290.27	2102	1149.5	1483165	2416249	62.91
21	153.964	172	3715	571976.3	638980	11.71
22	137.477	-22	46155	6345251	-1015410	116.00
23	6169.73	6183	275.1	1697293	1700943	0.22
24	1265.946	1222	756	957055.2	923832	3.47
25	179.73	176	1929	346699.2	339504	2.08
26	161.982	165	6914	1119944	1140810	1.86
27	151.261	163	121084	18315287	19736692	7.76
28	350.991	-135	1676	588260.9	-226260	138.46
29	5204.685	5212	432.3	2249985	2253148	0.14
30	2031.532	1894	930.4	1890137	1762178	6.77
31	327.568	374	2358	772405.3	881892	14.17
32	321.982	363	1644	529338.4	596772	12.74
33	138.649	141	9250	1282503	1304250	1.70
34	141.892	152	7034	998068.3	1069168	7.12
35	122.162	84	226776	27703410	19049184	31.24
36	5535.135	5823	967	5352476	5630841	5.20
37	603.243	595	3996	2410559	2377620	1.37
38	598.198	590	3103	1856208	1830770	1.37
39	133.153	174	5424	722221.9	943776	30.68
40	132.072	171	8499	1122480	1453329	29.47

% Error, E = abs ((D_{FA} - D_{FNN}/D_{FA}) x100)

It is clear from Table 4.17 that the fatigue damages obtained using both hysteresis energies (ΔW_A and ΔW_{NN}) are in good agreement.

4.6 Deformation mechanism map

Several deformation mechanism maps have been constructed for different engineering alloys using rate equations for different creep mechanisms [43-67] that were validated using experimental data only. New approaches also need to be developed that can allow a cross-check of the validity of the emerging deformation mechanism maps, particularly in cases where experimental data are very limited. Therefore, a deformation mechanism map for 1.23Cr-1.2Mo-0.26V steel considering dislocation glide, power law creep (PLC), and grain boundary sliding (GBS) accommodated by both wedge type cracking and creep cavitation, is constructed and validated using both experimental data and artificial neural network modeling results in this work. The map is constructed at a constant grain size of 100μm because the creep testing data for this material are available for this grain size only. Generally, 80-100 μm is standard for most steels used for turbine disc applications. The following paragraphs explain the steps involved in plotting the deformation mechanism map.

4.6.1 Creep deformation mechanisms and rate equations

The 1.23Cr-1.2Mo-0.26V rotor steel, explained in sections 2.2 and 3.2, is selected for constructing the deformation mechanism map. The high creep strength of 1.23Cr-1.2Mo-0.26V steel is obtained through a combination of transformation and precipitation hardening mechanisms. Creep testing results on a retired turbine disc after 100000 hours of service in a temperatures range from 500 to 675°C with creep stresses varying between 7 to 40 kg/mm^2 are taken for the construction of the deformation mechanism map [17]. The minimum creep rate data as a function of applied stress at different temperatures showing a clear power law breakdown (PLB) is reproduced in Figure 4.14 [17].

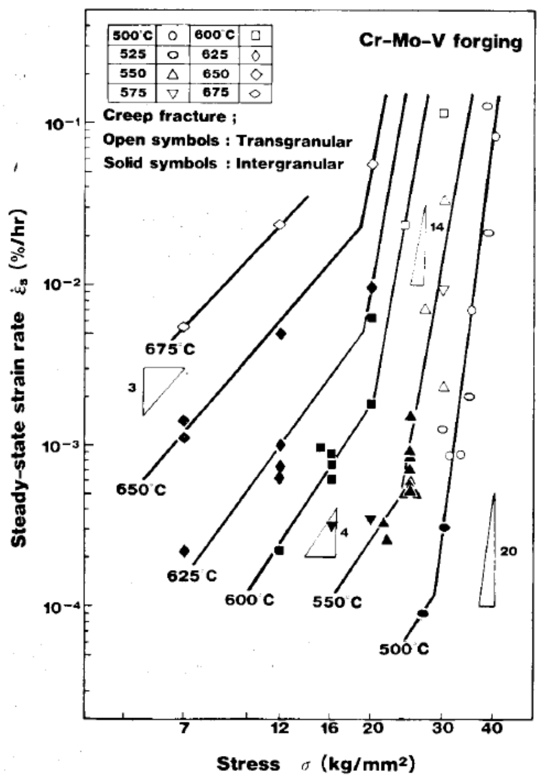

Figure 4.14: Steady state strain rate vs. stress diagram of Cr-Mo-V steel showing the power law breakdown at various temperatures [17].

Based on the results of creep tests of 1.23Cr-1.2Mo-0.26V steel [17], an obstacle-controlled dislocation glide is assumed to be operative at lower temperatures whereas PLC and GBS mechanisms are considered dominant at higher temperatures above and below the PLB stresses, respectively. All equations are expressed as a function of shear stress and strain only, therefore, creep stress (σ) and strain rate ($\dot{\varepsilon}$) values are converted to shear stress (τ_s) and shear strain rate ($\dot{\gamma}$) data using equations (24) and (25), respectively [40]:

$$\tau_s = \frac{\sigma}{\sqrt{3}} \tag{24}$$

$$\dot{\gamma} = \sqrt{3}\,\dot{\varepsilon} \tag{25}$$

Obstacle-controlled dislocation glide: 1.23Cr-1.2Mo-0.26V steel contains carbide particles that hinder dislocation glide resulting in a contribution to the flow strength. The following rate equation (see section 3.3.4) for discrete obstacle-controlled plasticity by particle shearing has been used [40,114]:

$$\dot{\gamma}_{DG} = \dot{\gamma}_0 \exp\left[-\frac{\Delta F}{kT}\left(1-\frac{\tau_s}{\tau_0}\right)\right] \tag{21}$$

where $\dot{\gamma}_{DG}$ is the shear strain rate due to dislocation glide; $\dot{\gamma}_0$ is a pre-exponential constant; k is the Boltzmann constant; R is the gas constant; T is the temperature in Kelvin; τ_s is the applied shear stress; and ΔF denotes the activation energy for dislocation glide required to overcome the obstacles without any aid from external stresses. Therefore, the value of ΔF is taken to be about $2\mu_o b^3$ [40]; where μ_o is the shear modulus at zero K and b is the Burgers vector. τ_o, assumed to be proportional to $\mu b/\lambda$ where λ is the obstacle spacing, is the flow strength of the solid at zero K and is also called athermal flow strength [40,45]. In other words, τ_o is the stress forcing the dislocation through the obstacle with little thermal energy contribution. It is dependent on density and arrangement of the obstacles.

Grain boundary sliding (GBS): Langdon's GBS model [41,42,46,48] does not take into account the presence of grain boundary carbides or the back stresses opposing dislocation glide or climb that are often present in engineering materials. When a dislocation climbs along the particle/matrix interface at the grain boundary, the dislocation particle interaction produces a back stress, τ_{ic} that reduces the effective stress or the applied shear stress (τ_s) acting on the climbing dislocation to τ_s-τ_{ic}. In a similar way, the back stress opposing dislocation glide, τ_{ig}, arises from dislocation pile-up that form at all grain boundary precipitates and reduces the effective stress to τ_s-τ_{ig}. Therefore, the modified rate equation (see section 3.3.4) of GBS incorporating the effects of back stresses in the presence of grain boundary precipitates has been used that can be given by [56,59]:

$$\dot{\gamma}_{GBS} = A_{GBS} \frac{D_{gb}\mu b}{kT}\left(\frac{b}{d}\right)^{q}\left(\frac{\lambda + r}{b}\right)^{q-1} \frac{(\tau_s - \tau_{ig})(\tau_s - \tau_{ic})}{\mu^2} \tag{22}$$

where $\dot{\gamma}_{GBS}$ is the shear strain rate due to GBS; A_{GBS} is a non-dimensional constant; D_{gb} is the diffusion coefficient for grain boundary diffusion; λ is the grain boundary precipitate spacing (or ledge spacing for clean boundaries); r is the average radius of grain boundary particles (or ledge height); d is the grain size; q is the grain size index which takes values of 1 (without particles or ledges), 2 (for discrete particles), and 3 (for a continuous network of particles). Furthermore, the back stress τ_{ic} opposing dislocation climb can be given by [59,62]:

$$\tau_{ic} = \frac{\alpha\mu b}{\lambda} \tag{26}$$

where α is a factor depending on the degree of coherency of the precipitate particles. Simplifying assumptions are made about the size, shape, coherency, etc., of the carbide precipitate particles for the purpose of plotting the deformation mechanism map. The following assumptions are made:

1. Precipitate particles are spherical in shape [17,59]
2. q = 2 for discrete grain boundary particle distribution [59]
3. $\alpha = 1$ for coherent precipitate particle [59], therefore $\tau_{ic} = \mu b/\lambda$ [59]
4. $\tau_{ig} = \mu b/\lambda$ [62]
5. $\lambda = 2r$ [17]

Substituting all the assumptions listed above, equation (22) can be re-written as:

$$\dot{\gamma}_{GBS} = A_{GBS}\,\frac{D_{gb}\mu b}{kT}\left(\frac{b}{d}\right)^{2}\left(\frac{1.5\lambda}{b}\right)\left(\frac{\tau_s - \tau_b}{\mu}\right)^{2} \tag{27}$$

where τ_b is the back stress due to carbides.

Power law creep: At high temperatures, the ability of dislocations to glide and climb within the grain interiors is considered responsible for the dominance of power law creep above PLB and the strain rate dependence of creep strength increases. The rate equation incorporating the effect of back stress for a dislocation glide-climb controlled creep in terms of tensile stress (σ) and strain rate ($\dot{\varepsilon}$) can be given by [56]:

$$\dot{\varepsilon}_{PLC} = A_{PLC}\,\frac{D_v\mu b}{kT}\left(\frac{\sigma - \sigma_b}{\mu}\right)^{n} \tag{23}$$

Tensile stress and strain rate in equation (23) can be converted to shear stress and shear strain rate using equation (24) and (25) respectively. The equation for power law creep then becomes:

$$\dot{\gamma}_{PLC} = A_{PLC}\left(\sqrt{3}\right)^{n+1}\frac{D_v \mu b}{kT}\left(\frac{\tau_s - \tau_b}{\mu}\right)^n \tag{28}$$

where $\dot{\gamma}_{PLC}$ is the shear strain rate due to power law creep; A_{PLC} is a material constant for power law creep; (τ_s- τ_b) is the effective stress causing creep; n is a mechanism dependent exponent; D_v is the volume diffusivity at the test temperature and other parameters are the same as in equations (21) and (22).

4.6.2 Determination of physical constants

Values for the various physical constants in equations (21), (27), and (28) are required to construct the deformation mechanism map. They are determined either from experimental data or from appropriate assumptions.

Diffusion coefficient (D) and activation energy (Q): Diffusion coefficients for grain boundary (D_{gb}) and volume (D_v) diffusion can be expressed by equations (29) and (30), respectively:

$$D_{gb} = D_{0gb}\exp\left(\frac{-Q_{gb}}{RT}\right) \tag{29}$$

$$D_v = D_{0v}\exp\left(\frac{-Q_v}{RT}\right) \tag{30}$$

where D_{ogb}, Q_{gb} and D_{ov}, Q_v are pre-exponential terms and activation energies for grain boundary and volume diffusion, respectively and R is the gas constant. A value of 251 kJ/mol is taken for the activation energy of volume diffusion (Q_v) as quoted by Frost and Ashby [40], while 125.5 kJ/mol is used for the activation energy of grain boundary diffusion (Q_{gb}) since Q_{gb} is generally approximately equal to half of Q_v. These values seem to be similar to other steels and Ni based superalloys as quoted by Frost and Ashby [40].

Shear modulus (μ): It is well known that the elastic modulus-temperature dependence is similar in materials with identical crystal structure. Therefore, the shear modulus values of ferritic steel similar to 1.23Cr-1.2Mo-0.26V as provided in Table 4.18 [19] are used.

Table 4.18: Shear modulus as a function of temperature [19]

Temperature, T (^{o}C)	Shear Modulus, μ (GPa)
25	84
100	81
200	77
300	74
400	70
450	68
500	66
525	65
550	64
575	63
600	62
625	61
650	60
675	58
700	56

Stress exponent for power law creep: The stress exponent for power law creep generally varies in the range from 3.5 to 5. Therefore, the value of 4 for ferritic steels has been used as a reasonable assumption [57,128].

Inter-particle spacing (λ): The grain boundary precipitate spacing as a function of temperature and stress, measured from the micrographs presented in reference [17], is given in Table 4.19.

Table 4.19: Inter-particle spacing (λ) as a function of temperature and stress [17]

Temperature, T (^oC)	Stress, σ (kg/mm^2)	λ (μm)	Dominant deformation mechanism
525	25	$1.20x10^{-1}$	GBS
525	27	$1.20x10^{-1}$	GBS
525	30	$1.30x10^{-1}$	GBS
550	12	$1.60x10^{-1}$	GBS
550	20	$1.20x10^{-1}$	GBS
550	25	$1.40x10^{-1}$	GBS
550	27	$1.40x10^{-1}$	GBS
600	12	$1.50x10^{-1}$	GBS
600	20	$1.30x10^{-1}$	GBS
650	7	$2.20x10^{-1}$	GBS
650	12	$2.00x10^{-1}$	GBS
525	38	$1.40x10^{-1}$	PLC
550	30	$1.50x10^{-1}$	PLC
600	30	$1.50x10^{-1}$	PLC
650	20	$1.30x10^{-1}$	PLC

Constants A_{GBS} and A_{PLC}: The constants A_{GBS} and A_{PLC} of equations (27) and (28) are calculated using experimental data extracted from Figure 4.14, as summarized in Table 4.20 [17]. The calculation gives A_{GBS} = 9.29 X 10^9 and A_{PLC} = $4.29x10^4$ respectively. These values are in good agreement with A_{GBS} and A_{PLC} for the similar material as given in reference [40].

In summary, the parameters and physical constants used for constructing the deformation mechanism map are listed in Table 4.21.

Table 4.20: Experimental data for calculation of A_{GBS} and A_{PLC} [17]

Temperature, T(^oC)	Strain rate, $\dot{\gamma}$ (s^{-1})	Shear stress, τ_s (MPa)	Dominant deformation mechanism
525	$4.81x10^{-08}$	152.93	GBS
550	$1.44x10^{-07}$	113.28	GBS
600	$9.62x10^{-08}$	67.97	GBS
625	$4.81x10^{-07}$	67.97	GBS
650	$4.81x10^{-07}$	39.65	GBS
650	$2.41x10^{-06}$	67.97	GBS
525	$1.44x10^{-07}$	169.92	PLC
525	$1.20x10^{-05}$	215.23	PLC
550	$8.66x10^{-07}$	141.60	PLC
550	$1.68x10^{-05}$	169.92	PLC
600	$9.62x10^{-07}$	113.28	PLC
650	$2.89x10^{-05}$	113.28	PLC

Table 4.21: Various parameters and physical constants used in plotting the deformation mechanism map [40,57,128]

Quantity	Magnitude	Reference
Burgers Vector, b (m)	$2.5x10^{-10}$	40
Gas constant, R (Joule/mol)	8.3144	40
Boltzmann constant, K (MNm/K)	$1.38x10^{-29}$	40
Melting temperature, T_m (K)	1810	40
Obstacle-controlled glide		
0 K flow stress, τ_o/μ_o	$6.2x10^{-3}$	40
Pre-exponential constant, γ_o (s^{-1})	10^6	40
Activation energy for dislocation glide, $\Delta F/ \mu_o b^3$	2	40
Grain boundary sliding		
Constant, A_{GBS}	$9.29 X 10^9$	-
Activation energy for grain boundary sliding, Q_{gb} (KJ/mol)	125.4	40
Pre-exponential constant for grain boundary sliding, D_{ogb}	$1.1x10^{-12}$	40
Stress exponent, n	2	40
Power law Creep		
Stress exponent, n	4	57,128
Constant, A_{PLC}	$4.29x10^4$	-
Activation energy for volume diffusion, Q_v (KJ/mol)	251.4	40
Pre-exponential constant for volume diffusion D_{ov}	$2x10^{-4}$	40

4.6.3 A deformation mechanism map of 1.23Cr-1.2Mo-0.26V steel

A programming code is written and run in Matlab (R2007b) in a personal computer (Microsoft Windows 7 edition, 3GB RAM). Using equations (21), (27), and (28), the deformation mechanism map of 1.23Cr-1.2Mo-0.26V steel is constructed as shown in Figure 4.15. The temperature range selected for the map is between 100-800°C and no consideration is given to the PLB creep regime due to solute diffusion because the application range of the alloy is limited to 600°C, above which excessive oxidation occurs; additional reason is that ferrite/austenite transformation takes place above 700°C. The creep data for 1.23Cr-1.2Mo-0.26V steel are available between 500-675°C; they are interpolated and extrapolated to 100-800°C temperature range. In the map, the applied stress is presented as the equivalent shear stress normalized with respect to the shear modulus over the equivalent temperature normalized with respect to the melting point with both T and T_m expressed in Kelvin [40]. The corresponding strain rate (10^{-1}-10^{-10}) contours are also plotted as a variable on the map using the Newton Rapson method in Matlab (R2007b).

The three controlling mechanisms i.e. dislocation glide, PLC, and GBS, most prevalent for the given creep, are clearly shown in Figure 4.15. The solid lines (boundary lines) represent the field boundaries separating areas in the stress temperature space wherein the specified mechanisms remain dominant. The solid lines are obtained by equating the strain rate equations for each mechanism. Two bordering deformation mechanisms are considered to have comparable creep rates and equally contribute to the total deformation along the boundary lines.

The triple point (B) where dislocation glide, GBS, and PLC regions meet, the strain rates of all three mechanisms are equal. Therefore, by equating (21), (27), and (28), the normalized stress at the triple point can be obtained. As can be seen in the map, plastic deformation between $0.4T/T_m$ and $0.6T/T_m$ can be explained by two parallel processes: GBS and PLC. It is clear from the map that above the curved line B-D-E, PLC is the sole mechanism occurring at high temperature and high stress. Below the B-D-E line at low stresses, GBS dominates. Following the procedure of dividing the GBS region by Banerjee et al. [66], the GBS region is sub-divided into two sub-regions: GBS accommodated by wedge type cracking below $0.5T/T_m$, and GBS accommodated by cavitation above $0.5T/T_m$.

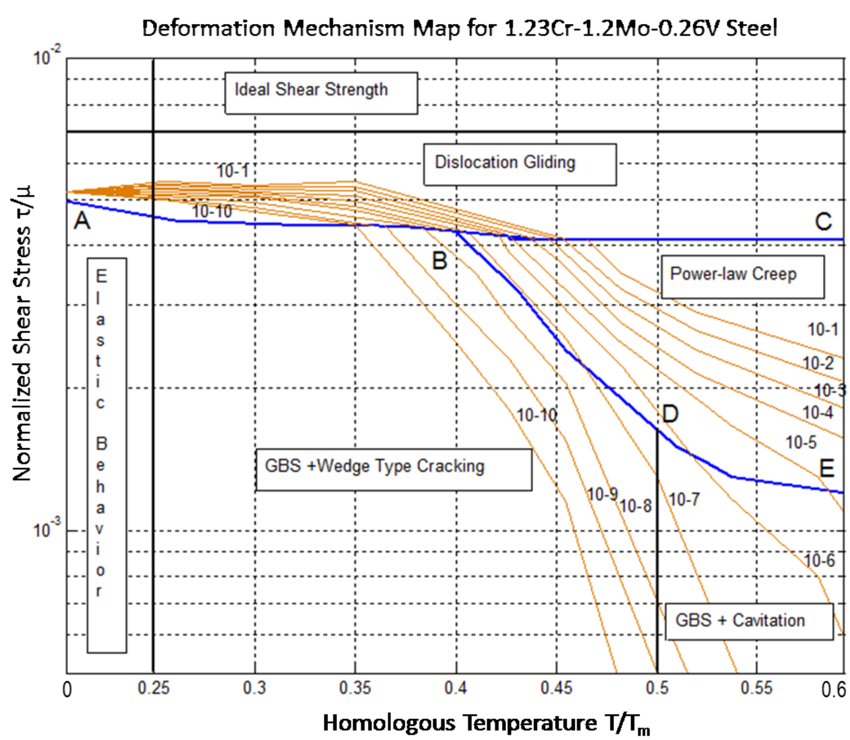

Figure 4.15: Deformation mechanism map for 1.23Cr-1.2Mo-0.26V steel.

4.6.4 Verification of the deformation mechanism map

The deformation mechanism map plotted above has been verified using experimental and neural network modeling results as described in the following sections.

4.6.4.1 Experimental results

The experimental data for PLB points (square points) given in Table 4.23 are also plotted on the map as shown by the B-D-G line in Figure 4.16. The deformation mechanism map shows that the experimental data points are in excellent agreement with boundary line drawn by equating the rate equations of GBS and PLC. This excellent match confirms the validity of using the rate equations for 1.23Cr-1.2Mo-0.26V steel.

4.6.4.2 Neural network results

A neural network modeling is also performed using experimental data. The PLB points used above for experimental validation are taken as the targets (normalized stresses) whereas homologous temperatures and strain rates are taken as the inputs. Inputs and targets and their ranges are given in Tables 4.22 and 4.23 [17]. In order to avoid over-fitting, a total of 16 data points is randomly divided into three subsets; a training subset (50% of the total data set), a validation subset (25% of the total data set), and a test subset (25% of the total data set). The Levenberg-Marquadt backpropagation method with three layered architecture (one input layer, one hidden layer, and one output layer) is used for the neural network modeling. After a number of trials, the most suitable architecture obtained is 2-11-1, i.e. 2 neurons in the input layer, 11 neurons in the hidden layer, and 1 neuron in the output layer. The performance is 4.60586×10^{-8} which is small and the training stops after only 8 epochs. Figure 4.17 shows the mean squared error vs. the number of epochs for training, validation, and testing subsets which indicate that no over-fitting occurred and the network is properly trained.

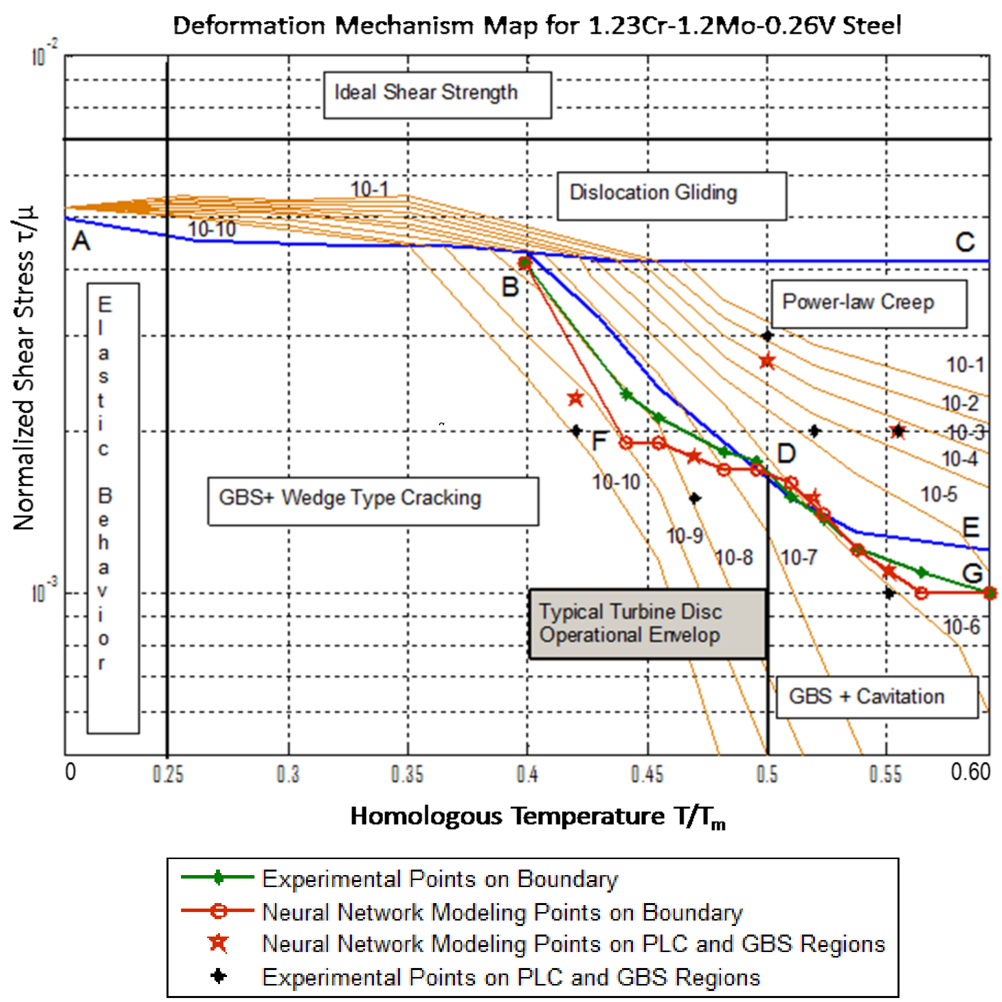

Figure 4.16: Experimental and neural network results for the validation of the deformation mechanism map for 1.23Cr-1.2Mo-0.26V steel.

Table 4.22: Inputs, targets, and their ranges [17] for modeling of the normalized stresses

Nr.	Input Parameters	Ranges
1	Homologous Temperature (T/T_m)	0.399-0.0593
2	Strain rate ($\dot{\gamma}$, s^{-1})	$1x10^{-8}$-$1x10^{-2}$
1	Target (τ/μ)	$9.06x10^{-4}$-$4.1x10^{-3}$

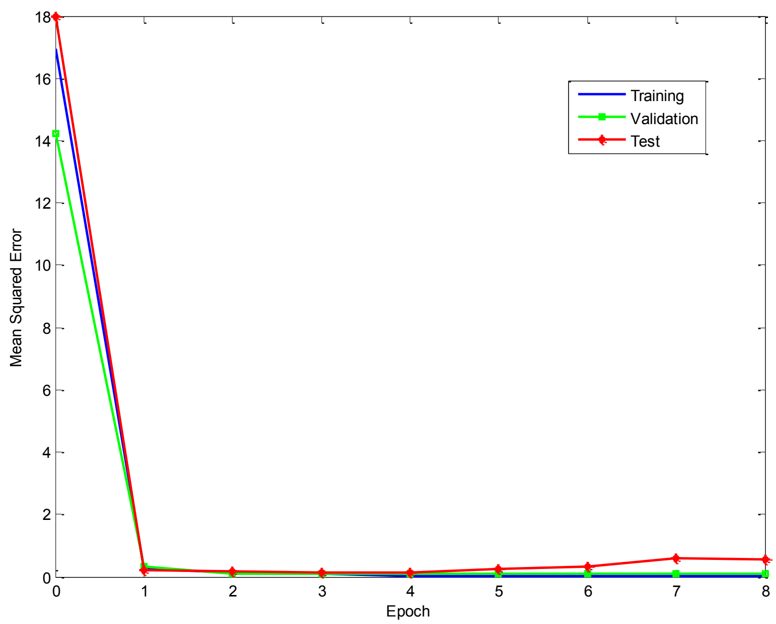

Figure 4.17: Mean squared error vs. epoch for modeling of the normalized stress.

The linear regression analysis is also performed as can be seen in Figure 4.18. The parameters obtained from the linear regression analysis are m = 0.73; b = 0.00041 and R = 0.95406. These parameters are close to ideal values (m = 1; b = 0; R = 1), which indicate a good fit and show the high accuracy of the model.

The output obtained from the modeling, corresponding target values and their % errors are summarized in Table 4.23. It can be seen that there is a good correlation between the output (Y) and the target (T) values and the overall percentage error is small.

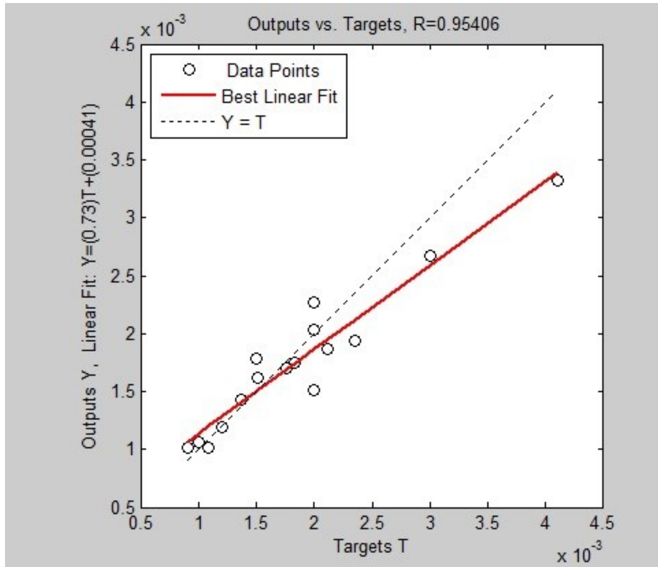

Figure 4.18: Linear regression analysis for modeling of the normalized stress.

Table 4.23: Outputs, targets, and corresponding % errors for modeling of the normalized stress

Nr.	Output, (Y)	Target (T)	(T-Y)	% Error, E	Dominant Deformation Mechanism
1	$4.1x10^{-3}$	$4.1x10^{-3}$	0.00	0.00	PLB
2	$1.9\ x10^{-3}$	$2.35x10^{-3}$	0.45	19.15	PLB
3	$1.9\ x10^{-3}$	$2.12x10^{-3}$	0.22	10.38	PLB
4	$1.7\ x10^{-3}$	$1.83x10^{-3}$	0.13	7.10	PLB
5	$1.7x10^{-3}$	$1.76x10^{-3}$	0.06	3.40	PLB
6	$1.6x10^{-3}$	$1.51x10^{-3}$	-0.09	5.96	PLB
7	$1.4\ x10^{-3}$	$1.37x10^{-3}$	-0.03	2.18	PLB
8	$1.2\ x10^{-3}$	$1.21x10^{-3}$	0.01	0.83	PLB
9	$1.0\ x10^{-3}$	$1.09x10^{-3}$	0.09	8.25	PLB
10	$1.0\ x10^{-3}$	$9.06x10^{-4}$	-0.094	10.37	PLB
11	$2.3\ x10^{-3}$	$2.00x10^{-3}$	-0.30	15.00	GBS
12	$1.8\ x10^{-3}$	$1.50x10^{-3}$	-0.30	20.00	GBS
13	$1.1x10^{-3}$	$1.00x10^{-3}$	-0.10	10.00	GBS
14	$1.5x10^{-3}$	$2.00x10^{-3}$	0.50	25.00	PLC
15	$2.0\ x10^{-3}$	$2.00x10^{-3}$	0.00	0.00	PLC
16	$2.7\ x10^{-3}$	$3.00x10^{-3}$	0.30	10.00	PLC

% Error, E = abs ((T-Y/T) x100)

The output values (circle points) obtained from the neural network modeling, given in Table 4.23, are also plotted on the map as shown by a B-F-D-G line in Figure 4.16. As can be seen from the Figure that neural network results accurately match experimental data points and the boundary line obtained by equating the rate equations for GBS and PLC. At point D, all three results overlap. Moreover, three random points in the GBS region and three random points in the PLC regions are also taken as inputs as shown in Table 4.23 in order to investigate whether the neural network can also be applied in these regions. As can be seen from Figure 4.16, the neural network outputs accurately match these random points and the error between them is very small. However, there is some scatter between neural network outputs and random points, and the best linear fit line and the one-to-one correspondence line deviate strongly from each other as can be seen from Figure 4.18. This may be caused by the small size of the inputs available for training, which seems not to allow appropriate learning of relationships between inputs and outputs.

In summary, the physics based rate equations and/or the neural network modeling can be used to construct or expand the investigated deformation mechanism map. The typical turbine disc operational envelop is also superimposed on the map and it is evident that GBS accommodated by wedge cracking is expected to dominate during service. This excellent modeling result opens new avenues and demonstrates the potential of the neural network to become a key design tool for Engineers if service conditions of actual components are accurately replicated.

Chapter 5

Thesis conclusions, contributions and future work

The primary focus of the thesis is to apply the feedforward neural network in modeling of materials such as Ni based superalloys and Cr-Mo-V steels used for turbine applications. The goals of the work are four fold: to compare the two neural network training methods for modeling of the γ’ precipitate size of Ni based superalloys; to model the thermal expansion coefficient of Ni based superalloys; to model the fatigue life and hysteresis energy and then to calculate the accumulated fatigue damage of Ni based superalloys; and finally to plot the creep deformation mechanism map of 1.23Cr-1.2Mo-0.26V steel used in land based turbines.

5.1 Conclusions

The following conclusions can be drawn from the present study:

1. γ’ precipitate size:

Two training methods, the Levenberg-Marquadt (Trainlm) and Bayesian Regularization (Trainbr), have been successfully used to develop neural network models to predict the γ’ precipitate size of various Nimonic alloys and IN100. Chemical compositions and heat treatments are used as inputs. The results of both methods are compared to each other, and both methods accurately predicted the γ’ precipitate size with only small errors. However, the Lavenberg-Marquadt method is proven to be faster and more accurate than the Bayesian Regularization method. Therefore, the Levenberg-Marquadt method is selected for all other neural network models. Moreover, in order to highlight the importance of ageing methods, a neural network model is also applied on the turbine blade material IN738LC to predict the γ' precipitate size. As the size of γ' precipitates can be directly related to fatigue and creep properties of turbine materials, these models could potentially help to predict the performance of turbine blade and disc materials.

2. Thermal expansion coefficient:

The modeling of thermal expansion coefficients of various γ' precipitate strengthened Ni based superalloys has been completed successfully. The model takes chemical compositions and heat treatments as inputs and predicts thermal expansion coefficients of various Ni based superalloys. Although the existing set of experimental data is limited, there is an excellent match between measurement data and modeling results. The developed models can potentially be used to assess the risk of thermo-mechanical stresses, damage, and failure at substrate-coating interfaces as well as between neighbouring turbine components.

3. Fatigue life:

The fatigue life of various Ni based superalloys used in turbine disc has been predicted using fracture mechanics and neural network approaches. Fracture mechanics is first used to predict the critical crack size to failure. The Paris equation is then integrated from the initial crack size to the final crack size in order to predict the crack propagation life for different load amplitudes. Crack initiation life values from literature are then added to obtain the total fatigue lives. Material's chemical compositions, microstructural properties, fatigue loading variables, and mechanical properties are used as inputs to predict the fatigue life using neural network as well. The model converges relatively well although it seems unable, as can be expected, to replicate the strong statistical uncertainties and variations commonly experienced in fatigue life.

4. Hysteresis energy:

The hysteresis energy is estimated using both the hysteresis area equation and the neural network approaches. The area equation calculates the energy absorbed per unit volume by the material during each fatigue cycle. Chemical compositions, microstructural properties, fatigue parameters, and mechanical properties are used as neural network inputs. Both, the area equation and the neural network approaches are accurate and yielded similar results.

5. Accumulated fatigue damage:

The accumulated fatigue damage to failure is estimated as the product of hysteresis energy and the number of cycles to failure. Hysteresis energies obtained from the area equation and the neural network are multiplied with the total fatigue life obtained from the fracture mechanics approach. Both, the hysteresis loop area equation and the neural network yielded similar results.

6. Deformation mechanism map:

Based on current understanding of time dependent deformation mechanisms operative in complex engineering alloys, the deformation mechanism map of 1.23Cr-1.2Mo-0.26V steel is constructed using dislocation glide, grain boundary sliding, and power law creep rate equations. The developed map is in good agreement with experimental results from literature and neural network modeling results. The constructed map could be potentially useful as a powerful tool for design engineers if service conditions of actual components are accurately replicated.

5.2 Contributions

Numerous research papers are available on the use of neural networks to predict various properties (strength, creep, and fatigue) and to form correlations within various parameters of Ni based superalloys. However, all modeling attempts so far have focused on only a few turbine component operating parameters. New approaches are yet to be developed that include all known application conditions in assessing component behavior as a function of temperature, chemical composition, and heat treatment. Therefore, this work makes a contribution in developing a comprehensive approach to describe and predict the behaviour, damage, and life of high temperature materials used in turbine components. Below are short overviews of specific contributions of this thesis:

1. γ' precipitate size:

Various neural network models have been previously developed to predict mechanical, fatigue, and creep properties of Ni based superalloys as function of microstructure. Lattice parameters of γ and γ' phases have also been developed as a function of chemical composition and temperature. However, neural network models to specifically predict γ' precipitate size of Ni based superalloys are still lacking. Therefore, neural network models are developed in this work to predict the γ' precipitate size as a function of chemical composition and heat treatment. The Levenberg-Marquadt (Trainlm) method is identified as a more appropriate method as compared to the Bayesian Regularization (Trainbr) method.

2. Thermal expansion coefficient:

Previous research has attempted to measure or derive the thermal expansion coefficient of simple metals and alloys. They are based on either features of the binding energy curve or regression analysis. Some authors have correlated the thermal expansion coefficient to the content and size of γ' precipitates of Ni based superalloys. However, current approaches are limited to low temperatures and provide only a rough estimate for higher temperatures. This thesis is the first of its kind to use the neural network modeling for predicting thermal expansion coefficients of Ni based superalloys using chemical compositions, heat treatments, and application temperatures as inputs.

3. Fatigue life:

Various neural network models to predict the fatigue crack growth rate, fatigue life, and fatigue properties of Ni based superalloys are available in the literature. However, very little has been done so far to combine both fracture mechanics and neural network approaches for a comprehensive prediction of the fatigue life of turbine blades and disc materials. Therefore, this work links linear elastic fracture mechanics and neural networks to predict high temperature fatigue life as a function of chemical compositions, microstructural properties, fatigue parameters, and mechanical properties.

4. Hysteresis energy and fatigue damage:

Several experimental studies and models have also been used to determine the hysteresis energies of materials. However, the neural network is yet to be investigated in this field. For this purpose, this thesis uses the area equation to determine the hysteresis energy which is then fed as targets into the neural network together with the chemical compositions, microstructural properties, fatigue parameters, and mechanical properties to estimate the accumulated damage.

5. Deformation mechanism map:

To date, several deformation mechanism maps have been constructed for different engineering alloys using rate equations for different creep mechanisms. Most maps are primarily constructed and/or validated using experimental data or microstructural evidences while others have assumed that observations made on simple metals and alloys are also applicable to complex engineering alloys. However, a general consensus is slowly emerging that GBS accommodated by different processes plays a major role in complex engineering alloys demanding a reassessment of conventional assumptions. In parallel, new approaches also need to be developed that can allow a cross-check of the validity of the emerging deformation mechanism maps. Therefore, the deformation mechanism map of 1.23Cr-1.2Mo-0.26V steel has been constructed where the modified rate equations incorporating the effects of back stresses of power law creep and GBS are considered. The map is then validated with experimental and artificial neural network results. The map is the first of its kind to be validated using the neural network modeling.

6. Journal and conference proceedings contributions as of the defence date:

1. N. Bano and M. Nganbe: Modeling of Thermal Expansion Coefficients of Ni based Superalloys using Artificial Neural Networks, Journal of Materials Engineering and Performance, Vol. 22, Issue 4, pp. 952-957, April 2013.
2. N. Bano and M. Nganbe: Neural Network Approach for Modeling the Hysteresis Energy of Ni based Superalloys, Proceedings of the International Conference on Mechanical Engineering and Mechatronics, Ottawa, Canada, August 2012.
3. N. Bano, A. Fahim, and M. Nganbe: Neural Network Model to Predict Low Cycle Fatigue Failure Energy of Rene77, Proceedings of the AES-ATEMA'2010 Fifth International Conference, Montreal, Quebec, Canada, pp. 123-126, June 2010.
4. N. Bano, A. Fahim, and M. Nganbe: Fatigue Crack Initiation Life Prediction of IN738LC using Artificial Neural Network, Proceedings of the AES-ATEMA'2010 Fifth International Conference, Montreal, Quebec, Canada, pp. 117-121, June 2010.
5. N. Bano, A. Fahim, and M. Nganbe: Modeling of γ’ Precipitate Size of IN738LC using Levenberg-Marquardt Backpropagation Neural Network, Proceedings of the First International Conference on Integrated Intelligent Computing, Bangalore, India, pp. 45-50, August 2010.

6. N. Bano, A. Fahim, and M. Nganbe: Prediction of Fracture Energy of IN738LC Superalloy using Neural Network, Proceedings of the International Conference on Fracture, Ottawa, July 2009.
7. N. Bano, A. Fahim, and M. Nganbe: Determination of Thermal Expansion Coefficient of IN738LC with Duplex Size Gamma Prime using Neural Network, Proceedings of the Conference of Metallurgists, Winnipeg, August 2008.
8. N. Bano, A. Fahim, and M. Nganbe: Neural Network Model of IN738LC Superalloy: Thermal Expansion Coefficient, Proceedings of the CSME Forum, Ottawa, June 2008.

7. Conference presentation contributions as of the defence date:

1. N. Bano and M. Nganbe: Neural Network Approach for Modeling the Hysteresis Energy of Ni based Superalloys, International Conference on Mechanical Engineering and Mechatronics, Ottawa, Canada, August 2012.
2. N. Bano, A. Fahim, and M. Nganbe: Neural Network Model to Predict Low Cycle Fatigue Failure Energy of Rene77, AES-ATEMA'2010 Fifth International Conference, Montreal, Quebec, Canada, June 2010.
3. N. Bano, A. Fahim, and M. Nganbe: Fatigue Crack Initiation Life Prediction of IN738LC using Artificial Neural Network, AES-ATEMA'2010 Fifth International Conference, Montreal, Quebec, Canada. June 2010.
4. N. Bano, A. Fahim, and M. Nganbe: Neural Network Model of IN738LC, Superalloy: Thermal Expansion Coefficient, CSME conference, Ottawa, June 2008.

5.3 Suggestions for future work

The results of this thesis have clearly proven the great potential of the neural network to become a powerful tool for predicting the behaviour and life of Ni based superalloys and steels used for turbine components. Below are suggestions for immediate further investigations that can contribute in achieving this goal:

1. Expand the investigation to other materials used at high temperatures.
2. Explore more training methods such as Gradient Descent, Gradient descent with Momentum, etc., to further optimise the performance of neural networks.
3. Explore neural network models with multiple outputs.
4. Explore serial connections of neural networks in which some networks automatically use the output of previous ones as their inputs.
5. Investigate the appropriateness of neural networks for predicting more complex states and demands such as ballistic and blast impact, thermo-mechanical loading, and stress-corrosion cracking.
6. Explore the appropriateness of neural networks in other complex areas typically covered by finite elements methods such as local stress concentrations.

References:

[1] R. C. Reed, The Superalloys, Fundamentals and Applications, Cambridge University Press, Cambridge, 2006.

[2] D. William and J. Callister, Materials Science and Engineering: An Introduction, John Wiley & Sons Inc., Hoboken New Jersey, 2008.

[3] P. K. Sung and D. R. Poirier, "Estimation of Densities and Coefficients of Thermal Expansion of Solid Ni Based Superalloys", Material Science and Engineering A, Vol. 245 (1), pp. 135-141, 1998.

[4] E. Balikci, R. A. Mirshams, and A. Raman, "Microstructure and Texture Effect on the Thermal Expansion of a Variously Aged Polycrystalline Superalloy IN738LC", Metallurgical and Materials Transactions A, Vol. 30, pp. 2803-2808, 1999.

[5] L. Zushu and K. C. Mills, "The Effect of γ' Content on the Densities of Ni Based Superalloys", Metallurgical and Materials Transactions B, Vol. 37 B, pp. 781-790, 2006.

[6] S. Raju, K. Sivasubramanian, R. Divakar, G. Panneerselvam, A. Banerjee, E. Mohandas, and M. P. Antony, "Thermal Expansion Studies on Inconel 600 by High Temperature X-ray Diffraction", Journal of Nuclear Materials, Vol. 325 (1), pp. 18-25, 2004.

[7] P. Abel and G. Bozzolo, "Calculation of Thermal Expansion Coefficients of Pure Elements and their Alloys", Scripta Materialia, Vol. 46, pp. 557-562, 2002.

[8] G. Bozzolo, M. F. del Grosso, and H. O. Mosca , "Algorithm for the Calculation of the Coefficient of Thermal Expansion of Multicomponent Metallic Alloys", Materials Letters, Vol. 62, pp. 3975-3977, 2008.

[9] G. Cadieux, "Influence of Heat Treatment on Heat Affected Zone Micro-processing in EB Welded Microcast-x INCONEL 718", Master Thesis, University of Manitoba, 1997.

[10] I. Roy, E. Balikci, S. Ibekwe, and A. Raman, "Precipitate Growth Activation Energy Requirements in the Duplex Size γ' Distribution in the Superalloy IN738LC", Journal of Materials Science, Vol. 40, pp. 6207-6215, 2005.

[11] J. R. Davis, ASM Speciality Handbook-Nickel, Cobalt, and their Alloys, ASM International, Materials Park, OH, 2000.

[12] S. A. Yandt, "Development of a Thermo-Mechanical Fatigue Testing Facility", Master Thesis, Carleton University, 1998.

[13] http://en.wikipedia.org/wiki/Superalloy, Accessed July 20, 2011.

[14] I. S. Kim, B. G. Choi, H. U. Hong, Y. S. Yoo, and C. Y. Jo, "Anomalous Deformation Behavior and Twin Formation of Ni based Superalloys at the Intermediate Temperatures", Materials Science and Engineering A, Vol. 528, pp. 7149-7155, 2011.

[15] E. Nembach, K. Suzuki, M. Ichihara, and S. Takeuchi, "In-situ Deformation of the Gamma Prime Hardened Superalloy Nimonic PE16 in High Voltage Electron Microscopes", Philosophical Magazine, Vol. 51A, pp. 607-618, 1985.

[16] M. E. Kassner, Fundamentals of Creep in Metals and Alloys, Second Edition, Elsevier Ltd., Oxford, UK, 2009.

[17] Y. Kadoya and T. Goto, "Creep Deformation and Creep-Rupture Behavior of Cr-Mo-V Steel Forgings", The Iron and Steel Institute of Japan International, Vol. 30, pp. 829-837, 1990.

[18] J. F. Shackelford, Introduction to Materials Science for Engineers, Seventh Edition, Pearson Prentice Hall, New Jersey, 2005.

[19] ASM International Handbook Committee, ASM Handbook-Properties and Selection: Irons, Steels and High Performance Alloys, ASM International, Vol. 1, 1990.

[20] N. D. Dimatteo, ASM Handbook-Fatigue and Fracture, ASM International, Vol. 19, 1996.

[21] X. Ma, H. Shi, J. Gu, Z. Wang, H. Harders, and T. Malow, "Temperature Effect on Low Cycle Fatigue Behavior of Ni Based Single Crystal Superalloy", Acta Mechanica Solida Sinica, Vol. 21 (4), pp. 289-297, August 2008.

[22] N. Bano, A. Fahim, and M. Nganbe, "Fatigue Crack Initiation Life Prediction of IN738 Using Artificial Neural Network", Proceedings of the Fifth International Conference on Advances and Trends in Engineering Materials and Their Applications, Montreal, Quebec, Canada, pp. 117-121, June 2010.

[23] G. E. Dieter, Mechanical Metallurgy, McGraw-Hill Company Limited, UK, 1988.

[24] S. D. Antolovich, E. Rosa, and A. Pineau, "Low Cycle Fatigue of Rene~77 at Elevated Temperatures", Materials Science and Engineering, Vol. 47, pp. 47-57, 1981.

[25] M. Ashby, H. Shercliff, and D. Cebon, Materials: Engineering, Science, Processing, and Design, University of Cambridge, 2007.

[26] K. O. Lee, K. H. Bae, and S. B. Lee, "Comparison of Prediction Methods for Low Cycle Fatigue Life of HIP Superalloys at Elevated Temperatures for Turbo-pump Reliability", Materials Science and Engineering A, Vol. 519, pp. 112-120, 2009.

[27] A. Saxena and S. D. Antolovich, “Low Cycle Fatigue, Fatigue Crack Propagation and Substructures in a Series of Polycrystalline Cu-AI Alloys”, Metallurgical Transactions A, Vol. 6A, pp.1809-1827, September 1975.

[28] M. D. Mathew, V. Singh, W. Chen, and R. P. Wahi, “Life Prediction for a Ni based Alloy Nimonic PE16 under Low Cycle Fatigue Loading at 923 K”, Acta Metallurgica et Materialia, Vol. 39 (7), pp. 1507-1513, 1991.

[29] D. S. Tchankov and K. V. Vesselinov, “Fatigue Life Prediction under Random Loading using Total Hysteresis Energy”, International Journal of Pressure Vessels and Piping, Vol. 75, pp. 955-960, 1998.

[30] M. Mazari, B. Bouchouicha, M. Zemri, M. Benguediab, and N. Ranganathan, “Fatigue Crack Propagation Analyses based on Plastic Energy Approach”, Computational Materials Science, Vol. 41, pp. 344-349, 2008.

[31] B. R. Daubenspeck and A. P. Gordon, “Extrapolation Techniques for Very Low Cycle Fatigue Behavior of a Ni based Superalloy”, Journal of Engineering Materials and Technology, Vol. 133, pp. 1-9, April 2011.

[32] L. Jiang, P. K. Liaw, C. R. Brooks, B. Somieski, and D. L. Klarstrom, “Nondestructive Evaluation of Fatigue Damage in ULTIMET® Superalloy”, Materials Science and Engineering A, Vol. 313, pp. 153-159, 2001.

[33] J. Y. Kim, L. J. Jacobs, J. Qu, and J. W. Littles, “Experimental Characterization of Fatigue Damage in a Ni based Superalloy using Non-linear Ultrasonic Waves”, Journal of the Acoustical Society of America, Vol. 120 (3), pp. 1266-1273, September 2006.

[34] R. K. Oruganti, R. Sivaramanivas, T. N. Karthik, V. Kommareddy, B. Ramadurai, B. Ganesan, E. J. Nieters, M. F. Gigliotti, M. E. Keller, and M. T. Shyamsunder,

"Quantification of Fatigue Damage Accumulation using Non-linear Ultrasound Measurements", International Journal of Fatigue, Vol. 29, pp. 2032-2039, 2007.

[35] A. Seweryn, A. Buczyn´ski, and J. Szusta, "Damage Accumulation Model for Low Cycle Fatigue", International Journal of Fatigue, Vol. 30, pp. 756-765, 2008.

[36] X. Wu, S. Williams, and D. Gong, "A True-Stress Creep Model Based on Deformation Mechanisms for Polycrystalline Materials", Journal of Materials Engineering and Performance, Vol. 21 (11), pp. 2255-2262, November 2012.

[37] R. J. Shipley and W. T. Becker, ASM Handbook-Failure Analysis and Prevention, ASM International, Vol. 11, 2002.

[38] J. Pelleg, Mechanical Properties of Materials, Solid Mechanics and Its Applications, Springer Science plus Business Media, pp. 259-336, 2013.

[39] O. D. Sherby and P. M. Burke, "Mechanical Behaviour of Crystalline Solids at Elevated Temperatures", Progress in Materials Science, Vol. 13, pp. 325-390, 1967.

[40] H. J. Frost and M. F. Ashby, Deformation Mechanism Maps-The Plasticity and Creep of Metals and Ceramics, Pergamon Press, 1982.

[41] T. G. Langdon, "Grain Boundary Sliding as a Deformation Mechanism during Creep", Philosophical Magazine, Vol. 22 (178), pp. 689-700, 1970.

[42] T. G. Langdon, "A Unified Approach to Grain Boundary Sliding in Creep and Superplasticity, Acta Metallurgica et Materialia, Vol. 42 (7), pp. 2437-2443, 1994.

[43] M. Kawasaki, S. Lee, and T. G. Langdon, "Constructing a Deformation Mechanism Map for a Superplastic Pb-Sn Alloy Processed by Equal-channel Angular Pressing", Scripta Materialia, Vol. 61, pp. 963-966, 2009.

[44] R. K. Bhargava, J. Moteff, and R. W. Swindeman, “The Dislocation Substructure, Carbides and the Deformation Mechanism Map for AlSI 304 Stainless Steel”, Metallurgical Transactions A, Vol. 7A, pp. 879-884, June 1976.

[45] M. F. Ashby, “A First Report on Deformation Mechanism Maps”, Acta Metallurgica, Vol. 20, pp. 887-897, July 1972.

[46] R. L. Bell and T. G. Langdon, “An Investigation of Grain Boundary Sliding during Creep”, Journal of Materials Science, Vol. 2, pp. 313-323, 1967.

[47] T. G. Langdon and F. A. Mohamed, “Deformation Mechanism Maps for Ceramics”, Journal of Materials Science, Vol. 11, pp. 317-327, 1976.

[48] T. G. Langdon, “Deformation Mechanism Maps for Applications at High Temperatures”, Geramurgia International, Vol. 6 (1), pp. 11-18, 1990.

[49] F. A. Mohamed and T. G. Langdon, “Deformation Mechanism Maps for Solid Solution Alloys”, Scripta Metallurgica, Vol. 9, pp. 137-140, 1975.

[50] F. A. Mohammed and T. G. Langdon, “Deformation Mechanism Maps for Superplastic Materials”, Scripta Metallurgica, Vol. 10, pp. 759-762, 1976.

[51] H. Luthy, R. A. White, and O. D. Sherby, “Grain Boundary Sliding and Deformation Mechanism Maps”, Materials Science and Engineering, Vol. 39, pp. 211-216, 1979.

[52] K. Janghorban and S. Esmaeili, “Deformation Mechanism Map for Ti-6wt%Al Alloy”, Journal of Materials Science, Vol. 26, pp. 3362-3365, 1991.

[53] J. A. Carey, P. M. Sargent, and D. R. H. Jones, “A Deformation Mechanism Map for IN738LC Superalloy”, Journal of Materials Science Letters, Vol. 9, pp. 572-575, 1990.

[54] S. A. Sajjadi and S. Nategh, “A High Temperature Deformation Mechanism Map for the High Performance Ni based Superalloy GTD-111”, Materials Science and Engineering A, Vol. 307, pp. 158-164, 2001.

[55] R. Castillo, A. K. Koul, J. P Immarigeon, P. Lowden, and J. Liburdi, Superalloys 1988, pp. 755-764, 1988.

[56] A. K. Koul and R. Castillo, “Creep behavior of Industrial Turbine Blade Materials” Proceedings of ASM 1993 Materials Congress Materials Week, Pittsburg, Pennsylvania, October 17-21, 1993.

[57] A. K. Koul, J. P. Immarigeon, and W. Wallace,” Microstructural Control in Ni based Superalloys”, Advances in High Temperature Structural Materials and Protective Coatings, National Research Council of Canada, pp. 95-125, 1994.

[58] M. F. Ashby, “On Interface-reaction Control of Nebarro-Herring Creep and Sintering”, Scripta Metallurgica, Vol. 3, pp. 837-842, 1969.

[59] X. J. Wu and A. K. Koul, “Grain Boundary Sliding in the Presence of Grain Boundary Precipitates during Transient Creep”, Metallurgical and Materials Transactions A, Vol. 26 A, pp. 905-914, April 1995.

[60] X. J. Wu and A. K. Koul, “Grain Boundary Sliding at Serrated Grain Boundaries”, Advanced Performance Materials, Vol. 4 (4), pp. 409-420, October 1997.

[61] A. Ayensu and T. G. Langdon, “The Inter-relationship between Grain Boundary Sliding and Cavitation during Creep of Polycrystalline Copper”, Metallurgical and Materials Transactions A, Vol. 27A, pp. 901-907, April 1996.

[62] S. Xu, X. J. Wu, A. K. Koul, and J. I. Dickson, “An Intergranular Creep Crack Growth Model Based on Grain Boundary Sliding”, Metallurgical and Materials Transactions A, Vol. 30A, pp. 1039-1045, April 1999.

[63] S. Xu, J. I. Dickson, and A. K. Koul, “Grain Growth and Carbide Precipitation in Superalloy, Udimet 520”, Metallurgical and Materials Transactions A, Vol. 29A, pp. 2687-2695, November 1998.

[64] J. Wadsworth, O. A. Ruano, and O. D. Sherby, “Denuded Zones, Diffusional Creep and Grain Boundary Sliding”, Metallurgical and Materials Transactions A, Vol. 33A, pp. 219-229, Febuary 2002.

[65] X. Wu, “Life Prediction of Gas Turbine Materials, Institute for Aerospace Research”, National Research Council, Canada, 2005.

[66] A. Banerjee, A. K. Koul, A. Kumar, and N. Goel, “Physics based Prognostics of Solder Joints in Avionics”, Annual Conference of the Prognostics and Health Management Society, 2011.

[67] M. Asadi, D. Guillot, A. Weck, S. R. Hegde, A. K. Koul, T. Sawatzky, and H. Saari, “Constructing a Validated Deformation Mechanisms Map using Low Temperature Creep Strain Accommodation Processes for Ni based Alloy 718”, Proceedings of the ASME 2012, Pressure Vessels and Piping Division Conference, PVP2012, 2012.

[68] P. A. S. Reed, M. J. Starink, S. R. Gunn, and I. Sinclair, “Adaptive Numerical Modeling and Hybrid Physically based ANM Approaches in Materials Engineering-A Survey”, Materials Science and Technology, Vol. 25 (4), pp. 488-503, 2009.

[69] H. Demuth, M. Beale, and M. Hagan, Neural Network Toolbox 5, User’s guide, The Math Works Inc., 2007.

[70] D. Raabe, "Challenges in Computational Materials Science", Advanced Materials, Vol. 14 (9), pp. 639-650, May 2002.

[71] M. T. Hagan and M. B. Menhaz, "Training Feedforward Network with the Marquadt Algorithm", IEEE Transactions on Neural Networks, Vol. 5 (6), pp. 989-993, November 1994.

[72] Y. Huang and P. L. Blackwell, "Prediction of Mechanical Properties of Superplastic Inconel 718 using Artificial Neural Networks", Materials Science and Technology, Vol. 18, pp. 1104-1108, October 2002.

[73] H. K. D. H. Bhadeshia, "Neural Networks in Materials Science", The Iron and Steel Institute of Japan International, Vol. 39, pp. 966-979, 1999.

[74] S. Yoshitake, V. Narayan, H. Harada, H. K. D. H. Bhadeshia, and D. J. C. MacKay, "Estimation of the γ and γ' Lattice Parameters in Ni based Superalloys using Neural Network Analysis", The Iron and Steel Institute of Japan International, Vol. 38, pp. 495-502, 1998.

[75] H. J. Sharpe, "Effect of Microstructure on High Temperature Mechanical Behaviour of Ni based Superalloys for Turbine Disc Applications", PhD. Thesis, Georgia Institute of Technology, 2007.

[76] R. S. Yassar, O. Abuomar, E. Hansen, and M. F. Horstemeyer, "On Dislocation-based Artificial Neural Network Modeling of Flow Stress", Materials and Design, Vol. 31, pp. 3683-3689, 2010.

[77] J. Jones and D. J. C. MacKay, "Neural Network Modeling of the Mechanical Properties of Ni based Superalloys", 8th International Symposium on Superalloys, Seven Springs, Pennsylvania, USA, pp. 417-424, 1996.

[78] F. Tanctret, H. K. D. H. Bhadeshia, and D. J. C. Mackay, “Comparison of Artificial Neural Networks with Gaussian Processes to Model the Yield Strength of Ni based Superalloys”, The Iron and Steel Institute of Japan International, Vol. 39 (10), pp. 1020-1026, 1999.

[79] J. Warde and D. M. Knowles, “Application of Neural Networks to Mechanical Property Determination of Ni based Superalloys”, The Iron and Steel Institute of Japan International, Vol. 39 (10), pp. 1006-1014, 1999.

[80] J. Warde and D. M. Knowles, “Use of Neural Networks for Alloy Design”, The Iron and Steel Institute of Japan International, Vol. 39 (10), pp. 1015-1019, 1999.

[81] M. E. Haque and K. V. Sudhakar, “ANN Backpropagation Prediction Model for Fracture Toughness in Microalloy Steel”, International Journal of Fatigue, Vol. 24, pp. 1003-1010, 2002.

[82] M. B. Esfahani, M. R. Toroghinejad, and S. Abbasi, “Artificial Neural Network Modeling the Tensile Strength of Hot Strip Mill Products”, The Iron and Steel Institute of Japan International, Vol. 49 (10), pp. 1583-1587, 2009.

[83] S. B. Singh, H. K. D. H. Bhadeshia, D. J. C. MacKay, H. Carey, and I. Martin, “Neural Network Analysis of Steel Plate Processing”, Ironmaking and Steelmaking, Vol. 25 (5), pp. 355-365, 1998.

[84] P. F. Bariani, S. Bruschi, and T. D. Negro, “Prediction of Ni based Superalloys’ Rheological Behaviour under Hot Forging Conditions using Artificial Neural Networks”, Journal of Materials Processing Technology, Vol. 152, pp. 395-400, 2004.

[85] I. D. Martino, J. W. Brooks, P. A. S. Reed, P. Holdway, and A. Wisbey, “Adaptive Numerical Modeling of High Temperature Strength, Creep, and Fatigue Behaviour in Ni

based Superalloys”, Materials Science and Technology, Vol. 23 (12), pp. 1402-1407, 2007.

[86] M. A. Yescas, “Prediction of the Vickers Hardness Austempered Ductile Irons using Neural Network”, International Journal of Cast Metals Research, Vol. 15, pp. 513-521, 2003.

[87] A. M. Hassan, A. Alrashdan, M. T. Hayajneh, and A. T. Mayyas, “Prediction of Density, Porosity, and Hardness in Aluminum-Copper-based Composite Materials using Artificial Neural Network”, Journal of Materials Processing Technology, Vol. 209, pp. 894-899, 2009.

[88] J. Syarif, Y. P. Detak, and R. Ramli, “Modeling of Correlation between Heat Treatment and Mechanical Properties of Ti-6Al-4V Alloy Using Feedforward Backpropagation Neural Network”, The Iron and Steel Institute of Japan International, Vol. 50 (11), pp. 1689-1694, 2010.

[89] Y. S. Yoo , C. Y. Jo, and C. N. Jones , “Compositional Prediction of Creep Rupture Life of Single Crystal Ni based Superalloy by Bayesian Neural Network”, Materials Science and Engineering A, Vol. 336, pp. 22-29, 2002.

[90] Y. S. Yoo, I. S. Kim, D. H. Kim, C. Y. Jo, H. M. Kim, and C. N. Jones, “The Application of Neural Network to the Development of Single Crystal Superalloys” Superalloys 2004, pp. 942-950, 2004.

[91] H. Fujii, D. J. C. MacKay, and H. K. D. H. Bhadeshia “Bayesian Neural Network Analysis of Fatigue Crack Growth Rate in Ni based Superalloys”, The Iron and Steel Institute of Japan International, Vol. 36, pp. 1373-1382, 1996.

[92] J. M. Schooling and P. A. S. Reed, “The Application of Neural Computing Methods to the Modeling of Fatigue in Ni based Superalloys”, 8th International Symposium on Superalloys, Seven Springs, Pennsylvania, USA, pp. 409-416, 1996.

[93] J. M. Schooling, M. Brown, and P. A. S. Reed, “An Example of the Use of Neural Computing Techniques in Materials Science-The Modeling of Fatigue Thresholds in Ni based Superalloys”, Materials Science and Engineering A, Vol. 260, pp. 222-239, 1999.

[94] J. A. Lee, D. P. Almond, and B. Harris, “The Use of Neural Networks for the Prediction of Fatigue Lives of Composite Materials”, Composites: Part A, Vol. 30, pp. 1159-1169, 1999.

[95] V. Venkatesh and H. J. Rack, “A Neural Network Approach to Elevated Temperature Creep-fatigue Life Prediction”, International Journal of Fatigue, Vol. 21, pp. 225-234, 1999.

[96] M. E. Haque and K. V. Sudhakar, “ANN based Prediction Model for Fatigue Crack Growth in DP Steel”, Fatigue and Fracture of Engineering Materials and Structures, Vol. 23, pp. 63-68, 2001.

[97] T. T. Pleune and O. K. Chopra, “Using Artificial Neural Networks to Predict the Fatigue Life of Carbon and Low-alloy Steels”, Nuclear Engineering and Design, Vol. 197, pp. 1-12, 2000.

[98] V. S. Srinivasan, M. Valsan, K. B. S. Rao, S. L. Mannan, and B. Raj, “Low Cycle Fatigue and Creep-fatigue Interaction Behavior of 316L (N) Stainless Steel and Life Prediction by Artificial Neural Network Approach”, International Journal of Fatigue, Vol. 25, pp. 1327-1338, 2003.

[99] K. Genel, "Application of Artificial Neural Network for Predicting Strain-life Fatigue Properties of Steels on the Basis of Tensile Tests", International Journal of Fatigue, Vol. 26, pp. 1027-1035, 2004.

[100] K. B. Kim, D. J. Yoon, J. C. Jeong, and S. S. Lee, "Determining the Stress Intensity Factor of a Material with an Artificial Neural Network from Acoustic Emission Measurements", Independent Nondestructive Testing and Evaluation International, Vol. 37, pp. 423-429, 2004.

[101] C. Marquardt and H. Zenner, "Lifetime Calculation under Variable Amplitude Loading with the Application of Artificial Neural Networks", International Journal of Fatigue, Vol. 27, pp. 920-927, 2005.

[102] J. Y. Kang, B. I. Choia, H. J. Lee, J. S. Kimb, and K. J. Kim, "Neural Network Application in Fatigue Damage Analysis under Multiaxial Random Loadings", International Journal of Fatigue, Vol. 28, pp. 132-140, 2006.

[103] T. Bucar, M. Nagode, and M. Fajdiga, "A Neural Network Approach to Describing the Scatter of S-N Curves", International Journal of Fatigue, Vol. 28, pp. 311-323, 2006.

[104] A. Bezazi, S. G. Pierce, K. Worden, and E. H. Harkati, "Fatigue Life Prediction of Sandwich Composite Materials under Flexural Tests using a Bayesian Trained Artificial Neural Network", International Journal of Fatigue, Vol. 29, pp. 738-747, 2007.

[105] A. Fotovati and T. Goswami, "Prediction of Elevated Temperature Fatigue Crack Growth Rates in Ti-6Al-4V Alloy-Neural Network Approach" Materials and Design, Vol. 25, pp. 547-554, 2004.

[106] M. Fast, M. Assadi, and S. De, "Development and Multi-utility of an ANN Model for an Industrial Gas Turbine", Applied Energy, Vol. 86, pp. 9-17, 2009.

[107] R. A. Cottis, L. Qing, G. Owen, S. J. Gartland, I. A. Helliwell, and M. Turega, "Neural Network Methods for Corrosion Data Reduction", Materials and Design, Vol. 20, pp.169-178, 1999.

[108] Z. Raida, "Modeling EM Structures in the Neural Network Toolbox of Matlab", IEEE Antenna's and Propagation Magzine, Vol. 44 (6), December 2002.

[109] E. Balikci, R. A. Mirshams, and A. Raman, "Fracture Behaviour of Superalloy IN738LC with Various Precipitate Microstructures", Materials Science and Engineering A, Vol. 265, pp. 50-62, 1999.

[110] B. Reppich and G. Schumann, "Electron Microscopy of γ' Particles in Ni based Superalloys", Materials Science and Engineering A, Vol. 101, pp. 171-182, 1988.

[111] F. Cverna, ASM Ready Reference-Thermal properties of Metals, ASM Materials Data Series, 2002.

[112] B. A. Chawles, D. L. Sims, and J. R. Warren, "Evaluation of the Cyclic Behaviour of Aircraft Turbine Disc Alloys", NASA Lewis Research Centre, NAS3-20367.

[113] V. Kliman and M. Bily, "Hysteresis Energy of Cyclic Loading", Materials Science and Engineering, Vol. 68, pp. 11-18, 1984.

[114] W. BruÈckner, "Deformation Mechanism Map for Cu-Ni Thin Films", Physica Status Solidi (a), Vol. 176, pp. 919-924, 1999.

[115] H. Arabi, J. Szpunar, S. H. Mirdamadi, and S. H. Razavi, "Improvement of Age-hardening Process of a Ni Based Superalloy, IN738LC, by Induction Ageing", Journal of Materials Science, Vol. 37, pp. 1461-1471, 2002.

[116] R. J. Smith, G. J. Lewis, and D. H. Yates, "Development and Application of Ni Alloys in Aerospace Engineering", Aircraft Engineering and Aerospace Technology, Vol. 73 (2), pp. 138-146, 2001.

[117] E. Balikci, A. Raman, and R. A. Mirshams, "Influence of Various Heat Treatments on the Microstructure of Polycrystalline IN738LC", Metallurgical and Materials Transactions A, Vol. 28, pp. 1993-2003, October 1997.

[118] N. Bano, A. Fahim, and M. Nganbe, "Modeling of γ' Precipitate Size of IN738LC using Levenberg-Marquardt Backpropagation Neural Network", Proceedings of the First International Conference on Integrated Intelligent Computing, Banglore, India, pp. 45-50, August 2010.

[119] H. W. Grunling, K. Schneider, and L. Singheiser, "Mechanical Properties of Coated Systems", Materials Science and Engineering, Vol. 88, pp. 177-189, 1987.

[120] V. Teixeira, M. Andritschky, W. Fischer, H. P. Buchkremer, and D. Stover, "Effects of Deposition Temperature and Thermal Cycling on Residual Stress State in Zirconia-based Thermal Barrier Coatings", Surface and Coatings Technology, Vol. 120-121, pp. 103-111, 1999.

[121] K. Fritscher, C. Leyens, and M. Peters, "Development of a Low-expansion Bond Coating for Ni based Superalloys", Materials Science and Engineering A, Vol. 190, pp. 253-258, 1995.

[122] J. A. Haynes, B. A. Pint, W. D. Porter, and I. G. Wright, "Comparison of Thermal Expansion and Oxidation Behavior of Various High Temperature Coating Materials and Superalloys", Materials at High Temperature, Vol. 21 (2), pp. 87-94 (8), May 2004.

[123] G. Parthasarathy, S. Menon, K. Richardson, A. Jameel, D. McNamee, T. Desper, M. Gorelik, and C. Hickenbottom, "Neural Network Models for Usage Based Remaining Life Computation", Journal of Engineering for Gas Turbines and Power, Vol. 130, pp. 1-7, January 2008.

[124] U. Hermosilla, I. A. Jones, T. H. Hyde, R. C. Thomson, and M. S. A. Karunaratne, "Finite Element Modeling of the Development of Stresses in Thermal Barrier Coatings", International Conference on Sustainable Power Generation and Supply, Supergen 09, pp. 1-7, 2009.

[125] E. P. Busso, L. Wright, H. E. Evans, L. N. McCartney, S. R. J. Saunders, S. Osgerby, and J. Nunn, "A Physics-based Life Prediction Methodology for Thermal Barrier Coating Systems", Acta Materialia, Vol. 55, pp. 1491-1503, 2007.

[126] E. P. Busso, H. E. Evans, L. Wright, L. N. McCartney, J. Nunn, and S. Osgerby, "Software Tool for Lifetime Prediction of Thermal Barrier Coating Systems", Materials and Corrosion, Vol. 59 (7), pp. 556-565, 2008.

[127] E. Balikci, R. A. Mirshams, and A. Raman, "Tensile Strengthening in the Ni Based Superalloy IN738LC", Journal of Materials Engineering and Performance, Vol. 9, pp. 324-329, 2000.

[128] K. Maruyama, K. Sawada, J. Koike, H. Sato, and K. Yagi, "Examination of Deformation Mechanism Maps in 2.25Cr-1Mo Steel by Creep Tests at Strain Rates of 10^{-11} to 10^{-6} s^{-1}", Materials Science and Engineering A, Vol. 224, pp. 166-172, 1997.

Appendix A

Table A1: Detailed information about inputs and targets for modeling of the γ' precipitate size [110]

	Element content (wt %)									T_{sol}	t_{sol}	T_{age}	t_{age}	γ' size
Material	Ni	Cr	Al	Ti	Co	Mo	Si	Fe	C	(°C)	(hr)	(°C)	(hr)	(nm)
Nimonic PE 16, W	43	16.7	1.1	1.28	0.19	3.27	0.24	34.155	0.065	1150	4	670	1	2.5
Nimonic PE 16, W	43	16.7	1.1	1.28	0.19	3.27	0.24	34.155	0.065	1150	4	670	5.65	4.3
Nimonic PE 16, W	43	16.7	1.1	1.28	0.19	3.27	0.24	34.155	0.065	1150	4	670	20.5	6.6
Nimonic PE 16, W	43	16.7	1.1	1.28	0.19	3.27	0.24	34.155	0.065	1150	4	670	34	7.5
Nimonic PE 16, W	43	16.7	1.1	1.28	0.19	3.27	0.24	34.155	0.065	1150	4	670	59	9
Nimonic PE 16, W	43	16.7	1.1	1.28	0.19	3.27	0.24	34.155	0.065	1150	4	670	90	10.5
Nimonic PE 16, W	43	16.7	1.1	1.28	0.19	3.27	0.24	34.155	0.065	1150	4	670	100	10.9
Nimonic PE 16, W	43	16.7	1.1	1.28	0.19	3.27	0.24	34.155	0.065	1150	4	670	290	15.8
Nimonic PE 16, W	43	16.7	1.1	1.28	0.19	3.27	0.24	34.155	0.065	1150	4	670	300	15.7
Nimonic PE 16, W	43	16.7	1.1	1.28	0.19	3.27	0.24	34.155	0.065	1150	4	670	1000	23.5
Nimonic PE 16, W	43	16.7	1.1	1.28	0.19	3.27	0.24	34.155	0.065	1150	4	750	0.5	6
Nimonic PE 16, W	43	16.7	1.1	1.28	0.19	3.27	0.24	34.155	0.065	1150	4	750	2.7	9.5
Nimonic PE 16, W	43	16.7	1.1	1.28	0.19	3.27	0.24	34.155	0.065	1150	4	750	3	9.5
Nimonic PE 16, W	43	16.7	1.1	1.28	0.19	3.27	0.24	34.155	0.065	1150	4	750	6.5	12.25
Nimonic PE 16, W	43	16.7	1.1	1.28	0.19	3.27	0.24	34.155	0.065	1150	4	750	7	12.6
Nimonic PE 16, W	43	16.7	1.1	1.28	0.19	3.27	0.24	34.155	0.065	1150	4	750	12	15
Nimonic PE 16, W	43	16.7	1.1	1.28	0.19	3.27	0.24	34.155	0.065	1150	4	750	14	16
Nimonic PE 16, W	43	16.7	1.1	1.28	0.19	3.27	0.24	34.155	0.065	1150	4	750	27	20.3
Nimonic PE 16, W	43	16.7	1.1	1.28	0.19	3.27	0.24	34.155	0.065	1150	4	750	50	24.5
Nimonic PE 16, W	43	16.7	1.1	1.28	0.19	3.27	0.24	34.155	0.065	1150	4	750	67	27
Nimonic PE 16, W	43	16.7	1.1	1.28	0.19	3.27	0.24	34.155	0.065	1150	4	750	85	30.3
Nimonic PE 16, W	43	16.7	1.1	1.28	0.19	3.27	0.24	34.155	0.065	1150	4	750	98.5	32.2
Nimonic PE 16, W	43	16.7	1.1	1.28	0.19	3.27	0.24	34.155	0.065	1150	4	750	3360	119
Nimonic PE 16, W	43	16.7	1.1	1.28	0.19	3.27	0.24	34.155	0.065	1150	4	800	2	18.1
Nimonic PE 16, W	43	16.7	1.1	1.28	0.19	3.27	0.24	34.155	0.065	1150	4	800	18	35.5
Nimonic PE 16, W	43	16.7	1.1	1.28	0.19	3.27	0.24	34.155	0.065	1150	4	800	62	54.1
Nimonic PE 16, W	43	16.7	1.1	1.28	0.19	3.27	0.24	34.155	0.065	1150	4	800	212	78.4
Nimonic PE 16, W	43	16.7	1.1	1.28	0.19	3.27	0.24	34.155	0.065	1150	4	800	512	111.6
Nimonic PE 16, W	43	16.7	1.1	1.28	0.19	3.27	0.24	34.155	0.065	1150	4	820	24	22
Nimonic PE 16, W	43	16.7	1.1	1.28	0.19	3.27	0.24	34.155	0.065	1150	4	820	27	48
Nimonic PE 16, W	43	16.7	1.1	1.28	0.19	3.27	0.24	34.155	0.065	1150	4	820	200	93.4
Nimonic PE 16, W	43	16.7	1.1	1.28	0.19	3.27	0.24	34.155	0.065	1150	4	820	288	105
Nimonic PE 16, W	43	16.7	1.1	1.28	0.19	3.27	0.24	34.155	0.065	1150	4	820	480	122
Nimonic PE 16, W	43	16.7	1.1	1.28	0.19	3.27	0.24	34.155	0.065	1150	4	820	652	138
Nimonic PE 16, W	43	16.7	1.1	1.28	0.19	3.27	0.24	34.155	0.065	1150	4	820	841	150
Nimonic PE 16, W	43	16.7	1.1	1.28	0.19	3.27	0.24	34.155	0.065	1150	4	820	1696	198

Nimonic PE 16, W	43	16.7	1.1	1.28	0.19	3.27	0.24	34.155	0.065	1150	4	820	2449	215
Nimonic PE 16, W	43	16.7	1.1	1.28	0.19	3.27	0.24	34.155	0.065	1150	4	824	0.225	10
Nimonic PE 16, W	43	16.7	1.1	1.28	0.19	3.27	0.24	34.155	0.065	1150	4	824	0.39	11.1
Nimonic PE 16, W	43	16.7	1.1	1.28	0.19	3.27	0.24	34.155	0.065	1150	4	824	0.9	16.7
Nimonic PE 16, W	43	16.7	1.1	1.28	0.19	3.27	0.24	34.155	0.065	1150	4	824	1.7	20.2
Nimonic PE 16, W	43	16.7	1.1	1.28	0.19	3.27	0.24	34.155	0.065	1150	4	824	2	23
Nimonic PE 16, W	43	16.7	1.1	1.28	0.19	3.27	0.24	34.155	0.065	1150	4	824	9	31
Nimonic PE 16, W	43	16.7	1.1	1.28	0.19	3.27	0.24	34.155	0.065	1150	4	824	14.5	40.9
Nimonic PE 16, W	43	16.7	1.1	1.28	0.19	3.27	0.24	34.155	0.065	1150	4	824	25.4	47
Nimonic PE 16, W	43	16.7	1.1	1.28	0.19	3.27	0.24	34.155	0.065	1150	4	824	28	48.7
Nimonic PE 16, W	43	16.7	1.1	1.28	0.19	3.27	0.24	34.155	0.065	1150	4	824	53	69
Nimonic PE 16, W	43	16.7	1.1	1.28	0.19	3.27	0.24	34.155	0.065	1150	4	824	76	72.2
Nimonic PE 16, W	43	16.7	1.1	1.28	0.19	3.27	0.24	34.155	0.065	1150	4	824	113	79
Nimonic PE 16, W	43	16.7	1.1	1.28	0.19	3.27	0.24	34.155	0.065	1150	4	824	160	98.7
Nimonic PE 16, W	43	16.7	1.1	1.28	0.19	3.27	0.24	34.155	0.065	1150	4	824	161	72
Nimonic PE 16, W	43	16.7	1.1	1.28	0.19	3.27	0.24	34.155	0.065	1150	4	824	215	106
Nimonic PE 16, W	43	16.7	1.1	1.28	0.19	3.27	0.24	34.155	0.065	1150	4	824	215	99.7
Nimonic PE 16, W	43	16.7	1.1	1.28	0.19	3.27	0.24	34.155	0.065	1150	4	824	290	108
Nimonic PE 16, W	43	16.7	1.1	1.28	0.19	3.27	0.24	34.155	0.065	1150	4	824	370	123.7
Nimonic PE 16, W	43	16.7	1.1	1.28	0.19	3.27	0.24	34.155	0.065	1150	4	824	410	110
Nimonic PE 16, W	43	16.7	1.1	1.28	0.19	3.27	0.24	34.155	0.065	1150	4	824	480	134
Nimonic PE 16, W	43	16.7	1.1	1.28	0.19	3.27	0.24	34.155	0.065	1150	4	824	590	142.6
Nimonic PE 16, W	43	16.7	1.1	1.28	0.19	3.27	0.24	34.155	0.065	1150	4	824	712	152.6
Nimonic PE 16, W	43	16.7	1.1	1.28	0.19	3.27	0.24	34.155	0.065	1150	4	824	1010	173
Nimonic PE 16, W	43	16.7	1.1	1.28	0.19	3.27	0.24	34.155	0.065	1150	4	824	1050	173
Nimonic PE 16, W	43	16.7	1.1	1.28	0.19	3.27	0.24	34.155	0.065	1150	4	824	1700	192.7
Nimonic PE 16, W	43	16.7	1.1	1.28	0.19	3.27	0.24	34.155	0.065	1150	4	824	1825	214.1
Nimonic PE 16, W	43	16.7	1.1	1.28	0.19	3.27	0.24	34.155	0.065	1150	4	840	2.65	26
Nimonic PE 16, W	43	16.7	1.1	1.28	0.19	3.27	0.24	34.155	0.065	1150	4	840	5.6	20
Nimonic PE 16, W	43	16.7	1.1	1.28	0.19	3.27	0.24	34.155	0.065	1150	4	840	6	35
Nimonic PE 16, W	43	16.7	1.1	1.28	0.19	3.27	0.24	34.155	0.065	1150	4	840	27.2	58
Nimonic PE 16, W	43	16.7	1.1	1.28	0.19	3.27	0.24	34.155	0.065	1150	4	840	69.6	69
Nimonic PE 16, W	43	16.7	1.1	1.28	0.19	3.27	0.24	34.155	0.065	1150	4	840	75	90
Nimonic PE 16, W	43	16.7	1.1	1.28	0.19	3.27	0.24	34.155	0.065	1150	4	840	140	110
Nimonic PE 16, W	43	16.7	1.1	1.28	0.19	3.27	0.24	34.155	0.065	1150	4	840	260	129
Nimonic PE 16, W	43	16.7	1.1	1.28	0.19	3.27	0.24	34.155	0.065	1150	4	840	260	107
Nimonic PE 16, W	43	16.7	1.1	1.28	0.19	3.27	0.24	34.155	0.065	1150	4	840	288	139
Nimonic PE 16, W	43	16.7	1.1	1.28	0.19	3.27	0.24	34.155	0.065	1150	4	840	480	155
Nimonic PE 16, W	43	16.7	1.1	1.28	0.19	3.27	0.24	34.155	0.065	1150	4	840	631	153
Nimonic PE 16, W	43	16.7	1.1	1.28	0.19	3.27	0.24	34.155	0.065	1150	4	840	652	168
Nimonic PE 16, W	43	16.7	1.1	1.28	0.19	3.27	0.24	34.155	0.065	1150	4	840	841	196
Nimonic PE 16, W	43	16.7	1.1	1.28	0.19	3.27	0.24	34.155	0.065	1150	4	840	943	202
Nimonic PE 16, W	43	16.7	1.1	1.28	0.19	3.27	0.24	34.155	0.065	1150	4	840	960	174
Nimonic PE 16, W	43	16.7	1.1	1.28	0.19	3.27	0.24	34.155	0.065	1150	4	840	960	203
Nimonic PE 16, W	43	16.7	1.1	1.28	0.19	3.27	0.24	34.155	0.065	1150	4	840	1607	231.5
Nimonic PE 16, W	43	16.7	1.1	1.28	0.19	3.27	0.24	34.155	0.065	1150	4	840	2448	294
Nimonic PE 16, W	43	16.7	1.1	1.28	0.19	3.27	0.24	34.155	0.065	1150	4	840	3360	325
Nimonic PE 16, G	43.2	16.2	1.25	1.28	0.05	3.5	0.06	35.61	0.054	1150	4	810	1	15.5

Nimonic PE 16, G	43.2	16.2	1.25	1.28	0.05	3.5	0.06	35.61	0.054	1150	4	810	5.795	28
Nimonic PE 16, G	43.2	16.2	1.25	1.28	0.05	3.5	0.06	35.61	0.054	1150	4	810	12	30.6
Nimonic PE 16, G	43.2	16.2	1.25	1.28	0.05	3.5	0.06	35.61	0.054	1150	4	810	20.12	41
Nimonic PE 16, G	43.2	16.2	1.25	1.28	0.05	3.5	0.06	35.61	0.054	1150	4	810	50.09	59
Nimonic PE 16, G	43.2	16.2	1.25	1.28	0.05	3.5	0.06	35.61	0.054	1150	4	810	58.72	56.5
Nimonic PE 16, G	43.2	16.2	1.25	1.28	0.05	3.5	0.06	35.61	0.054	1150	4	810	75.42	63
Nimonic PE 16, G	43.2	16.2	1.25	1.28	0.05	3.5	0.06	35.61	0.054	1150	4	810	102.7	81
Nimonic PE 16, G	43.2	16.2	1.25	1.28	0.05	3.5	0.06	35.61	0.054	1150	4	810	166	93.5
Nimonic PE 16, G	43.2	16.2	1.25	1.28	0.05	3.5	0.06	35.61	0.054	1150	4	810	265.6	95.4
Nimonic PE 16, G	43.2	16.2	1.25	1.28	0.05	3.5	0.06	35.61	0.054	1150	4	810	405.9	118
Nimonic PE 16, G	43.2	16.2	1.25	1.28	0.05	3.5	0.06	35.61	0.054	1150	4	810	569	140
Nimonic PE 16, G	43.2	16.2	1.25	1.28	0.05	3.5	0.06	35.61	0.054	1150	4	810	652	119
Nimonic PE 16, G	43.2	16.2	1.25	1.28	0.05	3.5	0.06	35.61	0.054	1150	4	810	2086	204
Nimonic PE 16, G	43.2	16.2	1.25	1.28	0.05	3.5	0.06	35.61	0.054	1150	4	810	2925	223
Nimonic 80A	76	19.4	1.53	2.47	0.1	0	0.2	0.19	0.07	1000	4	700	197	17
Nimonic 80A	76	19.4	1.53	2.47	0.1	0	0.2	0.19	0.07	1000	4	700	509	23
Nimonic 80A	76	19.4	1.53	2.47	0.1	0	0.2	0.19	0.07	1000	4	850	0.33	11
Nimonic 80A	76	19.4	1.53	2.47	0.1	0	0.2	0.19	0.07	1000	4	850	1	19
Nimonic 80A	76	19.4	1.53	2.47	0.1	0	0.2	0.19	0.07	1000	4	850	10	49
Nimonic 80A	76	19.4	1.53	2.47	0.1	0	0.2	0.19	0.07	1000	4	850	40	86
Nimonic 80A	76	19.4	1.53	2.47	0.1	0	0.2	0.19	0.07	1000	4	850	240	148
Nimonic 90	59.3	19.5	1.8	2	16	0.3	1	0	0.13	1150	4	850	1	17
Nimonic 90	59.3	19.5	1.8	2	16	0.3	1	0	0.13	1150	4	850	1.12	18
Nimonic 90	59.3	19.5	1.8	2	16	0.3	1	0	0.13	1150	4	850	4.12	32
Nimonic 90	59.3	19.5	1.8	2	16	0.3	1	0	0.13	1150	4	850	8.17	38.5
Nimonic 90	59.3	19.5	1.8	2	16	0.3	1	0	0.13	1150	4	850	9	42
Nimonic 90	59.3	19.5	1.8	2	16	0.3	1	0	0.13	1150	4	850	12.5	66
Nimonic 90	59.3	19.5	1.8	2	16	0.3	1	0	0.13	1150	4	850	14.33	48
Nimonic 90	59.3	19.5	1.8	2	16	0.3	1	0	0.13	1150	4	850	25.17	51
Nimonic 90	59.3	19.5	1.8	2	16	0.3	1	0	0.13	1150	4	850	32.5	61
Nimonic 90	59.3	19.5	1.8	2	16	0.3	1	0	0.13	1150	4	850	40	96
Nimonic 90	59.3	19.5	1.8	2	16	0.3	1	0	0.13	1150	4	850	46.17	69
Nimonic 90	59.3	19.5	1.8	2	16	0.3	1	0	0.13	1150	4	850	91.17	107
Nimonic 90	59.3	19.5	1.8	2	16	0.3	1	0	0.13	1150	4	850	180	161
Nimonic 90	59.3	19.5	1.8	2	16	0.3	1	0	0.13	1150	4	850	197.2	128
Nimonic 90	59.3	19.5	1.8	2	16	0.3	1	0	0.13	1150	4	850	435.3	168
Nimonic 90	59.3	19.5	1.8	2	16	0.3	1	0	0.13	1150	4	850	1009	205
Nimonic 90	59.3	19.5	1.8	2	16	0.3	1	0	0.13	1150	4	850	1078	219
Nimonic 90	59.3	19.5	1.8	2	16	0.3	1	0	0.13	1150	4	850	1331	209
Nimonic 90	59.3	19.5	1.8	2	16	0.3	1	0	0.13	1150	4	850	1847	222.5
Nimonic 90	59.3	19.5	1.8	2	16	0.3	1	0	0.13	1150	4	950	0.017	15
Nimonic 90	59.3	19.5	1.8	2	16	0.3	1	0	0.13	1150	4	950	0.02	8.8
Nimonic 90	59.3	19.5	1.8	2	16	0.3	1	0	0.13	1150	4	950	0.042	18
Nimonic 90	59.3	19.5	1.8	2	16	0.3	1	0	0.13	1150	4	950	0.5	36
Nimonic 90	59.3	19.5	1.8	2	16	0.3	1	0	0.13	1150	4	950	1	46
Nimonic 90	59.3	19.5	1.8	2	16	0.3	1	0	0.13	1150	4	950	1.5	57

Nimonic 90	59.3	19.5	1.8	2	16	0.3	1	0	0.13	1150	4	950	3	73
Nimonic 90	59.3	19.5	1.8	2	16	0.3	1	0	0.13	1150	4	950	5	91
Nimonic 90	59.3	19.5	1.8	2	16	0.3	1	0	0.13	1150	4	950	31.45	213
Nimonic 90	59.3	19.5	1.8	2	16	0.3	1	0	0.13	1150	4	950	70	275
Nimonic 90	59.3	19.5	1.8	2	16	0.3	1	0	0.13	1150	4	950	170	363
Nimonic 90	59.3	19.5	1.8	2	16	0.3	1	0	0.13	1150	4	950	300	418
Nimonic 90	59.3	19.5	1.8	2	16	0.3	1	0	0.13	1150	4	950	1000	600
Nimonic 105	53.9	15	5	1	20	5	0	0	0.12	1200	20	850	0.083	13.6
Nimonic 105	53.9	15	5	1	20	5	0	0	0.12	1200	20	850	0.25	15.7
Nimonic 105	53.9	15	5	1	20	5	0	0	0.12	1200	20	850	0.67	29.1
Nimonic 105	53.9	15	5	1	20	5	0	0	0.12	1200	20	850	2	34.6
Nimonic 105	53.9	15	5	1	20	5	0	0	0.12	1200	20	850	4.5	47.8
Nimonic 105	53.9	15	5	1	20	5	0	0	0.12	1200	20	850	8	65.4
Nimonic 105	53.9	15	5	1	20	5	0	0	0.12	1200	20	850	27	85.3
Nimonic 105	53.9	15	5	1	20	5	0	0	0.12	1200	20	850	64	122
Nimonic 105	53.9	15	5	1	20	5	0	0	0.12	1200	20	850	125	149
Nimonic 105	53.9	15	5	1	20	5	0	0	0.12	1200	20	850	329	184
Nimonic 105	53.9	15	5	1	20	5	0	0	0.12	1200	20	850	506	242
Nimonic 105	53.9	15	5	1	20	5	0	0	0.12	1200	20	850	1000	325
Nimonic 105	53.9	15	5	1	20	5	0	0	0.12	1200	20	1000	0.05	55
Nimonic 105	53.9	15	5	1	20	5	0	0	0.12	1200	20	1000	0.167	66
Nimonic 105	53.9	15	5	1	20	5	0	0	0.12	1200	20	1000	0.67	98
Nimonic 105	53.9	15	5	1	20	5	0	0	0.12	1200	20	1000	3	162
Nimonic 105	53.9	15	5	1	20	5	0	0	0.12	1200	20	1000	8	227
Nimonic 105	53.9	15	5	1	20	5	0	0	0.12	1200	20	1000	27	324
Nimonic 105	53.9	15	5	1	20	5	0	0	0.12	1200	20	1000	64	424
Nimonic 105	53.9	15	5	1	20	5	0	0	0.12	1200	20	1000	125	410
Nimonic 105	53.9	15	5	1	20	5	0	0	0.12	1200	20	1000	216	450
Nimonic 105	53.9	15	5	1	20	5	0	0	0.12	1200	20	1000	512	720
IN100	50	10	4.75	5.1	15.5	0	0	0	0	1200	2	800	0.33	15
IN100	50	10	4.75	5.1	15.5	0	0	0	0	1200	2	800	0.58	19
IN100	50	10	4.75	5.1	15.5	0	0	0	0	1200	2	800	1	20
IN100	50	10	4.75	5.1	15.5	0	0	0	0	1200	2	800	5	27
IN100	50	10	4.75	5.1	15.5	0	0	0	0	1200	2	800	10	36
IN100	50	10	4.75	5.1	15.5	0	0	0	0	1200	2	800	30	46
IN100	50	10	4.75	5.1	15.5	0	0	0	0	1200	2	800	50	50
IN100	50	10	4.75	5.1	15.5	0	0	0	0	1200	2	800	100	71
IN100	50	10	4.75	5.1	15.5	0	0	0	0	1200	2	800	200	95
IN100	50	10	4.75	5.1	15.5	0	0	0	0	1200	2	800	400	124
IN100	50	10	4.75	5.1	15.5	0	0	0	0	1200	2	800	600	139
IN100	50	10	4.75	5.1	15.5	0	0	0	0	1200	2	800	800	159
IN100	50	10	4.75	5.1	15.5	0	0	0	0	1200	2	900	0.16	21
IN100	50	10	4.75	5.1	15.5	0	0	0	0	1200	2	900	0.33	28
IN100	50	10	4.75	5.1	15.5	0	0	0	0	1200	2	900	0.42	38
IN100	50	10	4.75	5.1	15.5	0	0	0	0	1200	2	900	0.58	45
IN100	50	10	4.75	5.1	15.5	0	0	0	0	1200	2	900	1	63
IN100	50	10	4.75	5.1	15.5	0	0	0	0	1200	2	900	3	74

IN100	50	10	4.75	5.1	15.5	0	0	0	0	1200	2	900	5	81
IN100	50	10	4.75	5.1	15.5	0	0	0	0	1200	2	900	10	126
IN100	50	10	4.75	5.1	15.5	0	0	0	0	1200	2	900	30	143
IN100	50	10	4.75	5.1	15.5	0	0	0	0	1200	2	900	50	185
IN100	50	10	4.75	5.1	15.5	0	0	0	0	1200	2	900	100	232
IN100	50	10	4.75	5.1	15.5	0	0	0	0	1200	2	900	200	292
IN100	50	10	4.75	5.1	15.5	0	0	0	0	1200	2	900	400	364
IN100	50	10	4.75	5.1	15.5	0	0	0	0	1200	2	900	600	392
IN100	50	10	4.75	5.1	15.5	0	0	0	0	1200	2	900	800	439
IN100	50	10	4.75	5.1	15.5	0	0	0	0	1200	2	900	1000	538
IN100	50	10	4.75	5.1	15.5	0	0	0	0	1200	2	1000	0.16	54
IN100	50	10	4.75	5.1	15.5	0	0	0	0	1200	2	1000	0.33	70
IN100	50	10	4.75	5.1	15.5	0	0	0	0	1200	2	1000	0.42	86
IN100	50	10	4.75	5.1	15.5	0	0	0	0	1200	2	1000	0.58	100
IN100	50	10	4.75	5.1	15.5	0	0	0	0	1200	2	1000	1	109
IN100	50	10	4.75	5.1	15.5	0	0	0	0	1200	2	1000	5	180
IN100	50	10	4.75	5.1	15.5	0	0	0	0	1200	2	1000	10	249
IN100	50	10	4.75	5.1	15.5	0	0	0	0	1200	2	1000	30	401
IN100	50	10	4.75	5.1	15.5	0	0	0	0	1200	2	1000	50	479
IN100	50	10	4.75	5.1	15.5	0	0	0	0	1200	2	1000	100	541
IN100	50	10	4.75	5.1	15.5	0	0	0	0	1200	2	1000	200	582
IN100	50	10	4.75	5.1	15.5	0	0	0	0	1200	2	1000	400	652
IN100	50	10	4.75	5.1	15.5	0	0	0	0	1200	2	1000	600	727
IN100	50	10	4.75	5.1	15.5	0	0	0	0	1200	2	1000	800	770
IN100	50	10	4.75	5.1	15.5	0	0	0	0	1200	2	1000	1000	873

T_{sol}, T_{age}, t_{sol} and t_{age} refer to solutionizing temperature, ageing temperature, solutionizing time and ageing time respectively.

Table A2: Detailed information about inputs and targets for modeling of the thermal expansion coefficient [4,11,111]

Nr.	Material	T_{app}(°C)	T_{sol} (°C)	t_{sol} (hr)	M_{sol}	T_{age}(°C)	t_{age}(hr)	M_{age}	CTE, (α, 10^{-6}/°C)
1	IN738LC	550	1200	4	CWQ	-	-	-	12.77
2	IN738LC	650	1200	4	CWQ	-	-	-	13.22
3	IN738LC	750	1200	4	CWQ	-	-	-	13.61
4	IN738LC	850	1200	4	CWQ	-	-	-	14.16
5	IN738LC	550	1200	4	CWQ	1050	24	FC	12.76
6	IN738LC	650	1200	4	CWQ	1050	24	FC	13.26
7	IN738LC	750	1200	4	CWQ	1050	24	FC	13.74
8	IN738LC	850	1200	4	CWQ	1050	24	FC	14.22
9	IN738LC	550	1200	4	CWQ	1120	24	FC	12.96
10	IN738LC	650	1200	4	CWQ	1120	24	FC	13.4
11	IN738LC	750	1200	4	CWQ	1120	24	FC	13.86
12	IN738LC	850	1200	4	CWQ	1120	24	FC	14.35
13	IN738LC	550	1200	4	CWQ	1140	24	WQ	12.57
14	IN738LC	650	1200	4	CWQ	1140	24	WQ	12.84

15	IN738LC	750	1200	4	CWQ	1140	24	WQ	13.11
16	IN738LC	850	1200	4	CWQ	1140	24	WQ	13.69
17	Nimonic 90	20	1080	8	AC	705	16	AC	16.9
18	Nimonic 90	227	1080	8	AC	705	16	AC	18.3
19	Nimonic 90	427	1080	8	AC	705	16	AC	19.3
20	Nimonic 90	927	1080	8	AC	705	16	AC	20.8
21	X-750	20	1150	2	AC	845	24	AC	11.6
22	X-750	227	1150	2	AC	845	24	AC	14.4
23	X-750	427	1150	2	AC	845	24	AC	16.7
24	X-750	871	1150	2	AC	845	24	AC	16.8
25	X-750	927	1150	2	AC	845	24	AC	20.7
26	Astroloy	25	1175	4	AC	845	24	AC	13.5
27	Astroloy	540	1175	4	AC	845	24	AC	13.9
28	Astroloy	871	1175	4	AC	845	24	AC	16.2
29	IN100	93	1080	4	AC	870	12	AC	13
30	IN100	540	1080	4	AC	870	12	AC	13.9
31	IN100	1090	1080	4	AC	870	12	AC	18.1
32	IN738	25	1120	2	AC	845	24	AC	11.3
33	IN738	93	1120	2	AC	845	24	AC	11.6
34	IN738	540	1120	2	AC	845	24	AC	14
35	Mar M 246	93	1220	2	AC	870	24	AC	11.3
36	Mar M 246	540	1220	2	AC	870	24	AC	14.8
37	Mar M 246	1090	1220	2	AC	870	24	AC	18.6
38	Udimet 500	540	1080	4	AC	845	24	AC	14
39	Udimet 500	871	1080	4	AC	845	24	AC	16
40	Waspaloy	540	1080	4	AC	845	24	AC	13.9
41	Waspaloy	816	1080	4	AC	845	24	AC	15.7
42	Waspaloy	871	1080	4	AC	845	24	AC	16
43	IN713LC	205	1177	2	AC	-	-	-	12.6
44	duplex	427	1177	2	AC	-	-	-	15.1
45	duplex	649	1177	2	AC	-	-	-	16.2
46	duplex	871	1177	2	AC	-	-	-	16.76
47	Nimonic 115	205	1191	1.5	AC	1100	6	AC	12.76
48	Nimonic 115	427	1191	1.5	AC	1100	6	AC	13.41
49	Nimonic 115	649	1191	1.5	AC	1100	6	AC	14.4
50	Nimonic 115	871	1191	1.5	AC	1100	6	AC	15.7

T_{app}, T_{sol}, T_{age}, t_{sol}, t_{age} M_{sol}, and M_{age} and CTE refer to application temperature, solutionizing temperature, ageing temperature, solutionizing time, ageing time, solutionizing quenching method, ageing quenching method and coefficient of thermal expansion respectively.